

Sami Auvinen

COMPUTATIONAL MODELING OF THE PROPERTIES OF TiO₂ NANOPARTICLES

Thesis for the degree of Doctor of Science (Technology) to be presented with due permission for public examination and criticism in the Auditorium of the Student Union House at Lappeenranta University of Technology, Lappeenranta, Finland on the 19th of December, 2013, at noon.

Acta Universitatis
Lappeenrantaensis 564

Supervisor Professor Matti Alatalo
LUT School of Technology
Department of Mathematics and Physics
Lappeenranta University of Technology
Finland

Reviewers Professor Kari Laasonen
School of Chemical Technology
Aalto University
Finland

Professor Juha Vaara
Department of Physics
University of Oulu
Finland

Opponent Professor Tapio Rantala
Department of Physics
Tampere University of Technology
Finland

ISBN 978-952-265-544-8

ISBN 978-952-265-545-5 (PDF)

ISSN-L 1456-4491

ISSN 1456-4491

Lappeenrannan teknillinen yliopisto
Yliopistopaino 2013

Abstract

Sami Auvinen

Computational modeling of the properties of TiO₂ nanoparticles

Lappeenranta 2013

59 p.

Acta Universitatis Lappeenrantaensis 564

Diss. Lappeenranta University of Technology

ISBN 978-952-265-544-8, ISBN 978-952-265-545-5 (PDF), ISSN-L 1456-4491, ISSN 1456-4491

In this study we discuss the electronic, structural, and optical properties of titanium dioxide nanoparticles, and also the properties of Ni(II) diimine dithiolato complexes as dyes in dye-sensitized TiO₂ based solar cells. The abovementioned properties have been modeled by using computational codes based on the density functional theory. The results achieved show slight evidence on the structure-dependent band gap broadening, and clear blue-shifts in absorption spectra and refractive index functions of ultra-small TiO₂ particles. It is also shown that these properties are strongly dependent on the shape of the nanoparticles. Regarding the Ni(II) diimine dithiolato complexes as dyes in dye-sensitized TiO₂ based solar cells, it is shown that based on the experimental electrochemical investigation and DFT studies all studied diimine derivatives could serve as potential candidates for the light harvesting, but the efficiencies of the dyes studied are not very promising.

Keywords: *nanoparticle physics, cluster structures, absorption, optical properties*

UDC 539.2:535.34: 669.295:004.942:51.001.57

Preface

This work has been done at Lappeenranta University of Technology, Faculty of Technology, Department of Mathematics and Physics, Laboratory of Applied Mathematics, under supervision and guidance of Professor Matti Alatalo during years 2008-2013.

The work has been supported by Finnish Academy of Science and Letters, Vilho, Yrjö and Kalle Väisälä Fund, Sachtleben Pigments Oy, and The Research Foundation of Lappeenranta University of Technology. The computational resources were provided by CSC – IT Centre for Sciences Ltd.

There are so many people, who have been helping me in different ways during this long process, so the list is quite long and partly overlapping. First of all I want to thank my supervisor Matti Alatalo for giving me the opportunity to work and study in the research group of computational materials science, and for his advices, supervision, and support during all these years. I also want to thank all my collaborators involved in UV-TSM project: Heikki Haario, Erik Vartiainen, Juhopertti Jalava, Ralf-Johan Lamminmäki, Veli-Matti Taavitsainen, Minna Kuusisto, and Olga Miroshnichenko. As my international collaborator, thanks also goes for Abhinav Kumar.

It has been a privilege to work in a research group with many brilliant young scientists. Thank you my fellow co-workers Olga, Matti, Katariina, Heikki, Arto, Mikko, Marikki and Anindita. You all have participated in the studies related to this thesis, in one way or another, and we have also had refreshing and interesting conversations during the coffee and lunch breaks.

I want to acknowledge the reviewers Professor Juha Vaara and Professor Kari Laasonen. I am grateful for their efforts and comments. I am also grateful for Professor Tapio Rantala for his efforts as the opponent.

You should never forget that working and studying is not the only thing that matters in your life. Happy life with family and friends is also an essential part in your

life. I want to thank all my relatives and friends for their care and understanding. Especially I wish to thank my friends Tommi, Mari, Matti, Marikki, Liisi, and Mia. You really helped me through the hell and rain of fire that occurred in my private life during the writing process of this thesis. Without your help I would have not succeeded. I also wish to thank my parents and my brothers: Aulis, Anja, Ari, and Tomi. You have always supported and encouraged me.

Finally I wish to thank the most important persons in my life. They are my kids Niilo, Vili, and Lilli. You three are the best thing in my life, and without you my life would be empty. I love you so much!

Lappeenranta, 25.11.2013

Sami Auvinen

List of Publications

This thesis consists of an overview and the following publications

- I** S. Auvinen, M. Alatalo, H. Haario, J.P. Jalava, R.J. Lamminmäki, Size and Shape Dependence of the Electronic and Spectral Properties in TiO₂ Nanoparticles, *The Journal of Physical Chemistry C* 115, 8484-8493 (2011).

- II** S. Auvinen, M. Alatalo, H. Haario, E. Vartiainen, J.-P. Jalava, R.-J. Lamminmäki, Refractive Index Functions of TiO₂ Nanoparticles, *The Journal of Physical Chemistry C* 117, 3503-3512 (2013).

- III** A. Kumar, S. Auvinen, M. Trivedi, R. Chauhan, M. Alatalo, Synthesis, Characterization and Light Harvesting Properties of Nickel(II) Diimine Dithiolate Complexes, *Spectrochimica Acta Part A: Molecular and Biomolecular Spectroscopy* 115, 106-110 (2013).

- IV** S. Auvinen, M. Lahti, M. Alatalo, Unoccupied Titanium 3d States in Stoichiometric TiO₂ Nanoparticles, *J. Phys.: Condens. Matter*, Submitted (2013).

Author's contribution. In publications I and II the author has performed all the calculations and written most of the text. In publication III the author has performed all the calculations and written parts of the text. In publication IV the author has actively participated in the study, done all the GPAW test calculations, and participated in planning and interpretation of the VASP calculations. The author has also written most of the text in publication IV.

Abbreviations

| | |
|---------|---|
| CB | Conduction band |
| DFT | Density functional theory |
| DOS | Density of states |
| DSSC | Dye-sensitized solar cell |
| FTO | Fluorine-doped tin oxide |
| GGA | Generalized gradient approximation |
| HOMO | Highest occupied molecular orbital |
| IPCE | Incident photon-to-current efficiency |
| KK | Kramers-Kronig (relation) |
| LDA | Local density approximation |
| LUMO | Lowest unoccupied molecular orbital |
| PSD | Particle size distribution |
| RIF | Refractive index function |
| TDDFT | Time-dependent density functional theory |
| TPTDDFT | Time-propagation time-dependent density functional theory |
| TSM | Turbidity spectrum measurement |
| VB | Valence band |

| | |
|------------------------------|---|
| c_m | Expansion coefficients for partial waves m |
| $E[n]$ | Energy functional |
| $E_{Hartree}[n]$ | The classical Coulomb interaction energy functional |
| E_{HK} | Hohenberg-Kohn energy functional |
| E_{II} | Interaction energy of the nuclei |
| $E_{int}[n]$ | Internal potential energy |
| $E_{TF}[n]$ | Thomas-Fermi energy functional |
| $E_{xc}[n]$ | The exchange-correlation energy functional |
| ff | Fill factor |
| $\hat{H}(t)$ | The time-dependent Hamiltonian |
| $\hat{H}_{eff}(t)$ | The effective time-dependent Hamiltonian |
| J_{sc} | Short circuit current |
| $n_0(\mathbf{r})$ | Ground state electron density |
| $n(\mathbf{r})$ | Electron density |
| \tilde{p} | Set of projection operators |
| $T[n]$ | Internal kinetic energy |
| $V_{eff}^\sigma(\mathbf{r})$ | Local potential |
| $V_{ext}(\mathbf{r})$ | External potential |
| V_{oc} | Open circuit voltage |
| η | Power conversion efficiency |
| σ | Spin |
| \mathcal{T} | Linear transformation operator in PAW formalism |
| $\psi_i(t)$ | The time-dependent independent-particle wave function |
| $\tilde{\psi}_v$ | Smooth wavefunction |
| ψ_v | All-electron wavefunction |

Contents

| | | |
|----------|--|-----------|
| 1 | Introduction | 13 |
| 2 | Background | 15 |
| 2.1 | General properties of TiO ₂ | 15 |
| 2.2 | Quantum-size effect | 18 |
| 2.3 | Dye-sensitization of TiO ₂ | 19 |
| 3 | Theory | 23 |
| 3.1 | Density functional theory | 23 |
| 3.2 | Time-dependent density functional theory | 26 |
| 3.3 | Projector augmented wave method | 28 |
| 3.4 | Computational details | 30 |
| 3.4.1 | GPAW | 30 |
| 3.4.2 | VASP | 30 |
| 3.4.3 | Gaussian 09 | 30 |
| 4 | Review of the modeling results | 31 |
| 4.1 | Structural and electronic properties | 31 |
| 4.1.1 | Stoichiometric nanoparticles with terminal Ti-O bonds | 31 |
| 4.1.2 | Defect states in stoichiometric structures without terminal Ti-O bonds | 38 |
| 4.2 | Absorption characteristics and optical properties | 41 |
| 4.3 | Dye-sensitization of TiO ₂ nanoparticles | 45 |
| 5 | Concluding remarks | 51 |

Chapter 1

Introduction

During the past few decades there has been a true breakthrough of nanotechnology. This field of science is the key element in many aspects of our everyday life, although we might not see it. Nanotechnology is imported to our homes in surface coatings, UV protection, renewable energy from solar cells, cosmetics, paints, food dyes, medicines, ceramics and plastics, and even in deodorants. Today more and more emphasis is also put on environmental aspects and green chemistry, which is also raising the importance of this field of science. This is especially true in the case of titanium dioxide. Many of us might never have heard about this compound, but we are actually surrounded by its presence. Almost all of us have even eaten this compound during the last 24 hours!

TiO₂ is a wide band gap semiconductor which has a very high optical reflectivity at visible wavelengths, while being a strong absorber of ultraviolet radiation. It is also photoactive, and exhibits high surface reactivity with many chemical agents. On the other hand, TiO₂ is also chemically inert and non-toxic. Due to these properties titanium dioxide is the most used white pigment and opacifier in paints, food dyes, medicines, ceramics and plastics. It also has promising applications for solar cells, batteries, UV protectors, and self-cleaning surface coatings. All these properties make titanium dioxide a very fascinating compound.

All the modern applications of TiO₂ demand better understanding of the optical and electronic properties of this semiconductor, especially the behavior of these properties in nano-sized form. When the particle size is reduced, many interesting phenomena take place. We are entering the realm of quantum physics, where all the classical theories related to bulk quantities do not apply anymore. When we think of light scattering phenomena, we also have to deal with the duality of light.

In earlier studies the optical and electronic properties of titanium dioxide nanoparticles have shown to be strongly dependent on the structure and size of the particle. Small clusters also exhibit quantum size effects, where particles experience an effective band gap broadening, and this also has an effect on the properties of the ultra-fine particles. One interesting phenomena is that as ultra-fine particles this highly refractive white opacifier turns transparent for the visible light, while still being efficient absorber of UV wavelengths.

The aim of my studies was to understand the optical and electronic behavior of small TiO_2 particles at the atomic level. The first task was to computationally model the absorption characteristics and refractive index functions (RIFs) of ultra-small TiO_2 particles, and see how the quantum-size effect and particle size affect these properties. Because the structure, and thus the band structure of the particle are also dependent on particle size, the second task was to study the effects of structure on the light absorption characteristics. After gathering the basic knowledge on the behaviour of the small particles, I also participated in a study of practical application of TiO_2 in dye-sensitized solar cells (DSSCs). The aim was to study dyes having absorbances in the longer wavelength range, and be able to explain the nature of charge transfer in these molecules.

Chapter 2

Background

In this chapter I go through the chemical and physical background of titanium dioxide, and review the earlier theoretical and experimental results for TiO_2 bulk structures as well as for nanoparticles. I start by looking at the general properties of bulk titanium dioxide and then proceed to properties of nanoparticles and theory of DSSCs.

2.1 General properties of TiO_2

Titanium dioxide is a semiconducting metal oxide, which has three different crystal structures. Anatase and rutile structures are based on distorted TiO_6 octahedra, and due to slightly different bonding lengths and angles between titanium and oxygen atoms, they have different space groups and cell parameters. Anatase has $I4_1/amd$ space group with cell parameters of $a=3.784$ and $c=9.515$, whereas rutile has $P4_2/mnm$ space group with cell parameters of $a=4.5936$ and $c=2.9587$ [1, 2]. Both structures are tetragonal. Brookite, on the other hand, has a more complicated orthorhombic structure with $Pbca$ space group and cell parameters of $a=9.184$, $b=5.447$, and $c=5.145$ [1, 3]. The crystal structures for bulk anatase and rutile TiO_2 are presented in Figures 2.1 and 2.2.

Brookite has measured density of 4.13 g/cm^3 , Mohs' scale hardness of 5.5-6.0, dielectric constant of $\epsilon=78$, and refractive index of $n_\alpha=2.5831$, $n_\beta=2.5843$, and $n_\gamma=2.7004$ [4]. Brookite has been considered to be brittle, and generally it is less studied than the other two crystal structures, even experimentally. Although brookite is usually considered to be industrially uninteresting there are, however, some reasonable recent studies on brookite nanorods as highly active photocatalysts [5].

Anatase has measured density of 3.90 g/cm^3 , Mohs' scale hardness of 5.5-6.0, dielectric constant of $\epsilon=48$ (powder), and refractive index of $n_\omega=2.5612$ and $n_e=2.4880$ [4]. The experimental band gap of anatase TiO_2 is 3.2 eV, and the band gap is indirect.

Rutile is thermodynamically the most stable form of TiO_2 , and it can withstand high temperatures, whereas anatase and brookite are converted to rutile when heated. Rutile has quite high measured melting point of $1840 \pm 10 \text{ }^\circ\text{C}$, and density of 4.27 g/cm^3 [4]. It has Mohs' scale hardness of 6.0-6.5, dielectric constant of $\epsilon=110$ -117, and refractive index of $n_\omega=2.6124$ and $n_e=2.8993$ [4]. Rutile has experimentally measured direct band gap of 3.0 eV.

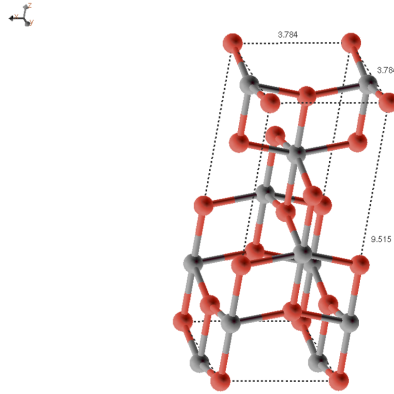


Figure 2.1: Structure of bulk anatase TiO_2 . Titanium atoms are presented with gray color and oxygen atoms with red. The lattice parameters are given in Ångströms.

The bonding in TiO_2 compound is interesting because of its semi-ionic nature. Due to much stronger electronegativity of oxygen, the shared electrons are closer to the oxygen atom, causing the titanium atom to have positive charge when the oxygen becomes negatively charged. That is the reason for the ionic nature for the bonding. In compounds titanium is usually present with oxidation number +IV and oxygen with oxidation number -II. The TiO_2 molecule is thus charge neutral, and this is also the case with stoichiometric clusters. The electron configuration for titanium is $1s^2 2s^2 2p^6 3s^2 3p^6 4s^2 3d^2$, and $1s^2 2s^2 2p^4$ for oxygen [6].

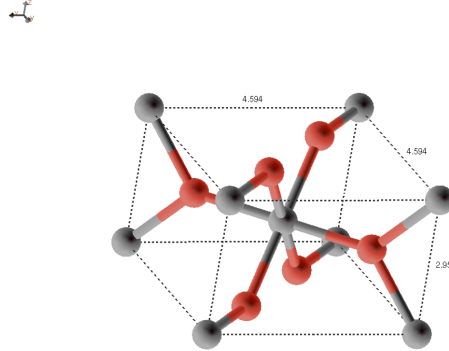


Figure 2.2: Structure of bulk rutile TiO_2 . Titanium atoms are presented with gray color and oxygen atoms with red. The lattice parameters are given in Ångströms.

As it was already mentioned, in the case of the bulk quantities rutile is the most stable crystal structure of TiO_2 . In the case of nanoparticles, however, the anatase structure becomes more favourable. This has been observed experimentally for example in the case of the TiO_2 thin layers [7]. The driving force behind this phase transformation are the surface energetics of different TiO_2 surfaces. The nanoparticle is a closed object, limited by surface boundaries. In the case of the nanoparticles the surface-to-bulk ratio is drastically increased when compared to larger particles, and the different surface energetics start to play a more and more important role in the particle energetics.

In 1998 Zhang and Banfield performed thermodynamical analyzes on phase stability of nanocrystalline anatase and rutile [8]. The earlier experimental studies of Penn and Banfield [9] had indicated that anatase clusters are dominated by 101 surfaces [9], while rutile clusters are usually dominated by 110 surfaces according to computational results of Ramamoorthy *et al.* [10]. Zhang and Banfield concluded that when the particle size is reduced under *ca.* 14 nm, the anatase structure becomes more stable than rutile [8]. The reason for the change in phase stability is the higher free energy of rutile, arising from the energetics of the dominating surface facet types in such small particles [8].

Due to the above-mentioned change in the phase stability, nanoparticle studies are usually performed on anatase structured particles. In my studies I have also concentrated on the properties of anatase structured particles. The rutile structured particles would also be interesting due to their copious usage as pigments. When

we deal with ultra-small nanoparticles we can model also rutile by using anatase particles, because it has been found in the computational studies that the distinction between anatase and rutile is minor at small particle sizes [11].

2.2 Quantum-size effect

When dealing with semiconductor nanoparticle physics, the phenomenon commonly known as the quantum-size effect [12, 13, 14, 15] can not be neglected. The phenomenon was originally explained in general case of semiconductor nanoparticles in 1984 by Brus, who linked the observed spectral blue-shifts in semiconductor nanoparticles with the confinement of the electron wave functions [12]. Brus concluded that the effective band gap broadening can be observed when the size of the semiconducting particle becomes smaller than the exciton radius. In this situation hole and electron are forced to form a confined bound state (Wannier exciton). The theoretical model predicted that with large band gap materials the effect should be visible when particle diameters are smaller than about 60 Å, and with small band gap materials the effect can be visible even with relatively large crystal sizes [12]. The original model was later improved in 2008 by Satoh *et al.* [16], by a model based on the Nosaka equation [17], using a finite depth potential well. All the theoretical models for quantum-size effect predict blueshifts caused by discretized levels in band gap edges, appearing as a larger effective band gap, but also excitonic peaks are likely to appear in the spectrum [12, 13, 14, 15, 16].

The earlier studies on the TiO₂ nanoparticles include both experimental and theoretical methods. Generally the observed quantum size effects are visible in the region where the size of the particle becomes comparable with the mean free path of the electron in the material [18]. In the case of TiO₂ the calculated threshold of the particle diameter varies with the reduced effective mass of the charge carriers used in the calculation, and usually the threshold diameter ranges from 0.6 nm to 3.8 nm [19, 20]. In 2006 Lundqvist *et al.* computationally proved that the quantum size effect causes a significant band gap broadening in TiO₂ nanoparticles when the size of the particle is between 1-2 nm, and under 1 nm further widening of the gap is limited by the effect of surface defect sites [18]. However, Anpo *et al.* have previously reported experiments showing quantum size effects for the anatase particles in the range of 3.8-53 nm, and for rutile particles in the range of 5.5-200 nm [21]. Quite the opposite was reported by Serpone *et al.* in 1995 [22]. In their experiments Serpone *et al.* did not find any any evidence of the quantum size effect at all, with the TiO₂ particles having mean diameters of 2.1 - 26.7 nm [22]. The discrepancy is evident.

In 2003 Persson *et al.* concluded in their computational studies on smallest possible semi-ionic cluster structures, that when we pay particular attention to strict criteria of stoichiometry, high coordination, and balanced charge distribution when creating model clusters, the resulting TiO₂ structures have defect-free band structures, and exhibit strong quantum-size effect [23]. When we further consider the studies of Persson *et al.* we will have to carefully consider that they have used selected unrelaxed crystal structures for the particles, so that they can prove their assumptions for defect-free structures. The chemical and physical picture of bonding and surface reconstruction during the relaxation process can lead to significantly different structures, as we will later show in Chapter 4 in the case of publication IV.

We should also bear in mind that the large band gap broadening of the Brus model does not take any surface reconstructions and changes in bonding into account [12]. The model also neglects the possible surface states [12]. As regards to computational results, and the discrepancy in size region where the quantum-size effects are seen, one should bear in mind that computational models always make a compromise between accuracy and the computational power needed.

2.3 Dye-sensitization of TiO₂

Depending on the crystal structure, the band gap of bulk TiO₂ is around 3 eV which corresponds roughly to 413 nm wavelength, and therefore TiO₂ absorbs radiation mainly at the UV-region. When nanoparticles experience band gap broadening due to quantum-size effect, the absorption threshold is moved towards even shorter wavelengths. In practice this means that most of the visible light is unable to create excitations in TiO₂ when we are dealing with photo-active applications, such as self-cleaning surfaces and solar cells. In order to overcome this problem, and improve the efficiency of photo-applications of TiO₂, we should be able to alter the band structure of TiO₂ or use other means to increase the light-harvesting performance of the system.

During the last two decades, there has been a substantial increase in solar cell technology, and TiO₂ nanoparticles have found increasingly interesting applications in the field of organic and inorganic DSSCs, which are considered as a good alternative to solid-state *p-n* photovoltaic devices [24, 25, 26, 27, 28]. The most typical form of DSSC is the so called Grätzel cell, where the semiconductor is anatase-like TiO₂ and the used dyes are ruthenium-oligopyridine complexes [29, 30]. The key element in the operation of DSSC is the charge injection, which happens from the excited states of the dye molecule at the surface of the nanoparticle, to the conduction band states within the nanoparticle itself [31]. In order to improve the efficiency

of DSSCs, the band gap and chemical potential of the nanoparticle must carefully match with the sensitizing dye.

The schematic operation principle of DSSC is presented in Figure 2.3. The usual structure is based on the mesoporous TiO_2 film, which is composed of TiO_2 nanoparticles which have been sintered together. The individual nanoparticles have diameters of 10-30 nm and the thickness of the mesoporous film is usually 10 μm [24]. The mesoporous TiO_2 film is placed on top of the layer of transparent conducting oxide, which is deposited on top of glass or plastic substrate. The most typical transparent conducting oxide is the fluorine-doped tin oxide (FTO) [24]. The sensitizing dye is deposited as a monolayer on top of the mesoporous TiO_2 , and the dye molecules further adsorb on the surfaces of TiO_2 nanoparticles in the mesoporous layer. This layered oxide-semiconductor-dye structure acts as an anode, which is separated from the counter electrode by an electrolyte. Typically this electrolyte is an organic solvent containing the iodide/triiodide redox system (I^-/I_3^-) [24]. The cathode is composed of glass-FTO structure covered by a thin layer of platinum catalyst (platinum nanoparticles) [24].

The operation principle of DSSC is the following: Illumination by light creates excited electrons in the dye molecule, and these electrons are injected on the conduction band of the TiO_2 nanoparticle. The oxidised dye is then restored by capturing electron from iodide in the electrolyte, and this process prevents the electrons injected to the TiO_2 to be recombined back to the dye [24]. The oxidation of I^- forms I_3^- ions, which are diffused through the electrolyte [24]. At the cathode the regenerative cycle is completed by electron transfer, when I_3^- reduced to I^- [24].

In DSSC, the interactions in oxide-dye-electrolyte interfaces are quite complex, and dependent also on external factors, which include solar radiation intensity, operating temperature, and operating conditions [24]. The numerous choices for dye-electrolyte combinations offer us a great potential to improve the performance of DSSCs. When considering the sensitizers, Ru-complexes have been considered as a good choice, but also osmium and iron complexes along with other classes of organometallic compounds have been developed [24]. As an electrolyte the solvents having I^-/I_3^- -redox couple have been considered as a good choice. Organic nitrile-based solvents seem to yield high efficiencies, and on the other hand gelification of the solvent or ionic liquids offer improved stability [24].

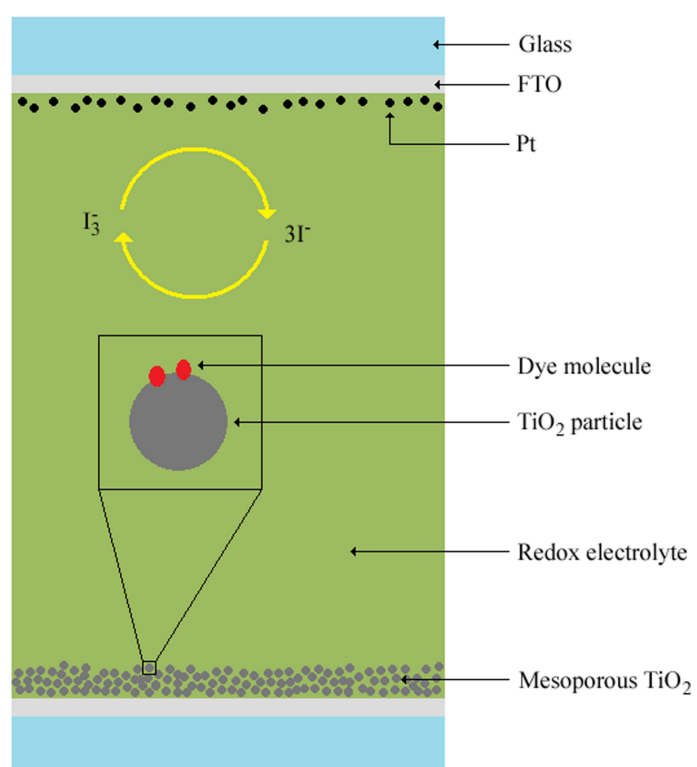


Figure 2.3: The schematic presentation of the structure and operation principle of DSSC.

Chapter 3

Theory

In this chapter I go through the background theory of computational methods, and briefly explain the software packages used. I begin with a short introduction of density functional theory (DFT) and time-dependent density functional theory (TDDFT). Because the DFT has been reviewed in numerous publications and theses, we only deal with general description of the method here. After the foundations of the theories used by the programs, I shortly describe GPAW, VASP, and Gaussian 09 packages used in the practical calculations.

3.1 Density functional theory

DFT is based on the idea that all the ground state properties of the system of interacting particles can be derived from the ground state electron density $n_0(\mathbf{r})$ of the system. The origin of DFT is in the method proposed by Thomas [32] and Fermi [33] in 1927. The original Thomas-Fermi method approximated the kinetic energy of the system as an explicit functional of the density, simplified as non-interacting electrons in homogeneous gas. This homogeneous electron gas is supposed to have a density equal to the local density at any given point. In the first approximation the exchange and correlation among the electrons was neglected, but this was later implemented by Dirac [34]. The functional for energy in the case of electrons in an external potential $V_{ext}(\mathbf{r})$ has been given in the literature [35] as

$$\begin{aligned} E_{TF}[n] = & \left(\frac{3(3\pi^2)^{\frac{2}{3}}}{10} \right) \int d^3r n(\mathbf{r})^{5/3} + \int d^3r V_{ext}(\mathbf{r})n(\mathbf{r}) \\ & + \left(-\frac{3}{4}(3/\pi)^{\frac{1}{3}} \right) \int d^3r n(\mathbf{r})^{4/3} + \frac{1}{2} \int d^3r d^3r' \frac{n(\mathbf{r})n(\mathbf{r}')}{|\mathbf{r} - \mathbf{r}'|}. \end{aligned} \quad (3.1)$$

In equation 3.1 the first term is the local approximation of the kinetic energy, the third term is the local exchange and the last term is the Hartree energy. Now the ground state of the system can be found by minimizing the $E[n]$ for all $n(\mathbf{r})$. This original Thomas-Fermi method is a fine example of how the DFT works, but it is far too inaccurate for present day electronic structure calculations. [35]

The modern DFT is based on the theorems of Hohenberg and Kohn [36]. These theorems formulate DFT as an exact theory of many-body systems:

Theorem I: For a system of interacting particles in an external potential, the external potential $V_{ext}(\mathbf{r})$ is uniquely determined by the ground state density $n_0(\mathbf{r})$. [35]

Theorem II: For any external potential $V_{ext}(\mathbf{r})$, we can define a universal functional for energy $E[n]$ in the terms of density $n(\mathbf{r})$, and the global minimum for $E[n]$ as a function of $n(\mathbf{r})$, represents the exact ground state and the ground state density of the system. [35]

Based on these two theorems, the energy functional can now be formulated as [35]

$$E_{HK} = T[n] + E_{int}[n] + \int d^3r V_{ext}(\mathbf{r})n(\mathbf{r}) + E_{II}. \quad (3.2)$$

In equation 3.2 $T[n]$ is the internal kinetic energy of the system, $E_{int}[n]$ is the internal potential energy, and E_{II} represents the interaction energy of the nuclei. [35]

The reason for DFT to be the most used method for electronic structure calculations today is the Kohn-Sham ansatz introduced in 1965. Kohn and Sham stated that the rather complicated many-body problem can be replaced with an auxiliary independent-particle problem, which can be solved far more easily. The Kohn-Sham method is self-consistent, dealing with independent particles and interacting density. [35]

The famous Kohn-Sham ansatz is based on two assumptions:

I: The exact ground state of the system can be represented by the ground state of the auxiliary system of non-interacting particles. [35]

II: The auxiliary Hamiltonian can be selected so, that it has a usual kinetic energy operator and an effective local potential $V_{eff}^\sigma(\mathbf{r})$, which acts on the electron in the point \mathbf{r} , having a spin of σ . [35]

The first assumption has not been proven for real systems, but the method still gives reasonable results for real systems.

The Kohn-Sham approach can be used to rewrite the Hohenberg-Kohn expression in the following form [35]

$$E_{KS} = T_s[n] + \int d\mathbf{r} V_{ext}(\mathbf{r})n(\mathbf{r}) + E_{Hartree}[n] + E_{II} + E_{xc}[n]. \quad (3.3)$$

In this final form, $T_s[n]$ is the kinetic energy functional, $E_{Hartree}[n]$ is the classical Coulomb interaction energy of the electron density interacting with itself, E_{II} is the interaction between the nuclei, $V_{ext}(\mathbf{r})$ is the external potential due to the nuclei and any other external fields, and $E_{xc}[n]$ represents the exchange-correlation energy including all many-body effects. [35]

The accuracy issues of DFT are strongly dependent on the quality of the exchange-correlation functional [37], because the exact exchange-correlation energy is not generally known. This is why we will have to rely on approximations for the exchange-correlation functional, and during the history of DFT many different approximations have been developed. The first commonly used one is the original local density approximation (LDA), in which the exchange-correlation energy is approximated by the exchange-correlation energy of the homogeneous electron gas [37].

The general problem with the LDA is the overbinding and the overly large cohesive energies [37]. To overcome this, the gradient of the density in exchange-correlation energy was also included in the approximation, leading to the generalized gradient approximation (GGA). Despite the improvements of GGA when compared to LDA, there are still problems with the accuracy of DFT calculations. It is a generally known fact that GGA methods tend to underestimate the band gap of the semiconducting systems. The amount of the underestimation varies considerably between different systems, and in the case of bulk TiO_2 the underestimation is around 1 eV, which can be considered as substantial in the energy scale of the atomic systems.

The known drawbacks of the DFT method have led to the development of numerous new exchange-correlation functionals, including also several hybrid functionals such as PBE0 [38, 39], HSE [40, 41], and B3LYP [42]. This class of functionals has been named “hybrid“ because they are constructed as combinations of orbital-dependent Hartree-Fock exchange, LDA or GGA, and possibly empirically adjusted coefficients [35]. Generally the hybrid functionals have been known to reproduce experimental band gaps well in the case of bulk structures. However, it has recently been shown that there can be problems in reproducing experimental band gaps for surfaces or nanoparticle systems, and also the absolute reliability of the hybrid functionals can

be questioned [43].

3.2 Time-dependent density functional theory

As we stated in the previous chapter, the original Kohn-Sham ansatz replaces the many-body problem with a problem of non-interacting particles, leading to a situation where we deal with independent particles with interacting density, and the basic DFT is a ground state method. Basic DFT lacks the ability to model any time-dependent phenomena such as optical excitations. The problem is that the eigenvalues of independent particles do not correspond to the real addition or removal energies of the electron. Neither do the differences between eigenvalues correspond to real excitation energies. [35]

In the original full many-body problem, the excitations are present as response functions, and the density response function as a function of frequency has poles at the excitation frequencies. This can be used in deriving the dynamic density response in the Kohn-Sham framework. [35] DFT has been further developed to time-dependent Kohn-Sham density functional theory (TDDFT) [44] by utilizing the time-dependent Schrödinger-like equation [35]

$$i\hbar \frac{\partial \psi_i(t)}{\partial t} = \hat{H}(t) \psi_i(t), \quad (3.4)$$

in which $\psi_i(t)$ are the independent particle wave functions, and $\hat{H}(t)$ is the Hamiltonian of the system. The time-dependent effective Hamiltonian of 3.4 can now be formulated as [35]

$$\hat{H}_{eff}(t) = -\frac{1}{2} \nabla^2 + V_{ext}(\mathbf{r}, t) + \int \frac{n(\mathbf{r}', t)}{|\mathbf{r} - \mathbf{r}'|} d\mathbf{r}' + V_{xc}[n](\mathbf{r}, t). \quad (3.5)$$

We should note that the $V_{xc}[n](\mathbf{r}, t)$ is a **function** of \mathbf{r} and t and a **functional** of $n(\mathbf{r}', t')$. [35]

The main problem of the recent theory of TDDFT is that it is not known how to define a universal function of time, since it should depend upon the density at previous times. The simplest approximation used is that V_{xc} is approximated based on density at time t , neglecting the memory effects. [35]

When we approach the TDDFT with explicit real-time calculations, we are able to model also the non-linear phenomena, such as laser pulses, because we are not limited to small perturbations in the system, as is the case in traditional linear re-

sponse approach. The real-time approach is also better in the case of large systems, since only the occupied electron states are evolved in the calculation, and the calculations scale linearly with the size of the modeled system. [35]

One way to perform the calculations is to iteratively propagate the time-dependent Schrödinger equation in steps in real time. This can be done by expanding the one-particle states $\psi_i(t)$ in a fixed time-independent basis [35]

$$\psi_i(t) = \sum_{\alpha} c_{i,\alpha}(t) \chi_{\alpha}, \quad (3.6)$$

and then the iteration from time t^n to time $t^{n+1} = t^n + \delta t$ can be given as [35]

$$c_{i,\alpha}^{n+1} = \sum_{\alpha'} [e^{-i\hat{H}\delta t}]_{\alpha,\alpha'} c_{i,\alpha'}. \quad (3.7)$$

The \hat{H} in Equation 3.7 is a matrix in the basis α, α' . Because \hat{H} must be considered constant over the time step there is a length limitation for the time step δt . The \hat{H} should be updated as a function of time-dependent density, which can cause important issues with efficiency. [35]

In practical calculations the expansion of the exponential can be done by using the Crank-Nicholson operator [35]

$$c^{n+1} = \frac{1 - i\hat{H}\frac{\delta t}{2} + \dots}{1 + i\hat{H}\frac{\delta t}{2} + \dots} c^n. \quad (3.8)$$

With this method the expansion of the exponential is unitary, preserving the orthonormality of the states for an arbitrary δt . The method is also explicitly time-reversal invariant, and conserves energy for time-independent Hamiltonians. In practice the energy is satisfactorily conserved, even if the Hamiltonian changes with time, with a suitable selection for δt . [35]

TDDFT calculations can be used for the study of the optical properties of finite size systems, such as clusters. The key element in these calculations is the dipole strength function $S(\omega)$. The dipole strength function is proportional to the experimentally measured absorption cross-section, which can be considered as a measure for the probability for a light quantum to be absorbed by the system. The actual calculation of the dipole strength function is based on the polarizability [35]

$$S(\omega) = \frac{2m}{\pi e^2 \hbar} \omega \text{Im}\alpha(\omega). \quad (3.9)$$

The polarizability can be calculated by using relation [35]

$$\alpha(\omega) = \frac{d(\omega)}{E(\omega)}, \quad (3.10)$$

where $d(\omega)$ is the dipole moment, and $E(\omega)$ is the applied electric field.

Practical calculation of the polarizability is done by finding the equilibrium ground state $\psi_i^{\bar{E}}$ for the system in an applied electric field \bar{E} , which has the polarisation direction \hat{x} . In this case the system has a time-independent Hamiltonian $\hat{H} = \hat{H}_0 - e\bar{E}_x$. At the time $t = 0$, the the applied field \bar{E} is suddenly removed, and the system is allowed to freely evolve for propagated time $t > 0$, with the initial independent-particle states $\psi_i^{\bar{E}}$ and the hamiltonian \hat{H}_0 . The actual output of the calculation will be the dipole strength function $S(\omega)$, and optical constants, such as dielectric function, can be further extracted and derived from this data. [35]

3.3 Projector augmented wave method

Working with DFT requires a method to deal with wave functions of atoms in computational crystal structure. The problem is that electron wavefunctions can have large oscillations near the nucleus, although they behave quite smoothly at a large distance. As the number of electrons in the calculation increases, the handling of all-electron wave functions soon becomes computationally demanding. All the methods for representing the basis for electron wave functions rely on the principle that many chemical interactions and phenomena, such as bonding and absorption, are more or less dictated by the valence electrons, whereas the states of tightly bound core electrons remain quite unchanged. Thus neglecting or simplifying the behavior of the core electrons can lower the computational load during the modeling.

Representing the electron wavefunctions in the computational model can be done by using numerical orbitals, plane waves, or tables. The plane waves provide a natural basis to represent the electron wave functions due to the simplicity of operations, and have been widely used in DFT modeling software. With plane waves, the electronic wavefunctions of core electrons have been handled with many different ways, but the main method used in this study is the projector augmented wave method (PAW) [45, 46]. The computational codes GPAW and VASP, which are the main tools used in my studies, rely on the PAW method.

The PAW method is a computationally very efficient all electron method, which is based on representing the electron wavefunctions with plane waves. In this method

an augmentation sphere is included surrounding each nucleus in the lattice, and outside this augmentation sphere, the wave functions are presented with normal smooth plane waves. Inside the augmentation sphere the wave functions are presented with projectors and auxiliary localized functions, just as in the case of “ultrasoft” pseudopotentials [47, 35].

The important difference of PAW when compared to pseudopotentials is that in PAW method also the full all-electron wavefunction can be preserved. Because the full wave function oscillates heavily around the nucleus, all integrals in the PAW method are evaluated as a combination of integrals of smooth functions outside the augmentation spheres, plus contributions from radial integration over augmentation spheres. [35]

The basic formalism is that the smooth part of the wavefunction $\tilde{\psi}_v$ is related to the all-electron wavefunction ψ_v by a linear transformation [35]

$$\psi_v = \mathcal{T}\tilde{\psi}_v. \quad (3.11)$$

The transformation \mathcal{T} is expected to be unity outside the augmentation sphere, and within the augmentation sphere it has a form of $\mathcal{T} = 1 + \mathcal{T}_0$ [35].

Inside the augmentation spheres, we can use Dirac notation to formulate the expansion of smooth functions in partial waves m as [35]

$$|\tilde{\psi}\rangle = \sum_m c_m |\tilde{\psi}_m\rangle, \quad (3.12)$$

and thus the correspondence to the all-electron wavefunction becomes [35]

$$|\psi\rangle = \mathcal{T}\tilde{\psi} = \sum_m c_m |\psi_m\rangle. \quad (3.13)$$

The full wavefunction in all the space can now be written as [35]

$$|\psi\rangle = \tilde{\psi} + \sum_m c_m \{|\psi_m\rangle - |\tilde{\psi}_m\rangle\}. \quad (3.14)$$

Because the transformation has to be linear, the coefficients must be given as a projection inside the augmentation sphere [35]

$$c_m = \langle \tilde{p}_m | \tilde{\psi} \rangle, \quad (3.15)$$

where \tilde{p} is some set of projection operators.

3.4 Computational details

The actual computational details are presented in each Publication in the computational details sections, so I do not fully cover the details here. Instead I make a short overview of the computational codes used in this study.

3.4.1 GPAW

Most of the calculations done for this study have been performed by using the GPAW software package. GPAW is a real-space grid based calculator using DFT with PAW method. The GPAW software was originally selected as a primary tool because it offers a possibility to perform calculations with non-periodic boundary conditions. This is an excellent way to model nanoparticles without any problems arising from periodic images. The other great advantage of GPAW is its ability to perform TDDFT calculations, including also the possibility to calculate the photo-absorption spectra for non-periodic systems. [48, 49, 50, 51]

3.4.2 VASP

The other program package used in this study is Vienna *ab initio* simulation package VASP. VASP was used in Publication III for the DOS calculations, verified with GPAW, and it turned out to be quite efficient in the calculation of DOS plots for nanoparticles. VASP uses same the DFT+PAW approach as GPAW, but the primary difference is that VASP is not able to perform calculations with non-periodic boundary conditions. [52, 53, 54, 55, 56, 57]

3.4.3 Gaussian 09

The third modeling package used in this study is Gaussian 09, which is the most recent version of this software favoured by quantum chemists. Gaussian 09 can be used to model energies, molecular structures, vibrational frequencies, and properties of molecules, and also reactions in a wide variety of chemical environments. Gaussian 09 offers a wide variety of methods, and thus it is suitable for modeling the full range of chemical systems for the entire periodic table. [58, 59]

Chapter 4

Review of the modeling results

In this chapter I will make a review of the modeling results. This chapter is based on four publications dealing with different aspects of the nanoparticle properties. The topics dealt within these publications can be roughly divided under the following three sections. The order of chaptering is not chronological, but is based on different aspects of my PhD studies, starting on the structural and electronic properties of the cluster structures modeled, and ending up on derived refractive index functions for the modeled TiO₂ particles, and modeling of dye complexes for dye sensitization.

4.1 Structural and electronic properties

4.1.1 Stoichiometric nanoparticles with terminal Ti-O bonds

There has been a lot of debate about the lowest lying global energy minimum structures of small TiO₂ particles [18, 60, 23, 61, 62], so the choice of the model structures was not at all an easy task. In the beginning I studied carefully the well executed studies of Lundqvist *et al.* [18], Persson *et al.* [23], and Qu and Kroes [61]. Based on these previously done studies, I ended up using two different sets of cluster models in publication I. First set of structures (labeled A) were cut from the anatase bulk structure so that they would be as symmetric as possible, still maintaining as much of a bulk structure as possible. The other set of structures (labeled B) were cut from the anatase bulk structure so that the structures would be more needle-like, having one dimension clearly longer than the other dimensions. The most important thing to note here is that all the selected structures possess two or more terminal Ti-O bonds. This means that there are under-coordinated oxygen atoms, which are bonded to only one titanium atom. The structures used are presented in Figure 4.1. More detailed description of the structures is available in Publication I.

Based on the structural analysis it was seen that these nanoclusters tend to form more compact structures during the relaxation. In the smallest particles the average bond lengths were shorter, and when the size of the cluster becomes larger, the average bond length starts to grow towards the bulk value. This is clearly seen in Table 4.1 where the average bond lengths of the cluster models from publication I have been collected. The average bond lengths have been calculated from the structures by using a Python script which simply assumed that there is a Ti-O bond if the bonding distance is smaller than 2.15 Å, Ti-Ti bond if the bonding distance is smaller than 2.90 Å, and O-O bond if the bonding distance is smaller than 1.47 Å.

It was concluded that the reason for the structures to compress from the original truncated bulk structures during the relaxation is the increased surface-to-bulk ratio. The phenomenon is exactly the same as it is in the case of the theory for relaxation of metal surfaces given by A. Groß[37]: the Smoluchowski charge smoothening leads to the reduction of the first interlayer spacing [63]. Another reason is that the optimal Ti-O bond length in the TiO₂ molecule is smaller (1.620 Å)[64] than in the bulk anatase structure (1.937 Å or 1.964 Å)[2], and the termination of the bulk symmetry on the cluster surface gives atoms on the surface more degrees of freedom, allowing the shorter optimal bonds.

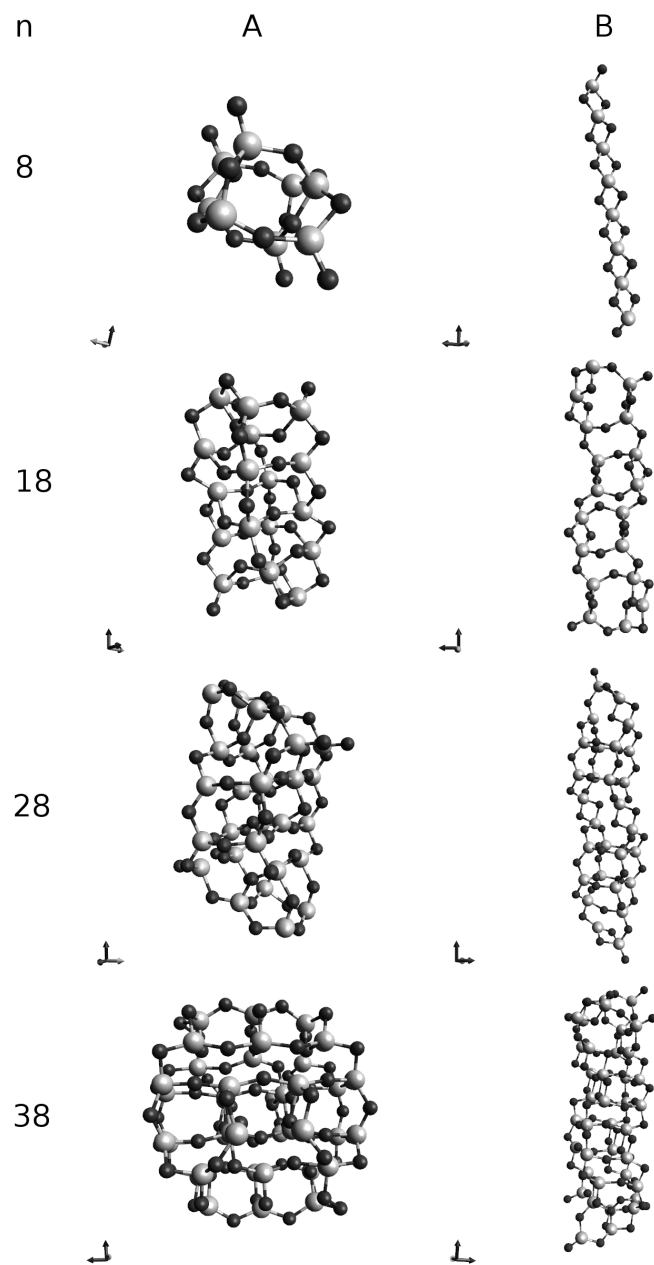


Figure 4.1: The relaxed $(\text{TiO}_2)_n$ A and B structures. Titanium atoms are presented with gray color and oxygen atoms with black.

Table 4.1: The average bonding lengths after the relaxation in A and B-structured $(\text{TiO}_2)_n$ particles. The values for anatase and rutile are from relaxed bulk structures.

| Structure | $d_{\text{Ti-O}}$ [Å] | $d_{\text{Ti-Ti}}$ [Å] | $d_{\text{O-O}}$ [Å] |
|------------------------|-----------------------|------------------------|----------------------|
| molecule | 1.71 | - | - |
| $(\text{TiO}_2)_2$ | 1.83 | 2.77 | - |
| $(\text{TiO}_2)_{8A}$ | 1.89 | 2.85 | - |
| $(\text{TiO}_2)_{8B}$ | 1.88 | 2.77 | - |
| $(\text{TiO}_2)_{18A}$ | 1.91 | 2.83 | - |
| $(\text{TiO}_2)_{18B}$ | 1.89 | 2.76 | - |
| $(\text{TiO}_2)_{28A}$ | 1.88 | 2.82 | - |
| $(\text{TiO}_2)_{28B}$ | 1.89 | 2.83 | - |
| $(\text{TiO}_2)_{38A}$ | 1.90 | 2.83 | 1.46 |
| $(\text{TiO}_2)_{38B}$ | 1.93 | 2.87 | - |
| anatase | 2.01 | - | - |
| rutile | 2.02 | - | - |

Based on the structural changes we can already expect changes in the electronic structure of the small particles. As a next step the density of states (DOS) was calculated for both sets of model particles along with bulk structures for reference data. The DOS for the structures are presented in Figures 4.2 - 4.4. As we can see from Figures 4.2 and 4.3, the DOS for the $(\text{TiO}_2)_2$ cluster differs fundamentally from DOS for bulk anatase. The states are very localized, and there is no clear band structure for valence band (VB) and conduction band (CB). When the particle size is increased, as we see from Figure 4.4, the localized states of the clusters start to grow towards the continuous band structure for VB and CB in the bulk structure.

The highest occupied molecular orbital (HOMO) - lowest unoccupied molecular orbital (LUMO) gaps for the particles are collected in Table 4.2. As we can see, the DOS results show clearly that small particles can have larger band gaps when compared to bulk values of TiO_2 . Here we have compared the gaps of the particles to the gap value of bulk anatase, because the particles are anatase structured. The calculated gap energy differences correspond well to the previously reported values of 0.1-0.6 eV [16]. It is worth noting that these results indicate structure related changes in the band gaps of the nanoparticles, because ground state based DFT calculations do not take any excitonic effects into account.

The interesting feature in the DOS results is that the band gaps of certain systems, for example $(\text{TiO}_2)_{38A}$, are suspiciously small when compared to bulk values. These very small gaps are obviously due to defect states possibly arising from low-coordinated oxygen atoms on terminal Ti-O bonds present in these structures.

These defect states can be occupied or unoccupied as we can see in Figure 4.4. The A and B-structures in publication I are stoichiometric, but still contain terminal Ti-O bonds, which are known to be energetically unfavoured. In the case of $(\text{TiO}_2)_{38,4}$ the small gap can also be partly explained with two O-O bonds present in the final relaxed structure.

Based on the DOS results of A and B-structures with terminal Ti-O bonds, I can conclude, that the structure of the nanoparticle plays an important role in the formation of the band structure. The excitonic effects, not visible in ground state DFT calculations, may enhance the quantum-size effect, but the structure dependent variations in the band gap of the particles are evident. TiO_2 nanoparticles may exhibit band gap broadening corresponding to the previously reported blue shifts, but this is strongly dependent on the cutting of the model structures. Because the electronic band structure is so sensitive to the structure and bonding environment of the particle, the accuracy level of the selected modeling method is emphasized. Small differences in relaxation schemes, modeling of interparticle forces, and convergence requirements for the final forces may affect the results significantly.

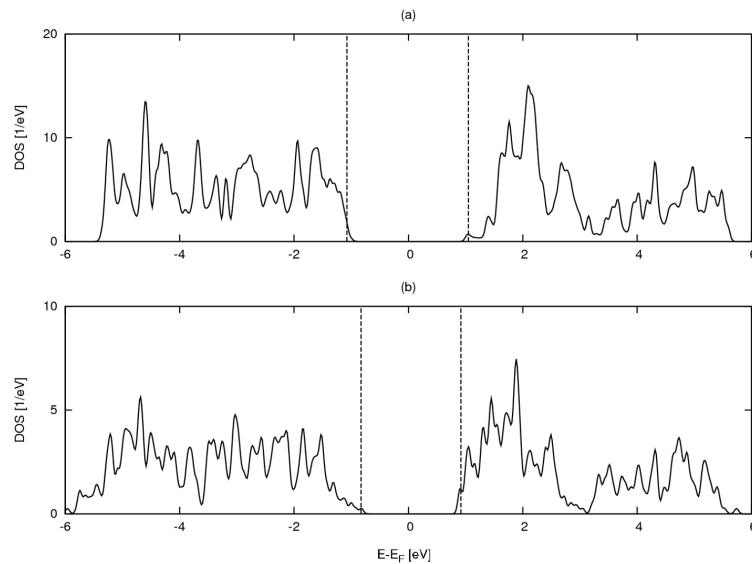


Figure 4.2: DOS for bulk anatase (a) and bulk rutile (b). HOMO and LUMO levels are marked with dashed lines. The energy is relative to the Fermi level

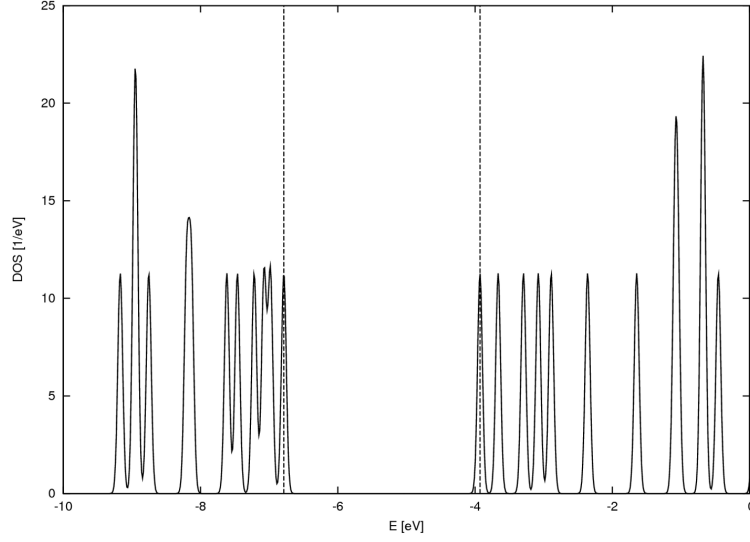


Figure 4.3: DOS for the $(\text{TiO}_2)_2$ cluster. HOMO and LUMO levels are marked with dashed lines. The energy is relative to the vacuum level.

Table 4.2: The HOMO-LUMO gaps of the A and B-structured TiO_2 particles, and the change of the gap when compared to the HOMO-LUMO gap of bulk anatase. The values for anatase and rutile are for bulk structures.

| Structure | HL gap [eV] | ΔE [eV] |
|------------------------|-------------|-----------------|
| $(\text{TiO}_2)_2$ | 2.86 | +0.74 |
| $(\text{TiO}_2)_{8A}$ | 2.01 | -0.11 |
| $(\text{TiO}_2)_{8B}$ | 2.79 | +0.67 |
| $(\text{TiO}_2)_{18A}$ | 2.22 | +0.10 |
| $(\text{TiO}_2)_{18B}$ | 1.33 | -0.79 |
| $(\text{TiO}_2)_{28A}$ | 1.03 | -1.09 |
| $(\text{TiO}_2)_{28B}$ | 1.99 | -0.13 |
| $(\text{TiO}_2)_{38A}$ | 0.37 | -1.75 |
| $(\text{TiO}_2)_{38B}$ | 1.86 | -0.26 |
| anatase | 2.12 | - |
| rutile | 1.75 | - |

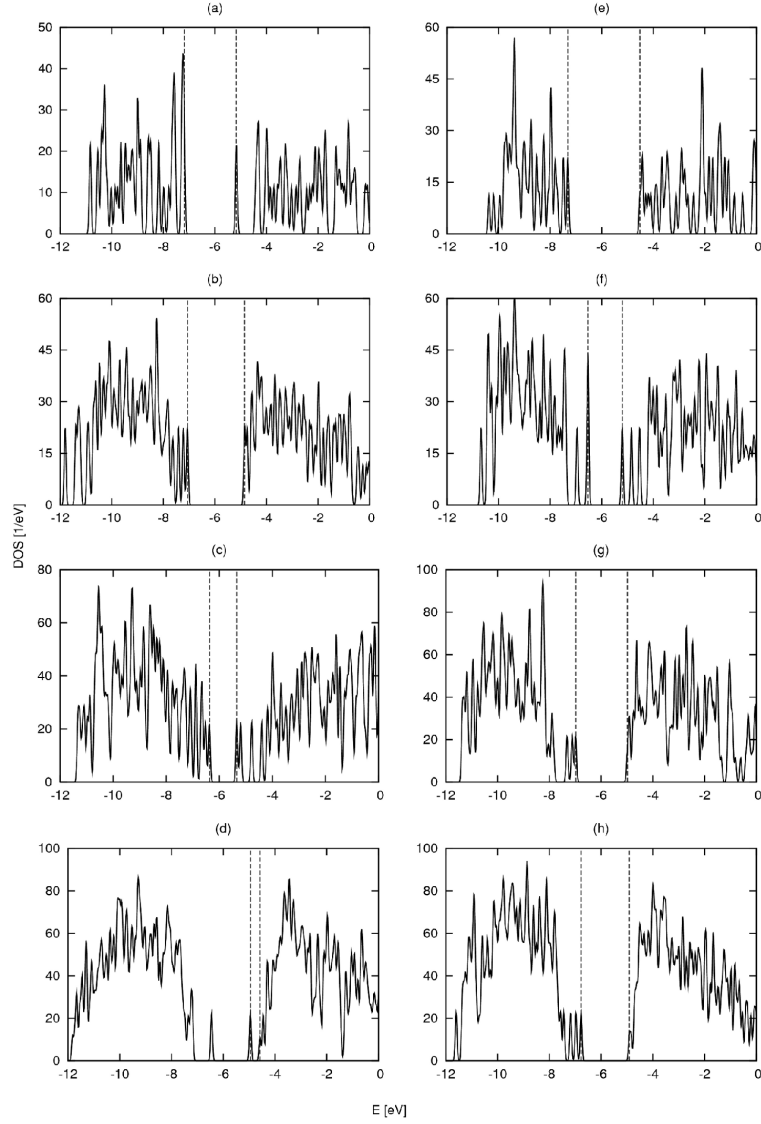


Figure 4.4: DOS for the A and B-model structures in Publication I. The left panel: Anatase structured $(\text{TiO}_2)_{8A}$ (a), $(\text{TiO}_2)_{18A}$ (c), $(\text{TiO}_2)_{28A}$ (e), $(\text{TiO}_2)_{38A}$ (g). The right panel: Anatase structured $(\text{TiO}_2)_{8B}$ (b), $(\text{TiO}_2)_{18B}$ (d), $(\text{TiO}_2)_{28B}$ (f), $(\text{TiO}_2)_{38B}$ (h). HOMO and LUMO levels are marked with red dashed lines. The energy is relative to the vacuum level.

4.1.2 Defect states in stoichiometric structures without terminal Ti-O bonds

In publication IV, the defect states noted in the previous subsection were studied more closely. We continued modeling of the stoichiometric particles, and paid more attention to the cutting process. The new model structures for anatase $(\text{TiO}_2)_{16}$, $(\text{TiO}_2)_{22}$, $(\text{TiO}_2)_{38}$, and $(\text{TiO}_2)_{46}$ were cut again from the experimental anatase bulk. The starting requirements in model cutting were that all the oxygen atoms should have coordination number of at least two, all titanium atoms should have coordination number of at least two, and the structures should still be stoichiometric.

The DOS results modeled with GPAW for these structures are presented in Figure 4.5. As it was expected, in the case of $(\text{TiO}_2)_{16}$, $(\text{TiO}_2)_{22}$, and $(\text{TiO}_2)_{46}$ the DOS of the particles showed defect free and well formed band gaps, supporting the size-dependent band gap broadening. But in the case of the $(\text{TiO}_2)_{38}$ cluster, the structure still possesses an *unoccupied* defect state at -4.8 eV. This is surprising, because the $(\text{TiO}_2)_{16}$, $(\text{TiO}_2)_{22}$, $(\text{TiO}_2)_{38}$, and $(\text{TiO}_2)_{46}$ clusters have seemingly similar and defect free structures.

The $(\text{TiO}_2)_{38}$ and $(\text{TiO}_2)_{22}$ structures were selected for closer examination, because of their feasible size. We started to study the source of the defect states more closely in these two structures, and the results of this part of the study are presented in publication IV. Based on the GPAW results, we were able to determine that the defect states appearing in the energy gap of the $(\text{TiO}_2)_{38}$ cluster, are titanium *d*-states. The preliminary GPAW results were further complemented with VASP calculations and the final conclusion was, that the defect states are Ti 3*d* states of three-fold coordinated titanium atoms at the corners of the $(\text{TiO}_2)_{38}$ cluster.

The VASP results for the total DOS of $(\text{TiO}_2)_{22}$ and $(\text{TiO}_2)_{38}$ are presented in Figure 4.6 (a) and (b). As we can see there is a slight difference when we compare the results to the ones modeled with GPAW, but the basic features are the same. Based on the VASP calculations we concluded that in the case of the $(\text{TiO}_2)_{38}$ cluster the unoccupied 3f-Ti 3*d* defect state is located at lower energy level because of the effective sub-cluster formation at the edges of the cluster. The structures of $(\text{TiO}_2)_{22}$ and $(\text{TiO}_2)_{38}$ are presented in Figure 4.7 (a) and (b), and the fundamental differences between these two structures are emphasized with black rectangles in the figure.

As we can see in Figure 4.7, the corners of the $(\text{TiO}_2)_{38}$ cluster actually form $(\text{TiO}_2)_2$ clusters, which are quite loosely connected to the main cluster. These sub-clusters have their own DOS, which is located at lower energy levels when compared to the

total DOS of the main cluster. The results of this sub-clustering during the relaxation process is that some of the states of the sub-cluster are visible as empty states in the bandgap of the main cluster. A more detailed study of the DOS results is presented in publication IV.

Based on these results we can conclude that these unoccupied $3d$ defect states are real, and not just computational artefacts due to the modeling method chosen. In real-life situation these states might become occupied due to doping or impurities, but in computational model the surrounding oxygen atoms are more electronegative, so the excess electrons end up to those atoms, lifting the defect state above Fermi level. The existence of these unoccupied gap states in stoichiometric nanoclusters opens up new ways of tuning the bandgaps in the applications of TiO_2 nanoparticles. On the other hand, we see once again the extreme structural sensitivity of the electronic structure of the nanoclusters.

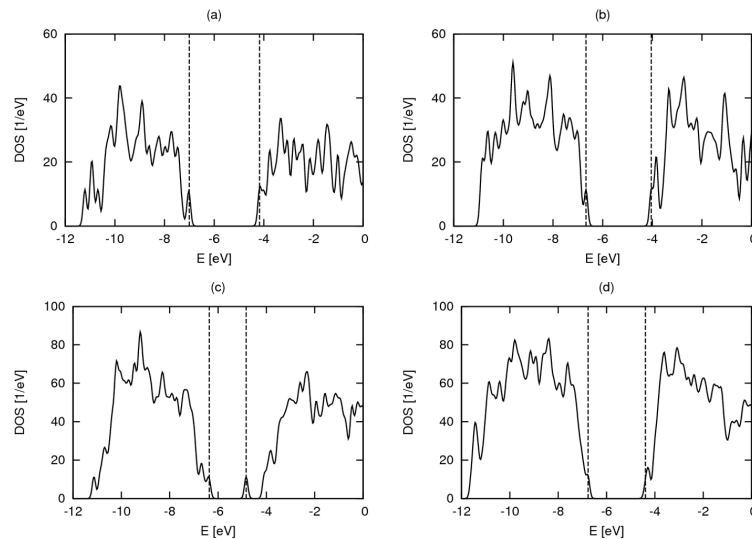


Figure 4.5: DOS for the adequately coordinated stoichiometric anatase nanoparticles. $(\text{TiO}_2)_{16}$ (a), $(\text{TiO}_2)_{22}$ (b), $(\text{TiO}_2)_{38}$ (c), and $(\text{TiO}_2)_{46}$ (d). HOMO and LUMO levels are marked with dashed lines. The energy is relative to the vacuum level. DOSs have been modeled with GPAW.

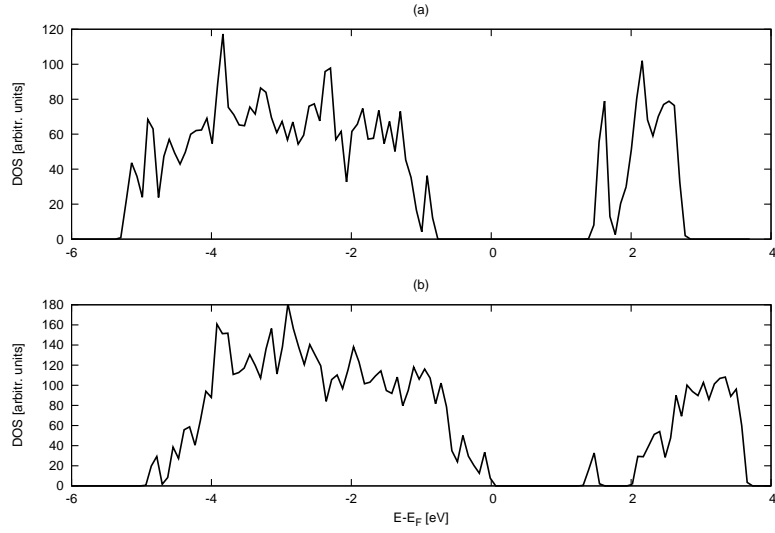


Figure 4.6: Total DOS for $(\text{TiO}_2)_{22}$ (a) and $(\text{TiO}_2)_{38}$ (b). The energy is relative to the Fermi level. The DOSs have been modeled with VASP.

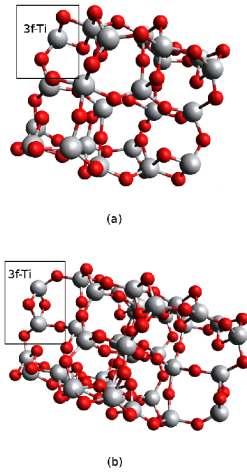


Figure 4.7: The structures for $(\text{TiO}_2)_{22}$ (a) and $(\text{TiO}_2)_{38}$ (b). Titanium atoms are presented with gray color and oxygen atoms with red. The fundamental differences between these two structures are emphasized with black rectangles.

4.2 Absorption characteristics and optical properties

In publication I we also modeled the photoabsorption spectra for the A and B structures. The total averaged photoabsorption spectra for the selected model particles are presented in Figure 4.8. The more detailed photoabsorption spectra for the structures in x, y, and z polarization directions are presented in publication I. As we can see in Figure 4.8 and the Figures in publication I, in the case of the symmetric particles, the basic absorption characteristics do not change much as a function of particle size, at least within this rather limited size range. In publication I we also concluded that the shape of the particle dominates the characteristics of total averaged photoabsorption spectrum so that in needlelike structures the longest dimension has strongest effect on the overall absorption characteristics. This is clearly visible also in Figure 4.8, as we can see that B-structures have more deviation in the shapes of the photoabsorption spectra.

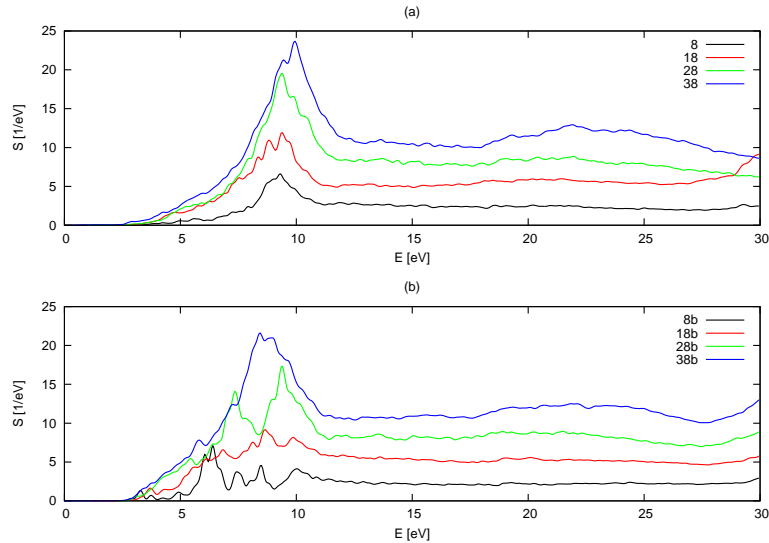


Figure 4.8: The total averaged photoabsorption spectra for selected $(\text{TiO}_2)_{nA}$ structures (a), and for $(\text{TiO}_2)_{nB}$ structures (b).

The photoabsorption results also indicate that the first allowed excitation energy can be 1.32 eV larger than the DFT HOMO-LUMO gap would predict. This is understandable as we consider the approximations made in standard ground state DFT calculations, and the tendency of DFT to underestimate the fundamental

band gap of semiconducting materials. The peak absorption for these ultra small TiO_2 clusters is located roughly around 8-9 eV for A-structures and for most of B-structures. Some of the B-structures have absorption peaks at lower energy levels. This indicates quite significant spectral blueshifts when compared to the absorption characteristics of the bulk TiO_2 phases.

Based on these photoabsorption results, we further calculated the refractive index functions (RIFs) for the modeled particles. The RIF results and derivation of RIF from photoabsorption spectrum data is presented in Publication II. One necessary approximation done in this process was the scaling of the RIFs to match the steady state absorption level. As we can see in Figure 4.8 the level of photoabsorption is increased as a function of (TiO_2) -units in the cluster. Without any scaling the RIFs of the particles would also increase as a function of the particle size. In publication II we present in detail the scaling based on the amount of (TiO_2) -units and the shape dependent scaling factor.

The total averaged RIFs for A structures along with RIF for the $(\text{TiO}_2)_2$ cluster are presented in Figure 4.9, and for B structures along with RIF for $(\text{TiO}_2)_2$ cluster in Figure 4.10. For comparison, the experimental data for anatase structured bulk TiO_2 by Jellison Jr. *et al.* [65] and Hosaka *et al.* [66] is presented in Figure 4.11.

A more detailed analysis of the RIFs of the A- and B-structures including x, y, and z polarization directions is presented in Publication II. Based on the results reported in Publication II we can conclude that RIFs of the nanoparticles show significant blueshifts. The average blueshift is 131 nm in the imaginary part of the RIF when we compare the results to the bulk data from Jellison Jr. *et al.* [65], and 101 nm when we compare the results to the bulk data from Hosaka *et al.* [66].

The results for RIFs of x, y, and z polarization directions of the nanoparticles also indicates an increase in anisotropy when compared to bulk structure. This is clear, when the RIFs of x and y polarisation directions differ from each other, as we can see in Figures 2-7 in publication II. The RIF results also indicate that in the case of ultrasmall TiO_2 particles, the structure of the particle may have a more pronounced effect on the RIF than the size of the particle, just as it was already shown in the case of photoabsorption spectra. We can also note that the weight of the RIFs moves toward shorter wavelengths when the particle size is decreased.

What is worth noting in here is that in real-life situations the TiO_2 nanoparticles are often in various solutions, so the results modeled for the particles in absolute vacuum do not necessarily reveal the whole truth behind the absorption phenomena. Once the refractive index function of the particles in vacuum is known, one can simply add

the effect of the surrounding medium by multiplying the refractive index function of the particles by the refractive index function of the suspending medium. Although this is a widely used procedure in the macroscopic world, it is not totally reliable in the microscopic scale. With macroscopic quantities, the surface-to-bulk ratio is small, and possible effects arising from surface chemistry and surface reconstructions play a minor role when compared to the larger scale phenomena. In the case of nanoparticles, simple multiplication of the RIFs ignores the previously mentioned effects, which in this size range can have a significant effect. The modeling results reveal that the anisotropy and blueshifts of the particle RIFs have to be taken into account in the turbidity spectrum measurement (TSM) and light-scattering measurements of the small TiO_2 particles, and we should not use bulk data to interpret the data measured for nanoparticles. However, the particle size at which the transformation of the particle RIF toward the bulk RIF starts still remains unknown.

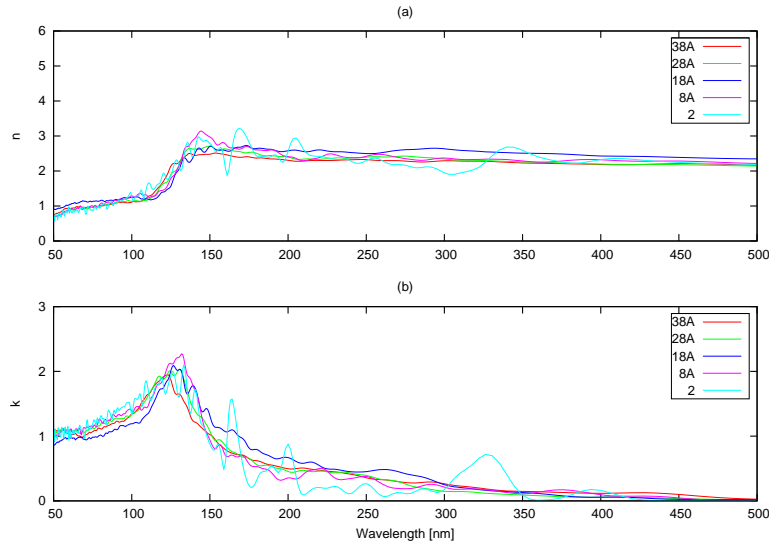


Figure 4.9: The total averaged RIFs for $(\text{TiO}_2)_{nA}$ structures and $(\text{TiO}_2)_2$ structure.

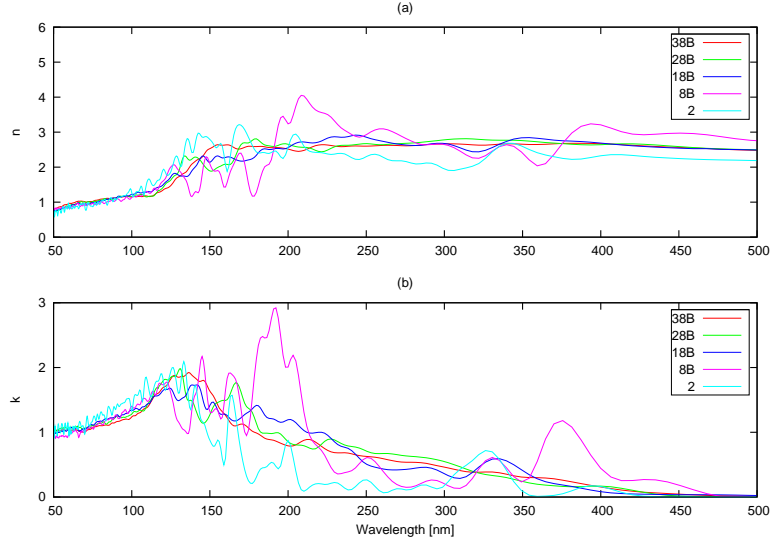


Figure 4.10: The total averaged RIFs for $(\text{TiO}_2)_{nB}$ structures and $(\text{TiO}_2)_2$ structure.

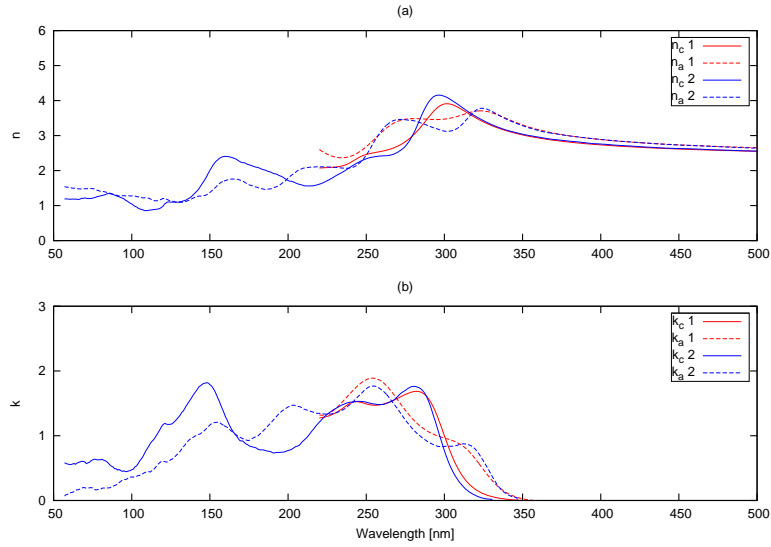


Figure 4.11: The experimental RIF for bulk anatase TiO_2 . The data marked with 1 is from Jellison Jr. *et al.* [65] and the data marked with 2 from Hosaka *et al.* [66]. The subscript a refers to the light polarization along the shorter lattice parameter (x and y in the case of the modeled clusters) and the subscript c to the light polarization along the longer lattice parameter (z in the case of the modeled clusters.)

4.3 Dye-sensitiation of TiO₂ nanoparticles

As a part of my modeling studies, I also participated in partly experimental study of Ni(II) diimine dithiolato complexes as dyes in DSSCs. The results of this study are reported in publication III. For this study four complexes based on [Ni(S₂C₂Ph₂)₂] (**1**) were selected. The selected Ni(II) diimine dithiolato complexes were [Ni(S₂C₂Ph₂) (1,10-Phenanthroline)] (**2**), [Ni(S₂C₂Ph₂)(3,3'-dicarboxy-2,2'-bipyridyl)] (**3**), [Ni(S₂C₂Ph₂)(4,4'-dicarboxy-2,2'-bipyridyl)] (**4**), and [Ni(S₂C₂Ph₂)(2,2'-bipyridyl)] (**5**). The computational study of these complexes was done with Gaussian 09 software. The dye structures were first relaxed, and after the relaxation the structures were used for molecular orbital analyses.

In the experimental studies (which were performed by Abhinav Kumar, Manoj Trivedi, and Ratna Chauhan in India) the electrochemical and electronic absorption characteristics of these dye complexes were measured. More details about the experiments are presented in publication III. The measured electronic absorption spectra and incident photon-to-current efficiency (IPCE) plots for each dye complex are presented in Figures 4.12 and 4.13, respectively. The electronic absorption spectra for the dyes were measured in 2×10^{-5} M dichloromethane solution for dye **1**, and in 2×10^{-3} M solutions for dyes **2-5**. The DFT isosurface plots for the HOMO and LUMO levels of the dyes **1-5** are presented in Figure 4.14.

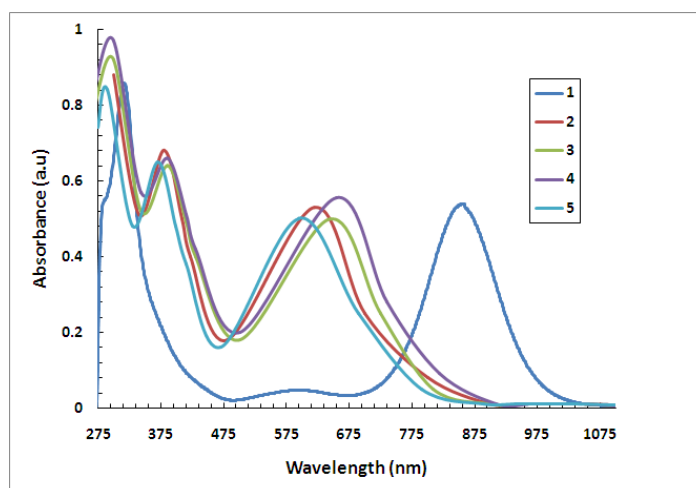


Figure 4.12: The experimental electronic absorption spectra measured for the dyes **1-5**.

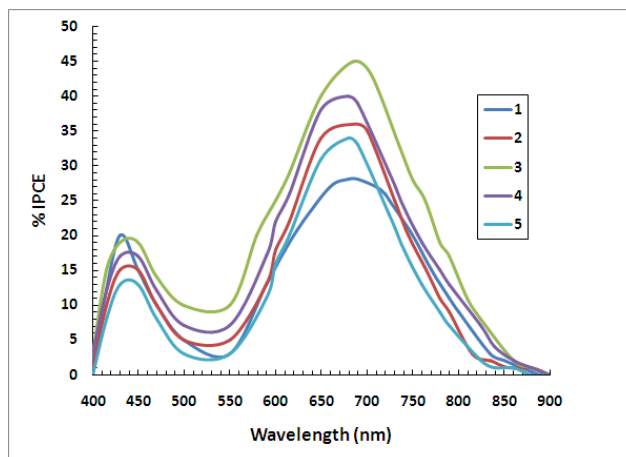


Figure 4.13: The IPCE plot for DSSCs sensitized with the dyes **1-5**.

The electrochemical experiments done by cyclic voltammetry in dichloromethane solution (reported in detail in publication III) indicated that the multiple oxidation for all the four dyes occurs at almost similar potentials. This was considered to be due to the oxidation of the HOMO centered over the dithiolen/dithiolate moiety. Because the dithiolate moiety is identical in all the four diimine derivatives, it was reasonable to expect that the oxidation will take place at similar potentials. Based on the electrochemical experiments, it was also concluded that for all the four diimine derivatives oxidation takes place on the dithiolate ligand and reduction on the diimine derivatives. This means that the charge transfer across the molecules would be directional from dithiolate ligand to diimine derivative. Also the location of HOMO indicated that when the dye is oxidized the positive charge density is placed further from the TiO_2 . The LUMO of all of the four derivatives was found to be at an energy level suitable to allow charge injection into the TiO_2 conduction band.

An interesting finding in the electrochemical experiments was that in the case of dye compound **3**, the first reduction potential was at less negative level when compared to other three derivatives. This was explained by the DFT optimized geometry of the compound **3**, which is presented in Figure S2 in supplementary material for publication III. There is a significant torsion angle (32.16°) between the pyridine rings of the bipyridyl derivative. This can explain the result, because lack in planarity may possibly interfere with the delocalization of the charge between the two pyridine rings. In this case the two pyridine rings behave more like two separate pyridine moieties, and the electrochemical response of the dye compound **3** is influenced by both the electronic and steric effects.

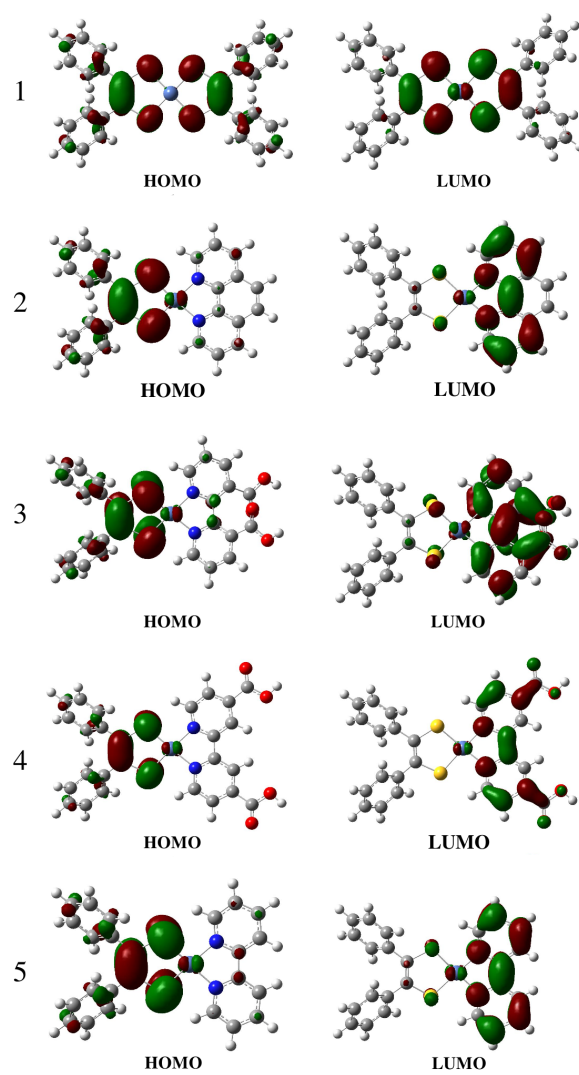


Figure 4.14: The DFT modeled isosurface plots for HOMO and LUMO levels of the dyes 1-5.

The DFT results for HOMO and LUMO densities show that in the cases of heteroleptic diimine dithiolate complexes (**2–5**) the HOMO density is mainly dithiolate ligand based having smaller contribution from the phenyl ring and the Ni(II) center. The LUMO density is almost entirely diimine ligand based. This result is consistent with previously reported results for the HOMO/LUMO positions in diimine dithio nickel(II) complexes [67]. On the other hand, in the case of homoleptic dye **1**, HOMO density is located on both of the dithiolate moieties as well as on the phenyl ring. At the LUMO density level, the density is moved towards the nickel plane. Based on the DFT results it was also concluded that in the case of dyes (**2–5**) the charge transfer is unidirectional. The direction is from dithiolate ligands to phenanthroline/bipyridyl or its derivatives. In the case of dye **1** this phenomenon was not observed. Based on these findings, dye compounds (**2–5**) were seen to be potential candidates for the light harvesting.

The experimentally measured output parameters for DSSCs sensitized with five different dye compounds are presented in Table 4.3. Based on the data in Table 4.3, measured electronic absorption spectra, and IPCE plots (along with some other measurements presented in more detail in publication III) it was concluded that dye **1** has an inferior performance when compared to the rest of its derivatives. This can be due to its symmetrical homoleptic nature. This is also supported by the DFT calculations, indicating the localization of the electron density in the metallic ring plane of the nickel bis(dithiolene) complex which is unfavourable for the electron injection.

Table 4.3: Output parameters of DSSCs sensitized with diimine dithiolate Ni(II) compounds. The parameters are short circuit current (J_{sc}), open circuit voltage (V_{oc}), fill factor (ff), power conversion efficiency (η), and incident photon-to-current efficiency (IPCE).

| Dye compound | J_{sc} [mA/cm ²] | V_{oc} [V] | ff | η [%] | IPCE |
|--------------|--------------------------------|--------------|------|------------|------|
| 1 | 0.328 | 0.402 | 0.49 | 0.06 | 28 |
| 2 | 0.430 | 0.440 | 0.55 | 0.10 | 36 |
| 3 | 0.545 | 0.500 | 0.61 | 0.17 | 40 |
| 4 | 0.519 | 0.460 | 0.57 | 0.14 | 45 |
| 5 | 0.400 | 0.425 | 0.52 | 0.08 | 34 |

The diimine derivatives of dye **1** have better performance, due to the heteroleptic nature of all the four Ni(II) diimine dithiolate dyes. This improves the effective

electron injection and charge separation. Despite this, the efficiencies of dyes **2** and **5** are not promising. The dyes **3** and **4** have **-COOH** functionals at 3,3' and 4,4' positions of the bipyridyl moiety, but they still do not exhibit sufficiently high efficiency. Additionally, in the case of dyes **1**, **2**, and **5** there is lack of chemical bond between the dye and the TiO₂ nanoparticulate [68], which would improve electron injection into the conduction band of the TiO₂.

Chapter 5

Concluding remarks

For this thesis I have been computationally modeling the electronic properties of TiO₂ nanoparticles, along with their absorption properties and RIFs. I have also participated in an experimental study of Ni(II) diimine dithiolato complexes as dyes in DSSCs, by computationally modeling the properties of the dye compounds.

The computational results presented in this thesis and related four publications have revealed that ultrasmall TiO₂ particles show slight evidence on the structure-dependent band gap broadening (about 0.1-0.74 eV). The TDDFT results show that the first allowed excitation can be even 1.32 eV larger than the actual DFT HOMO-LUMO gap. It is also clear that the spectral blue-shifts, blue-shifts in RIFs, and electronic structure in ultrasmall particles are strongly dependent on the shape and structure of the cluster, and in the needlelike structures the longest dimension dominates the absorption characteristics. Due to the small size range of the studied structures, the exact size range, where the transition towards the bulk properties happens was not found.

As already stated, these results are modeled in total vacuum, which is not the case in real-life situations. It can be concluded that there is a need for proper implementation of surrounding chemical environment and intraband excitations to be able to get closer to real-life behavior of the optical properties of nanoparticles. My results also reveal the fact that the optical properties of TiO₂ nanoparticles depend heavily on the structure of the particles, and thus the knowledge on the absolute ground state structures of the TiO₂ nanoparticles has a pronounced role.

Regarding the studies performed on Ni(II) diimine dithiolato complexes as dyes in DSSCs it can be concluded that based on the experimental electrochemical investigation and DFT studies all studied diimine derivatives could serve as potential candidates for the light harvesting. The symmetrical homoleptic complexes are inferior candidates as the dye in DSSCs due to their unfavourable electron injec-

tion properties, while the diimine derivatives have better performances, due to the heteroleptic nature. However, the efficiencies of the dyes studied were not promising.

As a final statement, I want to emphasize that my studies are humble effort to shed some light into this computationally and experimentally very challenging area of nanoparticle properties, and in my studies I have constantly been pushing against the limits of computational power. In the future, when when we are able to use more computational power, and the properties and efficiency of the modeling software are further developed, we should see great enhancement in the accuracy of modeling results for RIFs and other optical properties of TiO_2 nanoparticles.

Bibliography

- [1] S. Mo and W. Y. Ching, “Electronic and optical properties of three phases of titanium dioxide: Rutile, anatase, and brookite,” *Phys. Rev. B*, vol. 51, pp. 13023–13032, 1995.
- [2] D. T. Cromer and K. Herrington, “The structures of anatase and rutile,” *J. Am. Chem. Soc.*, vol. 77, pp. 4708–4709, 1955.
- [3] W. H. Baur, “Über die Verfeinerung der Kristallstrukturbestimmung einiger Vertreter des Rutiltyps. III. Zur Gittertheories des Rutiltyps,” *Acta Cryst.*, vol. 14, pp. 209–213, 1961.
- [4] R. J. H. Clark, *The Chemistry of Titanium and Vanadium: An Introduction to the Chemistry of the Early Transition Elements*. New York: Elsevier Publishing Company, 1 ed., 1968.
- [5] T. A. Kandiel, A. Feldhoff, L. Robben, R. Dillert, and D. W. Bahnemann, “Tailored titanium dioxide nanomaterials: Anatase nanoparticles and brookite nanorods as highly active photocatalysts,” *Chem. Mater.*, vol. 22, pp. 2050–2060, 2010.
- [6] A.-M. Anttila, M. Karppinen, M. Leskelä, H. Mölsä, and M. Pohjakallio, *Tekniikan Kemia*. Helsinki: Edita Publishing Oy, 10–11 ed., 2009.
- [7] M.-L. Kääriäinen, T. O. Kääriäinen, and D. C. Cameron, “Titanium dioxide thin films, their structure and its effect on their photoactivity and photocatalytic properties,” *Thin Solid Films*, vol. 517, p. 6666–6670, 2009.
- [8] H. Zhang and J. F. Banfield, “Thermodynamic analysis of phase stability of nanocrystalline titania,” *J. Mater. Chem.*, vol. 8, pp. 2073–2076, 1998.
- [9] R. L. Penn and J. F. Banfield, “Morphology development and growth in nanocrystalline aggregates under hydrothermal conditions: Insights from titania,” *Geochim. Cosmochim. Acta*, vol. 63, pp. 1549–1557, 1999.
- [10] M. Ramamoorthy, D. Vanderbilt, and R. D. King-Smith, “First-principles calculations of the energetics of stoichiometric TiO_2 surfaces,” *Phys. Rev. B*, vol. 49, pp. 16721–16727, 1994.

- [11] V. Blagojevic, Y.-R. Chen, M. Steigerwald, L. Brus, and R. A. Friesner, "Quantum chemical investigation of cluster models for TiO₂ nanoparticles with water-derived ligand passivation: Studies of excess electron states and implications for charge transport in the Grätzel cell," *J. Phys. Chem. C*, vol. 113, pp. 19806–19811, 2009.
- [12] L. Brus, "Electron-electron and electron-hole interactions in small semiconductor crystallites: The size dependence of the lowest excited electronic state," *J. Chem. Phys.*, vol. 80, pp. 4403–4409, 1984.
- [13] L. Brus, "Electronic wave functions in semiconductor clusters: Experiment and theory," *J. Phys. Chem.*, vol. 90, pp. 2555–2560, 1986.
- [14] L. Brus, "Size dependent development of band structure in semiconductor crystallites," *New J. Chem.*, vol. 11, pp. 123–127, 1987.
- [15] A. J. Nozik, F. Williams, M. T. Nenadović, T. Rajh, and O. I. Mičić, "Size quantization in small semiconductor particles," *J. Phys. Chem.*, vol. 89, pp. 397–399, 1985.
- [16] N. Satoh, T. Nakashima, K. Kamikura, and K. Yamamoto, "Quantum size effect in TiO₂ nanoparticles prepared by finely controlled metal assembly on dendrimer templates," *Nat. Nanotechnol.*, vol. 3, pp. 106–111, 2008.
- [17] Y. Nosaka, "Finite depth spherical well model for excited states of ultrasmall semiconductor particles. An application," *J. Phys. Chem.*, vol. 95, pp. 5054–5058, 1991.
- [18] M. J. Lundqvist, M. Nilsing, P. Persson, and S. Lunell, "DFT study of bare and dye-sensitized TiO₂ clusters and nanocrystals," *Int. J. Quantum Chem.*, vol. 106, pp. 3214–3234, 2006.
- [19] M. Grätzel, *Heterogeneous Photochemical Electron Transfer*. Boca Raton, FL: CRC Press, 1989.
- [20] C. Kormann, D. W. Bahnemann, and M. R. Hoffmann, "Preparation and characterization of quantum-size titanium dioxide," *J. Phys. Chem.*, vol. 92, pp. 5196–5201, 1988.
- [21] M. Anpo, T. Shima, S. Kodama, and Y. Kubokawa, "Photocatalytic hydrogenation of CH₃CCH with H₂O on small-particle TiO₂ - Size quantization effects and reaction intermediates," *J. Phys. Chem.*, vol. 91, pp. 4305–4310, 1987.
- [22] N. Serpone, D. Lawless, and R. Khairutdinov, "Size effects on the photophysical properties of colloidal anatase TiO₂ particles: Size quantization or direct

- transitions in this indirect semiconductor?," *J. Phys. Chem.*, vol. 99, pp. 16646–16654, 1995.
- [23] P. Persson, J. C. M. Gebhardt, and S. Lunell, "The smallest possible nanocrystals of semiionic oxides," *J. Phys. Chem. B*, vol. 107, pp. 3336–3339, 2003.
- [24] A. Hagfeldt, G. Boschloo, L. Sun, L. Kloo, and H. Pettersson, "Dye-sensitized solar cells," *Chem. Rev.*, vol. 110, pp. 6595–6663, 2010.
- [25] M. Grätzel, "Recent advances in sensitized mesoscopic solar cells," *Accounts Chem. Res.*, vol. 42, pp. 1788–1798, 2009.
- [26] S. Ardo and G. J. Meyer, "Photodriven heterogeneous charge transfer with transition-metal compounds anchored to TiO₂ semiconductor surfaces," *Chem. Soc. Rev.*, vol. 38, pp. 115–164, 2009.
- [27] M. Grätzel, "Solar energy conversion by dye-sensitized photovoltaic cells," *Inorg. Chem.*, vol. 44, pp. 6841–6851, 2005.
- [28] M. Grätzel, "Conversion of sunlight to electric power by nanocrystalline dye-sensitized solar cells," *J. Photoch. Photobio. A*, vol. 164, pp. 3–14, 2004.
- [29] B. O'Regan and M. Grätzel, "A low-cost, high-efficiency solar cell based on dye-sensitized colloidal TiO₂ films," *Nature*, vol. 353, pp. 737–740, 1991.
- [30] A. B. F. Martinson, T. W. Hamann, M. J. Pellin, and J. T. Hupp, "New architectures for dye-sensitized solar cells," *Chem. Eur. J.*, vol. 14, pp. 4458–4467, 2008.
- [31] N. R. Neale, N. Kopidakis, J. van de Lagemaat, M. Grätzel, and A. J. Frank, "Effect of a coadsorbent on the performance of dye-sensitized TiO₂ solar cells: Shielding versus band-edge movement," *J. Phys. Chem. B*, vol. 109, pp. 23183–23189, 2005.
- [32] L. H. Thomas, "The calculation of atomic fields," *Proc. Cambridge Phil. Roy. Soc.*, vol. 23, pp. 542–548, 1927.
- [33] E. Fermi, "Un metodo statistico per la determinazione di alcune priorieta dell'atome," *Rend. Accad. Naz. Lincei*, vol. 6, pp. 602–607, 1927.
- [34] P. A. M. Dirac, "Note on exchange phenomena in the Thomas-Fermi atom," *Proc. Cambridge Phil. Roy. Soc.*, vol. 26, pp. 376–385, 1930.
- [35] R. M. Martin, *Electronic Structure: Basic Theory and Practical Methods*. Cambridge: Cambridge University Press, 1 ed., 2004.

- [36] P. Hohenberg and W. Kohn, “Inhomogeneous electron gas,” *Phys. Rev.*, vol. 136, pp. B864–B871, 1964.
- [37] A. Groß, ed., *Theoretical Surface Science: A Microscopic Perspective*. Germany: Springer, 2003.
- [38] J. P. Perdew, M. Ernzerhof, and K. Burke, “Rationale for mixing exact exchange with density functional approximations,” *J. Chem. Phys.*, vol. 105, pp. 9982–9985, 1996.
- [39] C. Adamo and V. Barone, “Toward reliable density functional methods without adjustable parameters: The PBE0 model,” *J. Chem. Phys.*, vol. 105, pp. 6158–6170, 1999.
- [40] J. Heyd, G. E. Scuseria, and M. Ernzerhof, “Hybrid functionals based on screened coulomb potential,” *J. Chem. Phys.*, vol. 118, pp. 8207–8215, 2003.
- [41] J. Heyd, G. E. Scuseria, and M. Ernzerhof, “Erratum: ”hybrid functionals based on screened coulomb potential”,” *J. Chem. Phys.*, vol. 124, pp. 219906–219906, 2006.
- [42] P. J. Stephens, F. J. Devlin, C. F. Chabalowski, and M. J. Frisch, “Ab initio calculation of vibrational absorption and circular dichroism spectra using density functional force fields,” *J. Phys. Chem.*, vol. 98, pp. 11623–11627, 1994.
- [43] M. Jain, J. R. Chelikowsky, and S. G. Louie, “Reliability of hybrid functionals in predicting band gaps,” *Phys. Rev. Lett.*, vol. 107, pp. 216806–1 – 216806–5, 2011.
- [44] E. Runge and E. K. U. Gross, “Density-functional theory for time-dependent systems,” *Phys. Rev. Lett.*, vol. 52, pp. 997 – 1000, 1984.
- [45] P. E. Blöchl, “Projector augmented-wave method,” *Phys. Rev. B*, vol. 50, pp. 17953–17979, 1994.
- [46] P. E. Blöchl, C. J. Först, and J. Schimpl, “Projector augmented wave method: Ab initio molecular dynamics with full wave functions,” *Bull. Mater. Sci.*, vol. 26, pp. 33–41, 2003.
- [47] D. Vanderbilt, “Soft self-consistent pseudopotentials in a generalized eigenvalue formalism,” *Phys. Rev. B*, vol. 41, pp. 7892–7895, 1990.
- [48] J. J. Mortensen, L. B. Hansen, and K. W. Jacobsen, “Real-space grid implementation of the projector augmented wave method,” *Phys. Rev. B*, vol. 71, pp. 035109–1 – 035109–11, 2005.

- [49] J. Enkovaara, C. Rostgaard, J. J. Mortensen, J. Chen, M. Dulak, L. Ferrighi, J. Gavnholt, C. Glinsvad, V. Haikola, H. A. Hansen, H. H. Kristoffersen, M. Kuisma, A. H. Larsen, L. Lehtovaara, M. Ljungberg, O. Lopez-Acevedo, P. G. Moses, J. Ojanen, T. Olsen, V. Petzold, N. A. Romero, J. Stausholm-Møller, M. Strange, G. A. Tritsarlis, M. Vanin, M. Walter, B. Hammer, H. Häkkinen, G. K. H. Madsen, R. M. Nieminen, J. K. Nørskov, M. Puska, T. T. Rantala, J. Schiøtz, K. S. Thygesen, and K. W. Jacobsen, “Electronic structure calculations with GPAW: a real-space implementation of the projector augmented-wave method,” *J. Phys.:Condens. Mat.*, vol. 22, pp. 253202–1 – 253202–24, 2010.
- [50] S. R. Bahn and K. W. Jacobsen, “An object-oriented scripting interface to a legacy electronic structure code,” *Comput. Sci. Eng.*, vol. 4, pp. 56–66, 2002.
- [51] M. Walter, H. Häkkinen, L. Lehtovaara, M. Puska, J. Enkovaara, C. Rostgaard, and J. J. Mortensen, “Time-dependent density-functional theory in the projector augmented-wave method,” *J. Chem. Phys.*, vol. 128, pp. 244101–1 – 244101–10, 2008.
- [52] G. Kresse and J. Hafner, “Ab initio molecular dynamics for liquid metals,” *Phys. Rev. B*, vol. 47, pp. 558–561, 1993.
- [53] G. Kresse and J. Hafner, “Norm-conserving and ultrasoft pseudopotentials for first-row and transition elements,” *J. Phys. Condens. Matter*, vol. 6, pp. 8245–8258, 1994.
- [54] G. Kresse and J. Hafner, “Ab initio molecular-dynamics simulation of the liquid-metal–amorphous-semiconductor transition in germanium,” *Phys. Rev. B*, vol. 49, pp. 14251–14269, 1994.
- [55] G. Kresse and J. Furthmüller, “Efficiency of ab-initio total energy calculations for metals and semiconductors using a plane-wave basis set,” *Comput. Mater. Sci.*, vol. 6, pp. 15–50, 1996.
- [56] G. Kresse and J. Furthmüller, “Efficient iterative schemes for ab initio total-energy calculations using a plane-wave basis set,” *Phys. Rev. B*, vol. 54, pp. 11169–11186, 1996.
- [57] G. Kresse, M. Marsman, and J. Furthmüller, “VASP the guide.” <http://cms.mpi.univie.ac.at/vasp/vasp/vasp.html>, 2013.
- [58] M. J. Frisch, G. W. Trucks, H. B. Schlegel, G. E. Scuseria, M. A. Robb, J. R. Cheeseman, G. Scalmani, V. Barone, B. Mennucci, G. A. Petersson, H. Nakatsuji, M. Caricato, X. Li, H. P. Hratchian, A. F. Izmaylov, J. Bloino, G. Zheng, J. L. Sonnenberg, M. Hada, M. Ehara, K. Toyota, R. Fukuda, J. Hasegawa,

- M. Ishida, T. Nakajima, Y. Honda, O. Kitao, H. Nakai, T. Vreven, J. A. Montgomery, Jr., J. E. Peralta, F. Ogliaro, M. Bearpark, J. J. Heyd, E. Brothers, K. N. Kudin, V. N. Staroverov, R. Kobayashi, J. Normand, K. Raghavachari, A. Rendell, J. C. Burant, S. S. Iyengar, J. Tomasi, M. Cossi, N. Rega, J. M. Millam, M. Klene, J. E. Knox, J. B. Cross, V. Bakken, C. Adamo, J. Jaramillo, R. Gomperts, R. E. Stratmann, O. Yazyev, A. J. Austin, R. Cammi, C. Pomelli, J. W. Ochterski, R. L. Martin, K. Morokuma, V. G. Zakrzewski, G. A. Voth, P. Salvador, J. J. Dannenberg, S. Dapprich, A. D. Daniels, O. Farkas, J. B. Foresman, J. V. Ortiz, J. Cioslowski, and D. J. Fox, "Gaussian 09 Revision C.01." Gaussian Inc. Wallingford CT 2009.
- [59] "The official Gaussian website." http://www.gaussian.com/g_prod/g09b.htm, 2013.
- [60] T. Albaret, F. Finocchi, and C. Noguera, "Ab initio simulation of titanium dioxide clusters," *Appl. Surf. Sci.*, vol. 144, pp. 672–676, 1999.
- [61] Z.-W. Qu and G.-J. Kroes, "Theoretical study of the electronic structure and stability of titanium dioxide clusters $(\text{TiO}_2)_n$ with $n = 1-9$," *J. Phys. Chem. B*, vol. 110, pp. 8998–9007, 2006.
- [62] L. Tang, L. Sai, J. Zhao, and R. Qiu, "A topological method for global optimization of clusters: Application to $(\text{TiO}_2)_n$ ($n=1-6$)," *J. Comput. Chem.*, vol. 33, pp. 63–169, 2012.
- [63] R. Smoluchowski, "Anisotropy of the electronic work function of metals," *Phys. Rev.*, vol. 60, pp. 661 – 674, 1941.
- [64] N. S. McIntyre, K. R. Thompson, and W. Weltner, "Spectroscopy of titanium oxide and titanium dioxide molecules in inert matrices at 4.deg.k," *J. Phys. Chem.*, vol. 75, pp. 3243–3249, 1971.
- [65] G. E. Jellison, L. A. Boatner, J. D. Budai, B.-S. Jeong, and D. P. Norton, "Spectroscopic ellipsometry of thin film and bulk anatase (TiO_2) ," *J. Appl. Phys.*, vol. 93, pp. 9537–9541, 2003.
- [66] N. Hosaka, T. Sekiya, C. Satoko, and S. Kurita, "Optical properties of single-crystal anatase TiO_2 ," *J. Phys. Soc. Jpn.*, vol. 66, pp. 877–880, 1997.
- [67] C. L. Linfoot, P. Richardson, K. L. McCall, J. R. Durrant, A. Morandeira, and N. Robertson, "A nickel-complex sensitiser for dye-sensitised solar cells," *Sol. Energy*, vol. 85, pp. 1195–1203, 2011.
- [68] T. Ma, K. Inoue, H. Noma, K. Yao, and E. Abe, "Effect of functional group on photochemical properties and photosensitization of TiO_2 electrode sensitized by

porphyrin derivatives," *J. Photochem. Photobiol. A: Chem.*, vol. 152, pp. 207–212, 2002.

Publication I

S. Auvinen, M. Alatalo, H. Haario, J.P. Jalava, R.J. Lamminmäki,
“Size and Shape Dependence of the Electronic and Spectral Properties in TiO₂
Nanoparticles”

Reprinted from The Journal of Physical Chemistry C 115, 8484-8493 ©(2011),
with permission from American Chemical Society.

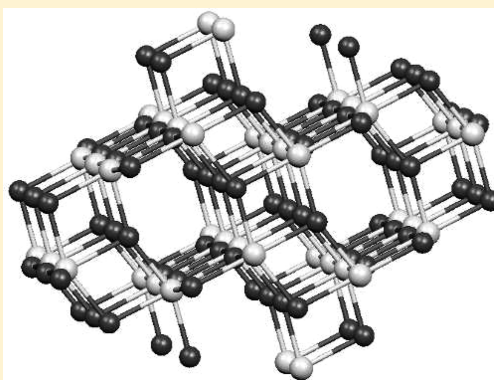
Size and Shape Dependence of the Electronic and Spectral Properties in TiO₂ Nanoparticles

Sami Auvinen,^{*,†} Matti Alatalo,[†] Heikki Haario,[†] Juho-Pertti Jalava,[‡] and Ralf-Johan Lamminmäki[‡]

[†]Faculty of Technology, Department of Mathematics and Physics, Lappeenranta University of Technology, P.O. Box 20, FI-53851 Lappeenranta, Finland

[‡]Sachtleben Pigments Oy, Pori, Finland

ABSTRACT: Electronic and spectral properties of small TiO₂ particles have been studied in order to gain more knowledge on their dependence on the crystal- and particle-size distributions. Our goal is to extend the recently developed light scattering based method for determining submicrometer size particles to nanoparticles. For that, we need to know how the refractive index function depends on the cluster size. As a first step, we have used time-dependent density functional theory (TDDFT) calculations having a focus on the shape changes of the calculated spectra, which can be related to changes in the refractive index function. Starting from the structure of TiO₂ molecule for the two smallest particles and truncated bulk anatase structure for larger particles, the structures for (TiO₂)_n clusters, $n = \{1, 2, 8, 18, 28, 38\}$, have been modeled. After the structure optimization using standard density functional theory (DFT) approach, the photoabsorption spectra for the optimized particle structures have been calculated by using TDDFT calculations. The results show slight evidence of the band gap broadening in the case of three out of the smallest particles and strong structural dependence of electronic and spectral properties, which can partly be related to the transformation of the electron structure, and breaking of the crystal symmetry as the size of the particle becomes smaller. These findings indicate that in the case of small particles their refractive index function can differ from the bulk values, and this has to be taken into account in the interpretation of light-scattering measurements.



INTRODUCTION

The most commonly used titanium dioxide pigment particles of the size ca. 200 nm are widely used, for example, in paints, printing inks, plastics, and papers, because of the excellent opacity and whiteness they provide.¹ Many other interesting applications become possible by decreasing the particle size from 200 nm to nanosize material down to 10 nm or even below. This decrease changes the optical properties of TiO₂ remarkably from opaque to transparent in the visible range of the light spectrum and to an excellent UV-light blocker. These kinds of nanomaterials are widely used in many applications where visible light transparency and UV shield is required such as sunscreens, wood lacquers, plastics, cosmetics, foods,^{2,3} and photoelectronics.^{4,5}

It is of most importance in manufacturing different products to finely control these wide range optical properties. Because of their dependence on the pigment's crystal- and particle-size distributions (CSD, PSD), the process and quality control of the CSD and PSD are essential. The development of a straightforward and sophisticated method for process and quality control for the most used or "normal" size (particle diameter ca. 200 nm) pigment products was presented several years ago.¹ The principal

component of the method is a relatively new determination method for the PSD on the basis of an accurate theory of light scattering of spheroidal particles.⁶ In this method, called the turbidity spectrum method (TSM), the turbidity spectrum is measured in a wide range of wavelengths. This spectrum, which is due to the particle-size distribution of the pigment particles, is then solved using the T-matrix method by taking into account the shape of the particles. The T-matrix method is one of the most powerful and widely used tools for the rigorous computing of electromagnetic scattering by nonspherical particles.^{7,8} TSM is now used as a process control method and is optimized for the normal pigment size having an excellent repeatability for the mean PSD with one standard deviation being 0.1 nm (0.05%). The measuring of pigment particles smaller than the normal size pigments, for example, UV-TITAN pigment particles, has gained more importance during the years. Therefore, the introduction of TSM also for nanosize materials is essential. Computing the

Received: December 21, 2010

Revised: February 28, 2011

Published: April 08, 2011

particle size by exact light scattering methods such as Mie scattering for spheres or TSM for elongated particles like most of the titanium dioxide pigments needs the complex refractive index function of the measured crystal material for all wavelengths used in the measurement. Normally, only refractive index function of the bulk material is needed. However, there are studies indicating that the surface or the finite size of a very small particle can have an effect on the refractive index function especially in the UV wavelengths.⁹ The TSM results are in accordance with these findings, and therefore, it is important to clarify this phenomenon.

Titanium dioxide is a semiconducting metal oxide that has a relatively large band gap of 3.23 eV for the anatase phase and 3.0 eV for the rutile phase.¹⁰ These two are commercially the most interesting ones of its polymorphs. The third possible structure, brookite, has also attracted interest recently as a promising photocatalyst in a nanocrystalline form.¹¹ Previous optical and electronic studies on titanium dioxide using both experimental and computational methods include studies on properties of the pure^{12–15} and doped bulk structures.¹⁶ These and many other studies have revealed the band structure and reflection and absorption properties for bulk titanium dioxide, but not much computational data can be found for spectral properties of very small TiO₂ particles.

In previous particle studies, it has already been shown that moderate and small semiconductor particles can have different absorption properties. The phenomenon is commonly known as the quantum-size effect or size quantization^{17–20} and was originally explained in 1984 by Brus, who linked the observed spectral blue-shifts of this phenomenon with confinement of the electron wave functions.¹⁷ This means that the effective band gap broadening is observed when the size of the semiconductor particle becomes smaller than the exciton radius thus making the hole and electron form a confined bound state. Brus's model predicted that with large band gap materials, such as CdS, the effect is visible with crystal sizes smaller than about 60 Å, whereas with small band gap materials, such as GaAs, the effect is already visible with relatively large crystal sizes.¹⁷ The original Brus model¹⁸ is known to fail in some cases for ultrasmall particles and, for example, in 2008, Satoh et al.²¹ used an equation derived from a Nosaka equation,²² which improved the formulation of the Brus model using a finite depth potential well. Besides the blue-shifts caused by discretized levels in valence and conduction band edges appearing as a larger effective band gap, in the small semiconductor particles, we can also expect the excitonic peaks to appear in the spectrum.²⁰

There is, however, a discrepancy between the observations and the theoretical explanations of this phenomenon in the case of titanium dioxide. The band gap broadening and quantum size effect have been usually connected with small semiconductor particles because of the suggested origin of the phenomenon. For TiO₂, the calculated size of the particle, below which we should see the quantum size effect, varies with the reduced effective mass of the charge carriers used in the calculation.²³ Typically, this predicted threshold diameter of the particle varies from 0.6 to 3.8 nm (refs 3 and 18 in an article by Serpone et al.²³) depending on the mass used. Recently, it was computationally verified for titanium dioxide that quantum size effect causes a significant band gap broadening when the size of the particle is reduced from 2 to 1 nm after which the further widening of the gap is limited by surface defect sites.²⁴ However, in 1987, Anpo et al. reported that in their experiments for the anatase particles in the range of

3.8–53 nm, and for the rutile particles in the range of 5.5–200 nm, the quantum size effects could still be seen at such high particle sizes.²⁵ On the other hand, in 1995, Serpone et al. reported that in their experiments they did not see any evidence of the quantum size effect at all with the TiO₂ particles studied having mean diameters of 2.1, 13.3, and 26.7 nm.²³ They also explained the earlier observations of blue-shifts with direct transitions in anatase which is an indirect semiconductor.²³ Also, in 2000, Monticone et al. reported experiments that found almost no variation of the TiO₂ band gap energy with sizes down to 1.5 nm, but they did find indications of significant effect of the size on the electronic band structure.²⁶ In 2008, Satoh et al. reported experiments showing quantum size effect in TiO₂ particle samples of anatase and rutile.²¹ In their experiments, Satoh et al. used fourth-generation phenylazomethine dendrimers as templates to make TiO₂ particle samples. The complexation in fourth-generation phenylazomethine dendrimers proceeds in a radially stepwise manner thus leading to very narrow size distribution in particle samples increasing the accuracy of the measurements.²¹

In this paper, we study the electronic and spectral properties of the very small TiO₂ particles using the newest time-dependent density functional theory (TDDFT) methods. The point in choosing the shape and structure of the particles for modeling was that they should simulate those forms which can be found during the manufacturing the particles. All the manufacturing methods in use are based on the hydrolysis of titanium dioxide from different kinds of acidic solutions or slurries. In many cases, also the calcination of the precipitated products will follow the hydrolysis. The basic event in hydrolysis is that the individual TiO²⁺ or Ti(OH)₂²⁺ ions, or their more hydrated products present in solutions, tend to polymerize via olation and oxolation to (TiO₂)_n-chains.^{27,28} The chains then tend to join together and grow first to small particles of several nanometers and then to bigger particles by aggregation. Depending on the composition of the solution and the temperature of hydrolysis, the structure of the forming particles can be anatase or rutile and their shape can be spherical or elongated or even needlelike.²⁹ Because the used software does not include the option to calculate the refractive index function directly, we have not yet calculated the refractive index function for the clusters modeled here. Instead, we concentrate on the effects of the particle size and shape on the photoabsorption spectra of the clusters.

We started by a brief background introduction, and the rest of the paper is organized as follows: In the next section, we present an overview of the software used and go through the computational details used in the modeling. In the Results and Discussion section, we go through the results in detail for structure optimization and photoabsorption spectra. Finally, in the last section, we provide some conclusions and future directions.

COMPUTATIONAL DETAILS

All calculations in this study have been performed by using the GPAW software,^{30–32} which is an efficient density functional theory (DFT) based code using projector-augmented wave (PAW) method.^{33,34} GPAW has a TDDFT implementation,³⁵ which can be used to model excited electron states needed in spectral analysis of the nanoparticles, and the possibility to use nonperiodic systems makes the code suitable for our needs.

As a first step in our calculations, the constructed model structures for the clusters were allowed to relax. This was done by

using a quasi-Newton minimizer and setting the accuracy requirement so that in final structures all forces are smaller than 0.05 eV/Å. In final relaxation runs, the width of the Fermi distribution was set to 0 eV giving us zero Kelvin electronic temperature and integer occupation numbers. The grid spacing was set to 0.17 Å, and the cell was set up with nonperiodic boundary conditions so that there was 7 Å of empty space surrounding the cluster in every coordinate direction. We used the Perdew, Burke, Ernzerhof (PBE) exchange correlation function³⁶ and conjugate gradient method for eigensolver, and all calculations were spin-paired using only the Γ -point. Some of the clusters were tested also with spin-polarized calculations but showed no sign of total polarization. The structures for bulk anatase and rutile were relaxed by using the width of the Fermi distribution of 0.05 eV and k -point sets of $8 \times 8 \times 6$ for anatase and $6 \times 6 \times 10$ for rutile.

To see the effect of the cluster size on the band structure, we calculated the density of states (DOS) for the clusters and bulk structures. In these calculations for the converged structures, we used the same computational settings as we did with structural optimization runs, but in addition, the empty states were also required to be fully converged. The actual DOS was acquired with 2000 data points and a normalized Gaussian broadening of 0.05 eV.

When calculating the photoabsorption spectra, we used the TP-TDDFT approach. With this method, we tested the calculation parameters for the $(\text{TiO}_2)_4$ cluster and molecule to find out sufficient values. The spectra for molecule and $(\text{TiO}_2)_2$ cluster were calculated using an 8.0 attosecond time step with 2000 iterations yielding a total simulation time of 16 fs. The grid-spacing was set to 0.2 Å. The spectra for $n = 8-38$ structures were calculated by using a time step of 16.0 attosecond with 1000 iterations and grid-spacing of 0.3 Å resulting in a significant reduction of the computational load while maintaining the accuracy. The kick parameter for initial disturbance of the wave functions was set to 10^{-3} . The calculation cell was set up again with nonperiodic boundary conditions so that there was 10 Å of empty space in every coordinate direction surrounding the cluster. All the parameters used were tested, and they give well-converged eigenvalues for bands in the adsorption region. The spectra were calculated from the dipole moment files by using a Gaussian broadening of 0.1 eV.

RESULTS AND DISCUSSION

Structure Optimization. The cluster models for $(\text{TiO}_2)_n$ clusters $n = \{1-38\}$ were constructed on the basis of empirical values for anatase and TiO_2 molecule. The two smallest ones, $n = \{1, 2\}$, are obvious structures because the structure of the molecule is known and the other is a combination of two molecules. As a starting point, we used experimental and computational data for TiO_2 molecule giving us the Ti–O bond length of ~ 1.62 Å and the O–Ti–O angle of $\sim 110^\circ$ for the molecule.^{37,38}

The calculated $n = 8$ structure is already a piece of truncated anatase bulk, and the $n = \{18, 28, 38\}$ clusters were also constructed from the truncated bulk structure. As a starting point, we used the anatase structure with 12 atoms per unit cell having lattice constants $a = 3.784$ and $c = 9.515$ Å.³⁹ In general, the rutile structure is the most thermodynamically stable TiO_2 structure, but at very small particle dimensions, the formation of the three TiO_2 phases depend on size, pH, temperature, and

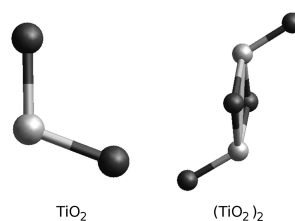


Figure 1. The quasi-Newton optimized structures for TiO_2 molecule and $(\text{TiO}_2)_2$ cluster. Titanium atoms are marked as gray, and oxygen atoms are marked as black.

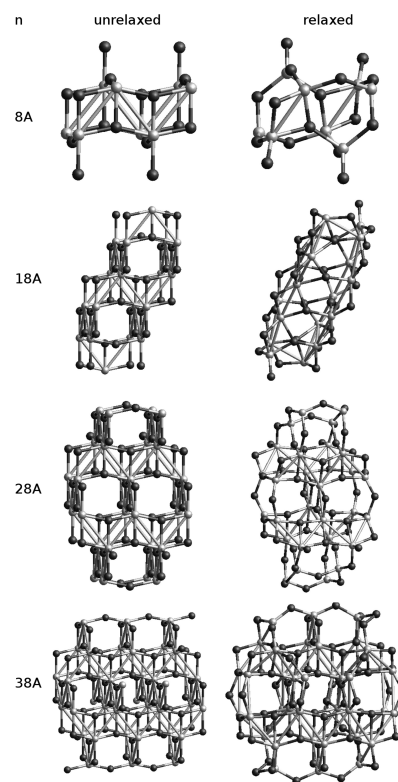


Figure 2. The original unrelaxed A-structures for $(\text{TiO}_2)_n$ clusters, $n = 8, 18, 28, 38$, and the quasi-Newton optimized structures in corresponding order. Titanium atoms are marked as gray, and oxygen atoms are marked as black.

medium.^{29,40–43} The previous studies have shown that in normal conditions the anatase structure is the most stable polymorph in the smallest particles.^{41–43} This is why we have neglected rutile and brookite in this study and have used only anatase structures as a starting point. To study the shape dependence of the properties, we used two different types of structures. The A-structures for $n = 8, 18, 28$, and 38 clusters were carved from

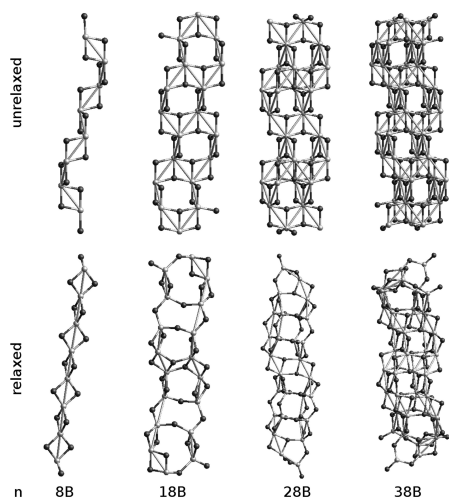


Figure 3. The original unrelaxed B-structures for $(\text{TiO}_2)_n$ clusters, $n = 8, 18, 28, 38$, and the quasi-Newton optimized structures in corresponding order. Titanium atoms are marked as gray, and oxygen atoms are marked as black.

the bulk so that they would be as symmetric as possible in every direction still possessing as much bulklike structure as possible. On the other hand, the corresponding B-structures were carved from the anatase bulk so that they would be longer in z coordinate direction, and the structure would be needlelike. The forms of A and B-structures are depicted in Figures 2 and 3.

As a result of the structure optimization, the structures behaved differently according to their size, and the smallest structures $n = \{1, 2\}$ changed only slightly. The optimized structures for molecule and $(\text{TiO}_2)_2$ cluster are presented in Figure 1. The unrelaxed A-structures along with optimized ones for $n = \{8-38\}$ clusters are presented in Figure 2, and the corresponding B-structures are shown in Figure 3. In all cases, the more symmetrical A-structures were energetically more favorable when compared to corresponding B-structures.

The relaxed structures have slight distortions from ideal anatase crystal structure. This means that the strict ordering of bulk structure disappeared in some sense but that the form of two connected molecules, which is a base of the anatase structure, can still be found in these structures in a slightly distorted form as we can see from Figures 2 and 3. For comparison, we also tried to relax rutile-structured $n = 28$ and $n = 38$ clusters, but in these two cases, the structure optimization ended up with having no recognizable crystal structure, which was exactly the result we expected in this case. The rutile-structured clusters were also energetically unfavored when compared to ones with anatase structure.

The relaxed TiO_2 molecule had the Ti–O bonding length of 1.706 Å and the O–Ti–O angle of 111.734 degrees. These values are in reasonable agreement with experimental values because larger values can be expected when working with GGA approach. Also, the grid density can introduce small unphysical forces in the structures, and this should always be remembered when working on structure optimizations with grid-based codes.

Table 1. Average Bonding Lengths in Relaxed Structures^a

| structure | $d_{\text{Ti-O}}$ [Å] | $d_{\text{Ti-Ti}}$ [Å] | $d_{\text{O-O}}$ [Å] |
|------------------------|-----------------------|------------------------|----------------------|
| molecule | 1.71 | | |
| $(\text{TiO}_2)_2$ | 1.83 | 2.77 | |
| $(\text{TiO}_2)_{8A}$ | 1.89 | 2.85 | |
| $(\text{TiO}_2)_{8B}$ | 1.88 | 2.77 | |
| $(\text{TiO}_2)_{18A}$ | 1.91 | 2.83 | |
| $(\text{TiO}_2)_{18B}$ | 1.89 | 2.76 | |
| $(\text{TiO}_2)_{28A}$ | 1.88 | 2.82 | |
| $(\text{TiO}_2)_{28B}$ | 1.89 | 2.83 | |
| $(\text{TiO}_2)_{38A}$ | 1.90 | 2.83 | 1.46 |
| $(\text{TiO}_2)_{38B}$ | 1.93 | 2.87 | |
| anatase | 2.01 | | |
| rutile | 2.02 | | |

^a The values for anatase and rutile are for bulk structure.

In this case, the reasonably small grid spacing ($h = 0.17$) should reduce the effect of these grid-born forces.

The average bonding lengths for all structures are presented in Table 1. By looking at the results in Table 1, one can see that the average Ti–O bonding length in the clusters is smaller than in the bulk. This indicates that the clusters have more compact crystal structure because of increased surface-to-bulk ratio. Also, the optimized structures distort from clear anatase crystal structure to some kind of semicrystal form not having a molecular structure anymore but still lacking the strict and clear periodicity of the anatase crystal. This is due to still quite small cluster size (the maximum diameter is about 2.66 nm for $(\text{TiO}_2)_{38B}$) and to the forming of the surface structure in the small particles. The results in Table 1 show that the average Ti–O bonding length grows as a function of particle size (when we take the changes between A and B structures into consideration) and will eventually achieve the bulk value at quite small particle diameter.

In the original unrelaxed structures, there were no O–O bonds, and the number of terminal Ti–O bonds were kept as small as possible, so that the unrelaxed clusters had only two to six terminal Ti–O bonds. After the quasi-Newton optimization, the final structures have usually only two terminal Ti–O bonds. In the case of $(\text{TiO}_2)_{38A}$ there are no terminal Ti–O bonds, but the final structure has two O–O bonds. In the analysis of the bonds in the relaxed structures, we simply assumed that there is a Ti–O bond if the bonding distance is smaller than 2.15 Å, a Ti–Ti bond if the bonding distance is smaller than 2.90 Å, and an O–O bond if the bonding distance is smaller than 1.47 Å.

Electronic Structures. The DOS for the optimized structures show the formation of the band structure. In Figure 4, we compare the DOS for $(\text{TiO}_2)_2$ and $(\text{TiO}_2)_{nA}$ structures, and in Figure 5, we compare the DOS for $(\text{TiO}_2)_2$ and $(\text{TiO}_2)_{nB}$ structures. For comparison, the DOS for bulk anatase and rutile are presented in Figure 6. The energy is relative to the vacuum level in the case of clusters and to the Fermi level in the case of bulk structures. The band gaps depicted in the DOS figures are also listed in Table 2. The DFT gaps for clusters, shown as dotted vertical lines in Figures 4 and 5, are the actual highest occupied molecular orbital–lowest unoccupied molecular orbital (HOMO–LUMO) gaps taken out from the GPAW, but the DFT gaps for anatase and rutile were estimated by a distance between the density peaks in the gap edges. This estimation gave

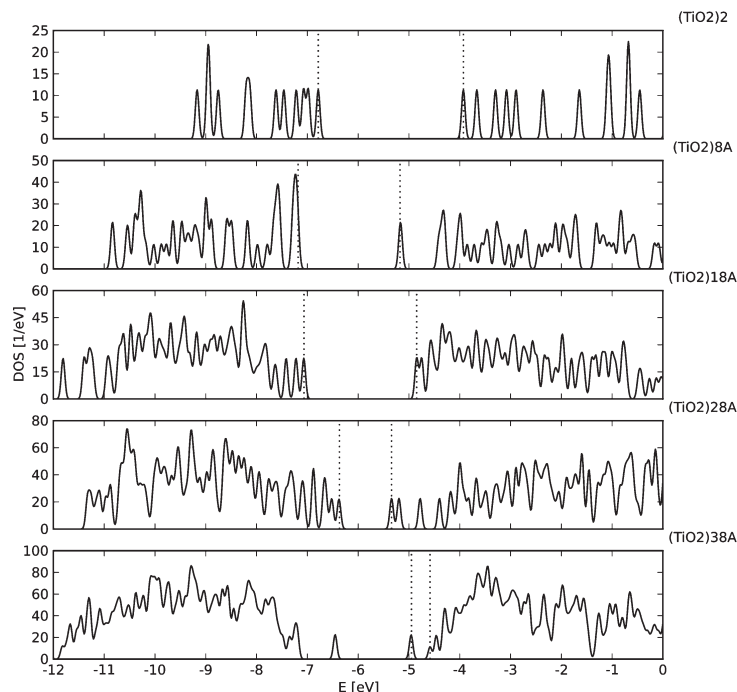


Figure 4. DOS for $(\text{TiO}_2)_2$ and $(\text{TiO}_2)_{nA}$ clusters, $n = 8, 18, 28, 38$. The x -axis represents the energy, and the y -axis is the total DOS. The energy is relative to the vacuum level. The gap edges have been plotted with dotted lines.

gaps of 2.12 eV for anatase and 1.75 eV for rutile. When we remember that GGA-DFT approach tends to underestimate the gap, these DFT estimations have quite good correspondence to the experimental values, anatase structure having a 0.37 eV larger gap than rutile, and also excellent correspondence to the previous DFT results. Previously, for example, Mo and Ching reported computational result for TiO_2 band structures. They found band gaps of 2.04, 1.78, and 2.20 eV for anatase, rutile, and brookite, respectively.¹² Their results also show that DOS for all three bulk phases are quite similar with each other.¹²

When we look at the DOS figures, it is clear that $(\text{TiO}_2)_{38A}$ already has more bulklike band structure with continuous valence and conduction bands, whereas $(\text{TiO}_2)_2$ has clearly more localized states in valence and conduction bands. The normalized Gaussian broadening of 0.05 eV has been used in the plotting of the DOS. We can also see a slight change in the width of the band gap as the $(\text{TiO}_2)_2$ structure has a 0.74 eV larger gap when compared to bulk anatase structure. Also, $(\text{TiO}_2)_{8B}$ and $(\text{TiO}_2)_{18A}$ structures have 0.67 and 0.1 eV larger gaps than bulk anatase. These results correspond well to the previously reported blue-shifts of 0.1–0.6 eV.²¹ These observations indicate structure-dependent gap broadening, because in these ground state based DFT calculations, we do not see any excitonic quantum-size effects.

It is interesting that besides the three above-mentioned structures, the other modeled clusters have smaller gaps than bulk anatase crystal should have. What is especially interesting in the DOS results is that the DFT gap of the $(\text{TiO}_2)_{38A}$ structure is

only 0.37 eV, and also the $(\text{TiO}_2)_{28A}$ structure has a suspiciously small gap of 1.03 eV. When we look at the DOS figures of $(\text{TiO}_2)_{28A}$ and $(\text{TiO}_2)_{38A}$ more carefully, we see that especially with $(\text{TiO}_2)_{38A}$ the actual gap should be larger, but it seems that there are localized states in the gap area. Previously, Lundqvist et al. reported defect-free fundamental band gaps for $(\text{TiO}_2)_{28}$ and $(\text{TiO}_2)_{38}$ structures.²⁴

These two extra small gaps in our case could be explained by defect states and structural changes. In the case of $(\text{TiO}_2)_{38A}$ structure, the small gap could be partly due to two O–O bonds present in final relaxed structure. In the case of $(\text{TiO}_2)_{28A}$, there is no clearly visible reason for the extra small gap, but along with terminal Ti–O bonds, the bond length analysis discussed in the previous section revealed that both $(\text{TiO}_2)_{28A}$ and $(\text{TiO}_2)_{38A}$ include more 7-fold coordinated titanium atoms and 3-fold coordinated oxygen atoms than the other structures. Previously, Persson et al. published an article about a computational study on TiO_2 nanocrystals with semiionic bonding.⁴⁴ The results of Persson et al. show that if the TiO_2 clusters simultaneously fulfill strict criteria of stoichiometry, high coordination, and balanced charge distribution, they exhibit systematic and strong quantum-size effects.⁴⁴ On the other hand, if the TiO_2 nanocrystals do not strictly fulfill all the necessary criteria, the quantum-size effects are not clearly visible anymore, and these nanocrystals can even have gaps that are smaller than the bulk values.⁴⁴ Our current results agree perfectly with their findings. Closer inspection of the $(\text{TiO}_2)_{28}$ and $(\text{TiO}_2)_{38}$ structures used by Lundqvist et al.²⁴ shows that they used more flat structures when compared to the

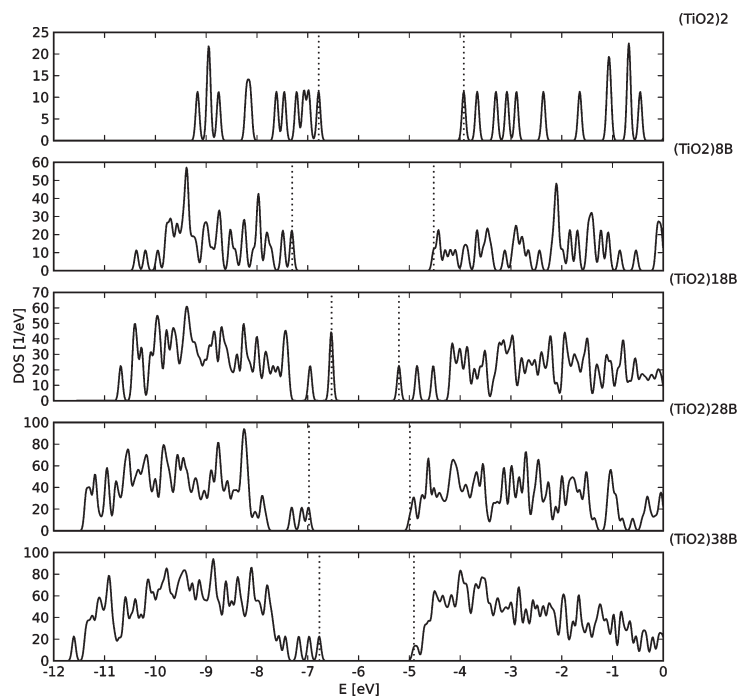


Figure 5. DOS for $(\text{TiO}_2)_2$ and $(\text{TiO}_2)_{nB}$ clusters, $n = 8, 18, 28, 38$. The x -axis represents the energy, and the y -axis is the total DOS. The energy is relative to the vacuum level. The gap edges have been plotted with dotted lines.

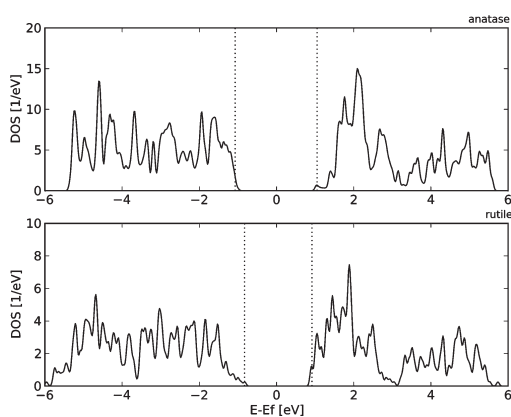


Figure 6. DOS for bulk anatase TiO_2 and for bulk rutile TiO_2 . The x -axis represents the energy, and the y -axis is the total DOS. The energy is relative to the Fermi level. The gap edges have been plotted with dotted lines.

ones we used in this study and also that the used structures seem to be constructed with minimal or even nonexistent number of terminal Ti–O bonds. Lundqvist et al. also reported increasing surface defect sites to limit the gap broadening when particles are

Table 2. DFT HOMO–LUMO Gaps for Cluster and Bulk Structures

| structure | HL gap [eV] |
|------------------------|-------------------|
| $(\text{TiO}_2)_2$ | 2.86 |
| $(\text{TiO}_2)_{8A}$ | 2.01 |
| $(\text{TiO}_2)_{8B}$ | 2.79 |
| $(\text{TiO}_2)_{18A}$ | 2.22 |
| $(\text{TiO}_2)_{18B}$ | 1.33 |
| $(\text{TiO}_2)_{28A}$ | 1.03 |
| $(\text{TiO}_2)_{28B}$ | 1.99 |
| $(\text{TiO}_2)_{38A}$ | 0.37 |
| $(\text{TiO}_2)_{38B}$ | 1.86 |
| anatase | 2.12 ^a |
| rutile | 1.75 ^a |

^a Estimation from density peaks in DOS plot.

smaller than 1 nm in diameter and that the achieved structural reconstructions in the modeling are sensitive to the quality of the computational method used in the relaxation.²⁴ This is because several structural isomers with different bonding arrangements are very close in energy for really small titanium dioxide particles.²⁴

There is also a possibility that the choice of the cluster surfaces, made in the selection of cutting direction when cleaving the cluster model from the bulk structure, could also affect the

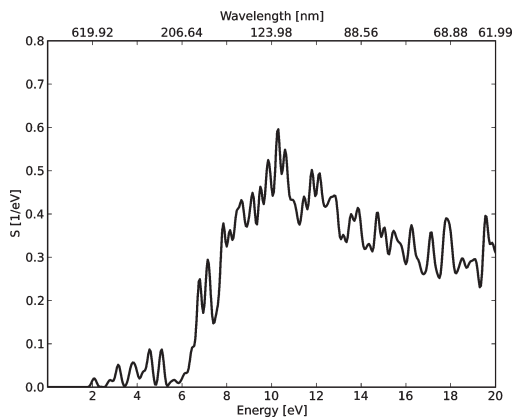


Figure 7. Photoabsorption spectrum for TiO_2 molecule. The x -axis represents the excitation energy and the corresponding wavelength. The y -axis represents the absorption spectrum.

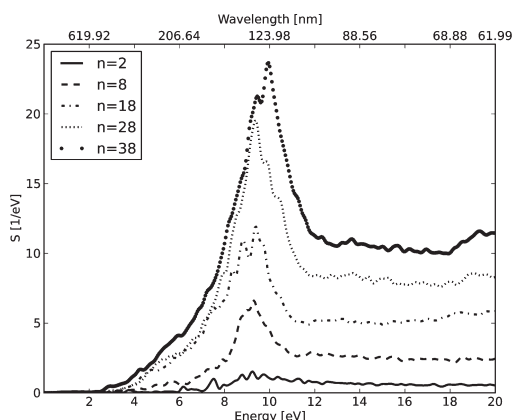


Figure 8. Photoabsorption spectrum for $(\text{TiO}_2)_2$ and $(\text{TiO}_2)_{nA}$ ($n = 8, 18, 28, 38$) clusters. The x -axis represents the excitation energy and the corresponding wavelength. The y -axis represents the absorption spectrum.

electronic structure and the gap of the cluster. Although we present here some ideas about the source of the extra small band gap in $(\text{TiO}_2)_{28A}$ and $(\text{TiO}_2)_{38A}$ structures, the reader should be aware that on the basis of only two structures, we cannot make any final statements. It is clear, however, that the electronic structure and the gap width are very sensitive to the changes in the coordination of the atoms, the structure of the cluster, and the shape of the cluster and not only to the size and the amount of (TiO_2) units. This is very clearly seen when we compare the DOS plots for A- and B-structures.

Photoabsorption Spectra. The calculated photoabsorption spectrum for the TiO_2 molecule is presented in Figure 7, and the photoabsorption spectra for $(\text{TiO}_2)_2$ and A-structured clusters is shown in Figure 8. As we can see, the spectra also show clear evidence of the transition from molecular-like electron structure,

where valence and conduction bands are quite narrow with almost atomic orbitals, toward the bulklike electron structure with wide band structure. This is clear when we compare the quite spiky spectrum for the molecule with all the rest of the spectra. We see that as the cluster size becomes larger the absorption spectrum becomes more continuous.

When we look at Figure 8, we see that the bigger shoulder of the absorption for the largest cluster starts in the region of 3.2 eV. Closer inspection of the first visible excitations shows that the TDDFT absorption thresholds correspond well with band gaps achieved with standard DFT calculation, although the TDDFT gaps are systematically larger than DFT gaps. The DFT HOMO–LUMO gaps, the TDDFT absorption thresholds, and the corresponding wavelengths and cluster sizes are shown in Table 3. The DFT gaps in Table 2 and the absorption thresholds in Table 3 indicate that the first allowed excitation can be even 1.32 eV bigger than the actual HOMO–LUMO gap depending on the cluster structure. We also already stated that there is an absorption blue-shift of 0.74 eV between the smallest cluster and the anatase bulk on the basis of the HOMO–LUMO gaps.

By looking at the shapes of the spectra in the scale of Figure 8, it might appear that the front edge of the spectrum shifts higher and toward the lower excitation energies as a function of the cluster size. This conclusion is, however, incorrect. If we scale the spectra so that they all have the same maximum value (1.0), we see that in the case of A-structures the basic shape of the absorption spectra stays quite constant as we can see in Figure 9 where three example spectra are plotted. This indicates that the basic absorption characteristics do not change when the particle size is growing in the case of symmetric ultrasmall TiO_2 particles. We also already stated that the absorption gets more localized in smaller excitation energies as the size of the cluster decreases, which is clearly visible also in Figure 9. If we compare the scaled spectra for A-structures with ones for B-structures, presented in Figure 10, we see that shape of the cluster can have a strong effect on the absorption spectra of the cluster. This is particularly clear in the case of $(\text{TiO}_2)_{8B}$, which has a strongly red-shifted spectrum when compared with the spectrum of $(\text{TiO}_2)_{38B}$.

When we consider the total absorption spectra, the more localized excitations seen in the spectra of smaller particles correspond well to the DOS figures. As the cluster size becomes larger, the absorption peak position should approach the shape of the absorption spectrum of the bulk anatase, which has a sharp rise after 3.3 eV, and the maximum absorption is located at 4.7 eV.¹³ As seen in Figure 9, this does not happen at the particle sizes studied here.

The absorptions for $n = \{8, 18, 28, 38\}$ A- and B-structures for each Cartesian direction along with total absorption are presented in Figures 11–14. The clusters were constructed so that in the case of B-structures, the longest dimension is always the z coordinate direction of the system. The total absorption spectrum is the average of each Cartesian direction.

In the case of $(\text{TiO}_2)_{8A}$, the absorptions in x , y , and z directions are quite similar to each other except that y and z directions have more strength around 8 eV as we can see in Figure 11. In the total spectrum, the maximum absorption is located at 9.3 eV (133.32 nm). With $(\text{TiO}_2)_{8B}$ structure, the x and y spectra are similar to each other, but the absorption in z direction is clearly different: The absorption is much stronger, and the maximum is located in lower excitation energy. This is also clearly visible in total absorption. In this case, the largest dimension heavily dominates the total absorption because the

Table 3. Absorption Data for Clusters^a

| structure | d_{\max} [Å] | d_{avg} [Å] | HL gap [eV] | TD gap [eV] | HL gap [nm] | TD gap [nm] |
|------------------------------------|----------------|----------------------|-------------|-------------------|-------------|----------------------|
| (TiO ₂) ₂ | 5.43 | 3.38 | 2.86 | 3.15 | 433.93 | 393.60 |
| (TiO ₂) _{8A} | 9.35 | 6.07 | 2.01 | 2.05 | 617.94 | 604.80 |
| (TiO ₂) _{8B} | 21.52 | 9.79 | 2.79 | 2.90 | 444.66 | 427.53 |
| (TiO ₂) _{18A} | 14.29 | 9.55 | 2.22 | 2.55 ^b | 558.95 | 486.21 ^b |
| (TiO ₂) _{18B} | 22.41 | 11.49 | 1.33 | 2.65 ^b | 935.13 | 467.87 ^b |
| (TiO ₂) _{28A} | 15.98 | 11.24 | 1.03 | 2.25 ^b | 1207.33 | 551.04 ^b |
| (TiO ₂) _{28B} | 29.37 | 13.70 | 1.99 | 2.60 | 624.45 | 476.86 |
| (TiO ₂) _{38A} | 14.84 | 11.51 | 0.37 | 0.80 ^b | 3379.98 | 1549.80 ^b |
| (TiO ₂) _{38B} | 26.57 | 14.20 | 1.86 | 1.95 | 666.14 | 635.82 |

^a Maximum dimension (d_{\max}), average dimension (d_{avg}), DFT HOMO–LUMO gap (HL gap), and TDDFT gap (TD gap). Dimensions are expressed in angstroms, and energy gaps are in electron volts and corresponding wave lengths. ^b Estimated value.

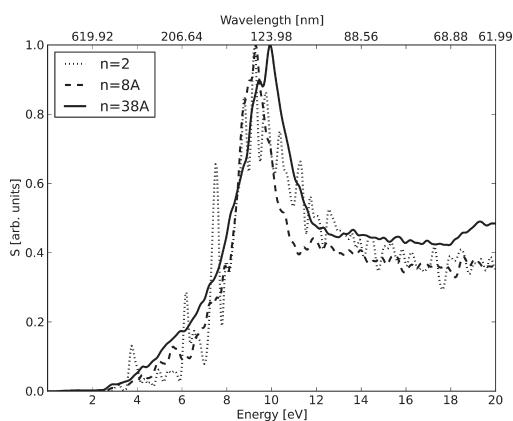


Figure 9. Photoabsorption spectrum for (TiO₂)₂, (TiO₂)_{8A}, and (TiO₂)_{38A} clusters. The *x*-axis represents the excitation energy and the corresponding wavelength. The *y*-axis represents the absorption spectrum.

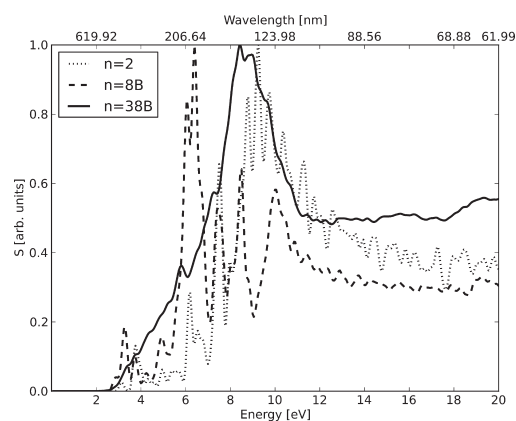


Figure 10. Photoabsorption spectrum for (TiO₂)₂, (TiO₂)_{8B}, and (TiO₂)_{38B} clusters. The *x*-axis represents the excitation energy and the corresponding wavelength. The *y*-axis represents the absorption spectrum.

absorption is so much stronger in *z* direction. The peak absorption is located at 6.4 eV (193.73 nm).

In the case of (TiO₂)_{18A}, the absorptions in different Cartesian directions are quite different from each other with the *z* direction having more strength around 7–8 eV. The maximum value of the total absorption is located at 9.4 eV (131.9 nm) as we can see in Figure 12. In (TiO₂)_{18B} structure, the absorptions in different Cartesian directions are totally different with each other, but the absorption of the longest dimension does not dominate the total absorption so much as it does with (TiO₂)_{8B} because the strength balance is better in this case. The total spectrum of (TiO₂)_{18B} still shows that the structure absorbs more in smaller excitation energies than the A-structure and has maximum absorption at 8.65 eV (143.33 nm).

In the case of (TiO₂)_{28A}, the *x* and *y* directions are almost similar to each other because of the good symmetry in the structure as can be seen in Figure 13, and the *z* direction absorbs slightly more at smaller energy levels. The total absorption spectrum has peak absorption at 9.4 eV (131.9 nm). In the case of (TiO₂)_{18B} structure, the absorption in the longest dimension *z* is clearly shifted to the lower absorption energies. The strength

balance between different Cartesian directions causes the maximum value in the total absorption spectrum at 9.4 eV (131.9 nm), which is exactly the same as it is in the case of the A-structure, but there is also an extra peak in lower excitation energies around 7–7.5 eV.

The absorption of (TiO₂)_{38A} and (TiO₂)_{38B} is presented in Figure 14. In the case of A-structure, the absorption is quite balanced in the *y* and *z* directions except that the *z* direction has generally more strength. In the *x* direction, there is more strength around 8–9 eV, and the total absorption spectrum has maximum absorption at 9.95 eV (124.61 nm). In the case of B-structure, the absorptions in the *x* and *y* directions are quite similar with each other, but the absorption in the *z* direction is again clearly enhanced in smaller energy levels. In the total absorption, the maximum value is located at 8.45 eV (146.73 nm), and so the largest dimension dominates the absorption characteristics again.

When we look at all the photoabsorption spectra, it is clear that the actual gap width has an effect on the absorption threshold, and the lowest allowed excitation energy tends to be higher than the original HOMO–LUMO gap. Also, the position of the maximum absorption seems to blue-shift when the largest

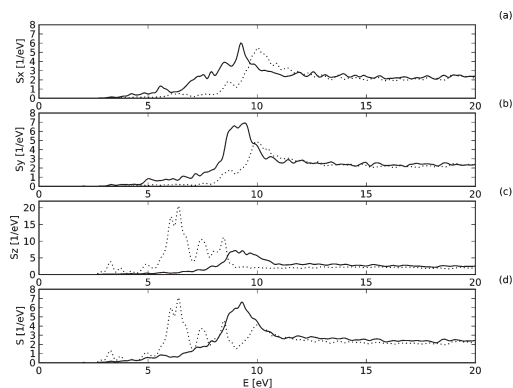


Figure 11. Photoabsorption spectrum for $(\text{TiO}_2)_8$ clusters for the x coordinate direction (a), for the y coordinate direction (b), and for the z coordinate direction (c). The total spectrum is shown in d. The x -axis represents the excitation energy. The y -axis represents the absorption spectrum. The spectra for A-structure are plotted with solid line and for B-structure with dotted line.

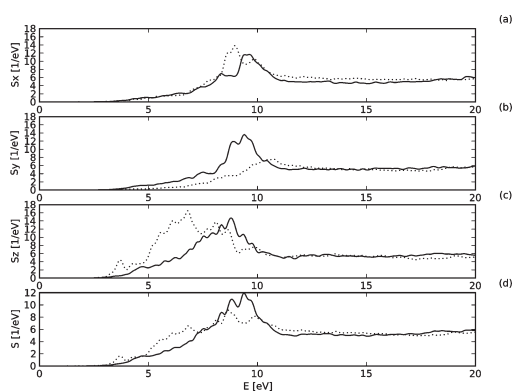


Figure 12. Photoabsorption spectrum for $(\text{TiO}_2)_{18}$ clusters for the x coordinate direction (a), for the y coordinate direction (b), and for the z coordinate direction (c). The total spectrum is shown in d. The x -axis represents the excitation energy. The y -axis represents the absorption spectrum. The spectra for A-structure are plotted with solid line and for B-structure with dotted line.

dimension of the particle gets smaller. The spectral results also show that the total absorption is strongly dependent on the shape of the cluster and not only on the largest dimension or amount of TiO_2 units in the structure.

CONCLUSIONS

The electronic and spectral properties of TiO_2 molecule and two different types of $(\text{TiO}_2)_n$ clusters having $n = \{2, 8, 18, 28, 38\}$ were studied by using DFT and TDDFT methods. The DFT results show slight evidence on the structure-dependent band gap broadening about 0.1–0.74 eV in the case of three of the smallest particles. All the rest of the particles exhibited gaps

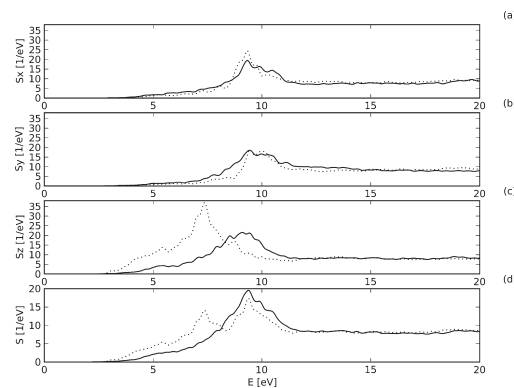


Figure 13. Photoabsorption spectrum for $(\text{TiO}_2)_{28}$ clusters for the x coordinate direction (a), for the y coordinate direction (b), and for the z coordinate direction (c). The total spectrum is shown in d. The x -axis represents the excitation energy. The y -axis represents the absorption spectrum. The spectra for A-structure are plotted with solid line and for B-structure with dotted line.

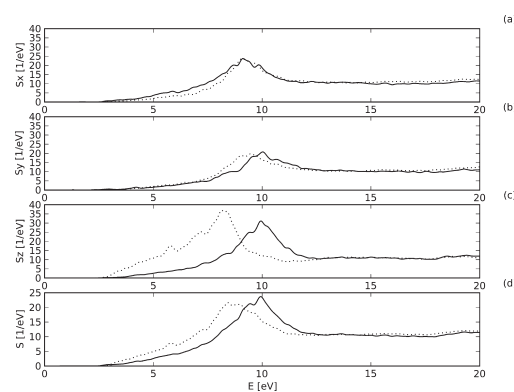


Figure 14. Photoabsorption spectrum for $(\text{TiO}_2)_{38}$ clusters for the x coordinate direction (a), for the y coordinate direction (b), and for the z coordinate direction (c). The total spectrum is shown in d. The x -axis represents the excitation energy. The y -axis represents the absorption spectrum. The spectra for A-structure are plotted with solid line and for B-structure with dotted line.

smaller than that of bulk anatase. The TDDFT results show that the first allowed excitation can be even 1.32 eV larger than the actual DFT HOMO–LUMO gap. What is clear from the results is that the spectral blue-shifts and electronic structure in ultra-small particles are strongly dependent on the shape and structure of the cluster so that in needlelike structures the longest dimension seems to dominate the absorption characteristics. On the other hand, in the case of symmetrical cluster shape, the fundamental absorption characteristics do not seem to depend on the size of the cluster at the particle sizes studied here. The changes in the gap width, the density of states, and the shapes of the spectra indicate that the refractive index function of small TiO_2 particles

will differ from bulk values, and this has to be taken into account in the interpretation of light-scattering measurements in the TSM method.

As the structure and the shape of the particle seem to be very important factors in the absorption of small TiO₂ particles, we are planning to concentrate more on the absorption characteristics of different structural changes in our further studies. We are also interested in modeling the structural effects of OH and SO₃ groups on the cluster surface and their effect on the absorption characteristics of the TiO₂ particles. In our future studies, we will also concentrate on the refractive index function for small TiO₂ particles.

AUTHOR INFORMATION

Corresponding Author

*E-mail: sami.auvinen@lut.fi.

ACKNOWLEDGMENT

We thank the Finnish Academy of Science and Letters and the Research Foundation of Lappeenranta University of Technology for funding our research. We also thank Sachtleben Pigments for their cooperation in this project, Dr. Jussi Enkovaara in CSC-Scientific Computing Ltd., and Dr. Lauri Lehtovaara for technical support with the GPAW software. For the advice regarding the optical constants, we thank Professor Erik Vartiainen at Lappeenranta University of Technology. All calculations were done by using the generous computer resources of CSC-Scientific Computing Ltd., Espoo, Finland.

REFERENCES

- (1) Jalava, J.-P. *Part. Part. Syst. Charact.* **2006**, *23*, 159–164.
- (2) Härkönen, R.; Aro, H.; Kujansivu, L. *Cosmet. Toiletries Manufacture Worldwide* **2003**, 195–201.
- (3) Härkönen, R.; Kujansivu, L. *Pers. Care Mag.* **2003**, *9*, 27–29.
- (4) Karvinen, S.; Lamminmäki, R.-J. *Solid State Sci.* **2003**, *5*, 1159–1166.
- (5) Salmi, M.; Tkachenko, N.; Lamminmäki, R.-J.; Karvinen, S.; Vehmanen, V.; Lemmetyinen, H. *J. Photochem. Photobiol., A* **2005**, *175*, 8–14.
- (6) Jalava, J.-P.; Taavitsainen, V.-M.; Haario, H.; Lamberg, L. *J. Quant. Spectrosc. Radiat. Transfer* **1998**, *60*, 399–409.
- (7) Mishchenko, M.; Travis, L. D. *Appl. Opt.* **1994**, *33*, 7206–7225.
- (8) *Light Scattering by Nonspherical Particles. Theory, Measurements, and Applications*; Mishchenko, M., Hovenier, J. W., Travis, L. D., Eds.; Academic Press: London, 2000; pp 147–221.
- (9) Bohren, C. F.; Huffman, D. R. *Absorption and Scattering of Light by Small Particles*, 1st ed.; Wiley: New York, 1983; pp 227–267.
- (10) Karvinen, S.; Hirva, P.; Pakkanen, T. A. *J. Mol. Struct.* **2003**, *626*, 271–277.
- (11) Kandel, T. A.; Feldhoff, A.; L.; Robben, R. D.; Bahnemann, D. W. *Chem. Mater.* **2010**, *22*, 2050–2060.
- (12) Mo, S.; Ching, W. Y. *Phys. Rev. B* **1995**, *51*, 13023–13032.
- (13) Hosaka, N.; Sekiya, T.; Fujisawa, M.; Satoko, C.; Kurita, S. *J. Electron Spectrosc. Relat. Phenom.* **1996**, *78*, 75–78.
- (14) Asahi, R.; Taga, Y.; Mannstadt, W.; Freeman, A. J. *Phys. Rev. B* **2000**, *61*, 7459–7465.
- (15) Zhang, Y.; Lin, W.; Li, Y.; Ding, K.; Li, J. *J. Phys. Chem. B* **2005**, *109*, 19270–19277.
- (16) Yang, K.; Dai, Y.; Huang, B. *Phys. Rev. B* **2007**, *76*, 195201–1–195201–6.
- (17) Brus, L. *J. Chem. Phys.* **1984**, *80*, 4403–4409.
- (18) Brus, L. *J. Phys. Chem.* **1986**, *90*, 2555–2560.
- (19) Brus, L. *New J. Chem.* **1987**, *11*, 123–127.
- (20) Nozik, A. J.; Williams, F.; Nenadović, M. T.; Rajh, T.; Micić, O. I. *J. Phys. Chem.* **1985**, *89*, 397–399.
- (21) Satoh, N.; Nakashima, T.; Kamikura, K.; Yamamoto, K. *Nat. Nanotechnol.* **2008**, *3*, 106–111.
- (22) Nosaka, Y. *J. Phys. Chem.* **1991**, *95*, 5054–5058.
- (23) Serpone, N.; Lawless, D.; Khairutdinov, R. *J. Phys. Chem.* **1995**, *99*, 16646–16654.
- (24) Lundqvist, M. J.; Nilsing, M.; Persson, P.; Lunell, S. *Int. J. Quantum Chem.* **2006**, *106*, 3214–3234.
- (25) Anpo, M.; Shima, T.; Kodama, S.; Kubokawa, Y. *J. Phys. Chem.* **1987**, *91*, 4305–4310.
- (26) Monticone, S.; Tufeu, R.; Kanaev, A. V.; Scolan, E.; Sanchez, C. *Appl. Surf. Sci.* **2000**, *162*, 565–570.
- (27) Jere, G. V.; Patel, C. C. *J. Sci. Ind. Res.* **1961**, *20B*, 292–293.
- (28) Santacesaria, E.; Tonello, M.; Storti, G.; Pace, R. C.; Carrà, S. *J. Colloid Interface Sci.* **1989**, *111*, 44–53.
- (29) Jalava, J.-P. Formation of TiO₂ Pigment Particles in the Sulphate Process - A Methodological Study. Ph.D.-thesis, University of Turku, Finland, 2000.
- (30) Mortensen, J. J.; Hansen, L. B.; Jacobsen, K. W. *Phys. Rev. B* **2005**, *71*, 035109–1–035109–11.
- (31) Enkovaara, J.; et al. *J. Phys.: Condens. Matter* **2010**, *22*, 253202.
- (32) Bahn, S. R.; Jacobsen, K. W. *Comput. Sci. Eng.* **2002**, *4*, 56–66.
- (33) Blöchl, P. E. *Phys. Rev. B* **1994**, *50*, 17953–17979.
- (34) Blöchl, P. E.; Först, C. J.; Schimpl, J. *Bull. Mater. Sci.* **2003**, *26*, 33–41.
- (35) Walter, M.; Häkkinen, H.; Lehtovaara, L.; Puska, M.; Enkovaara, J.; Rostgaard, C.; Mortensen, J. J. *J. Chem. Phys.* **2008**, *128*, 244101–1–244101–10.
- (36) Perdew, J. P.; Burke, K.; Ernzerhof, M. *Phys. Rev. Lett.* **1996**, *77*, 3865–3868.
- (37) McIntyre, N. S.; Thompson, K. R.; Weltner, W. *J. Phys. Chem.* **1971**, *75*, 3243–3249.
- (38) Albaret, T.; Finocchi, F.; Noguera, C. *Appl. Surf. Sci.* **1999**, *144*, 672–676.
- (39) Cromer, D. T.; Herrington, K. *J. Am. Chem. Soc.* **1955**, *77*, 4708–4709.
- (40) Bekkerman, L. I.; Dobrovol'skii, I. P.; Ivakin, A. A. *Russ. J. Inorg. Chem.* **1976**, *21*, 223–226.
- (41) Zhang, H.; Banfield, J. F. *J. Mater. Chem.* **1998**, *8*, 2073–2076.
- (42) Zhang, H.; Banfield, J. F. *J. Phys. Chem. B* **2000**, *104*, 3481–3487.
- (43) Naicker, P. K.; Cummings, P. T.; Zhang, H.; Banfield, J. F. *J. Phys. Chem. B* **2005**, *109*, 15243–15249.
- (44) Persson, P.; Gebhardt, J. C. M.; Lunell, S. *J. Phys. Chem. B* **2003**, *107*, 3336–3339.

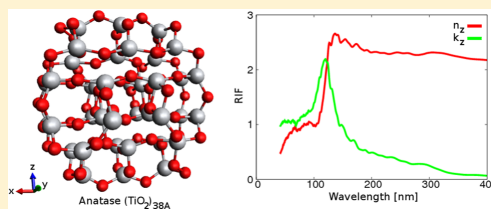
Publication II

S. Auvinen, M. Alatalo, H. Haario, E. Vartiainen, J.P. Jalava, R.J. Lamminmäki,
“Refractive Index Functions of TiO₂ Nanoparticles”

Reprinted from The Journal of Physical Chemistry C 117, 3503-3512 ©(2013),
with permission from American Chemical Society.

Refractive Index Functions of TiO₂ NanoparticlesSami Auvinen,^{*,†} Matti Alatalo,[†] Heikki Haario,[†] Erik Vartiainen,[†] Juho-Pertti Jalava,[‡]
and Ralf-Johan Lamminmäki[‡][†]Lappeenranta University of Technology, Faculty of Technology, Department of Mathematics and Physics, P.O. Box 20, FI-53851 Lappeenranta, Finland[‡]Sachtleben Pigments Oy, Pori, Finland

ABSTRACT: Wavelength-dependent refractive index functions (RIFs) of (TiO₂)_n nanoparticles ($n = 2, 8, 18, 28, \text{ or } 38$) have been calculated by using the data from our previous density functional theory and time-dependent density functional theory photoabsorption calculations. The results show significant blueshifts and increased anisotropy in the RIFs of the nanoparticles, when compared to experimental bulk values. On the basis of the results, we conclude that, in the case of these ultrasmall particles, the RIFs may depend notably on the shape and structure of the cluster and on the other hand the fundamental absorption characteristics do not depend much on the rather limited cluster size range. The results also support the proposition that, in light-scattering measurements, one should not use the bulk RIF to model nanosize particles, at least in the case of TiO₂ particles. Our results shed some light into this computationally and experimentally very challenging area of nanoparticle properties.



■ INTRODUCTION

Titanium dioxide is a wide band gap semiconductor that has gained a lot of interest due to its unique properties. TiO₂ is transparent in the visible region, while it absorbs strongly in the ultraviolet region. It is also photoactive, exhibits high surface reactivity with many chemical agents, and is nontoxic and cost-effective. Titanium dioxide is the most stable white pigment material because it is chemically highly resistant with other substances. In nature, TiO₂ occurs in three polymorphs: anatase, rutile, and brookite; the main source of industrially manufactured TiO₂ is ilmenite FeTiO₃.

In our previous publication,¹ we expressed the importance of submicrometer-size titanium dioxide pigment particles in many applications and described their production control by a recently developed light-scattering-based method, the turbidity spectrum method (TSM).² As it was pointed out,¹ we are now expanding the TSM to nanosize materials. By decreasing the particle size to the nanosize regime, many interesting applications become possible. This decrease changes the optical properties of TiO₂ remarkably from opaque to transparent in the visible range of the light spectrum and to an excellent UV-light blocker. These kinds of nanomaterials are widely used in many applications where visible-light transparency and UV shield are required such as sunscreens, wood lacquers, plastics, cosmetics, foods,^{3,4} and photoelectronics.^{5,6}

In the TSM, the particle size distribution (PSD) is determined from a turbidity spectrum measured from a diluted water solution by means of the T-matrix that is a rigorous light-scattering theory for nonspherical particles.^{7,8} The TSM is now optimized for submicrometer size particles. The light-scattering computing requires the refractive index function (RIF) of the

measured crystal material for all wavelengths used in the measurement. For submicrometer particles, the normal bulk values of RIFs are used. This is justified because, in the literature, we can find experiments proving that, for example, in the case of TiO₂ nanotubes, the diffuse reflectance UV–visible spectra match with bulk values when the nanotubes have diameters up from 5 nm and lengths around 500 nm.^{9,10} However, there are studies indicating that the surface or the finite size of a very small particle can have an effect on the RIF especially at the UV wavelengths.¹¹ The TSM results are in accordance with these findings, and therefore, it is important to clarify this phenomenon. For that, we need to know how the RIF depends on the cluster size and shape.

As a first step, in our earlier paper,¹ electronic and spectral properties of small TiO₂ particles were studied using density functional theory (DFT) and time-dependent density functional theory (TDDFT) calculations. We had a focus on the shape changes of the calculated spectra, which can be related to changes in the RIF. Our results indicated that, in the case of small particles, their RIF can differ from the bulk values, and this has to be taken into account in the interpretation of light-scattering measurements.¹ In this paper, we report the RIFs that are calculated from the photoabsorption spectra for the previously optimized particle structures.¹ We have used two different sets of (TiO₂)_n structures ($n = 2, 8, 18, 28, \text{ or } 38$) along with the (TiO₂)₂ cluster. A similar study for bulk TiO₂

Received: May 31, 2012

Revised: January 30, 2013

Published: January 30, 2013

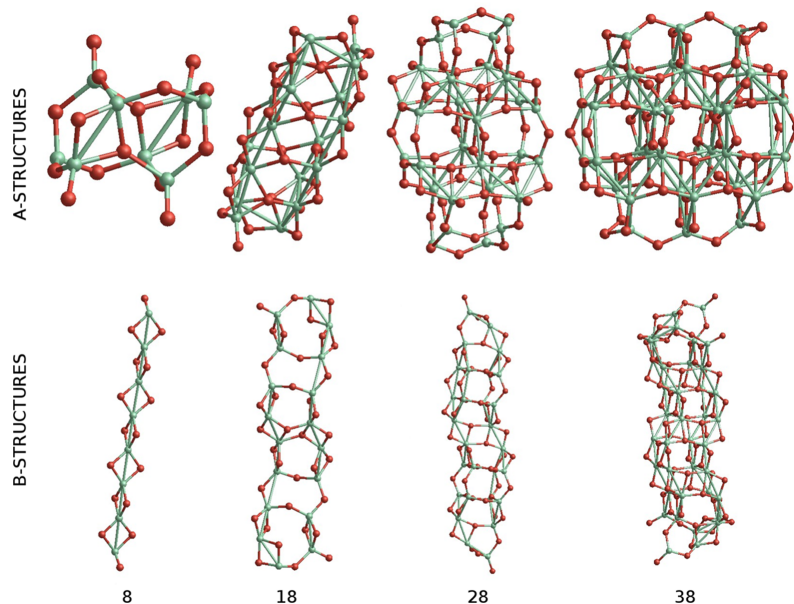


Figure 1. Relaxed A and B structures for $(\text{TiO}_2)_n$ clusters, $n = 8, 18, 28,$ or 38 . Titanium atoms are marked as green, and oxygen atoms are marked as red.

phases has been performed by Rocquefelte et al.¹² We also discuss the dielectric functions (DFs) of the particles.

THEORY

All DFT and TDDFT calculations for this study were performed by using the GPAW software,^{13–16} which is a grid-based code using the projector-augmented wave (PAW) method.^{17,18} The time-propagation TDDFT (TP-TDDFT) implementation in GPAW gives us the photoabsorption spectrum of the cluster as a function of the excitation energy of the photon, in the form of the dipole strength tensor,³⁶ which can be interpreted as a dipole strength function:¹⁹

$$S(\omega) = \frac{2m}{\pi e^2 \hbar} \omega \text{Im} \alpha(\omega) \quad (1)$$

which has units of 1 per electronvolt. In eq 1, m is the mass of the electron, e is the charge of the electron, α is the polarizability of the system, and ω is the angular frequency. On the basis of eq 1, we can formulate the imaginary part of the polarizability to be

$$\text{Im} \alpha(\omega) = \frac{\pi e^2 \hbar S(\omega)}{2m \omega} \quad (2)$$

Because $E = \hbar\omega$, we can write eq 2 as

$$\text{Im} \alpha(\omega) = \frac{\pi e^2 \hbar^2 S(\omega)}{2m E} \quad (3)$$

In eq 3, E is the excitation energy of the electrons, and when we use units $[S(\omega)] = 1/\text{eV}$ and $[E] = \text{eV}$, the term e^2 is canceled out in the equation.

The imaginary part of the DF can now be calculated based on eq 3 by using the equation for electronic polarization,²⁰ taking into consideration the fact that the electric field is local:

$$\epsilon'' = \frac{N_v}{\epsilon_0} \text{Im} \alpha(\omega) \quad (4)$$

where N_v is the valence electron density of the system and ϵ_0 is the vacuum permittivity. The valence electron density of the system in eq 4 can be given by multiplying the number density of molecules \mathcal{N}^{20} by the number of valence electrons per molecule N_v :

$$N_v = \mathcal{N} N_v' = \frac{\rho}{M} A N_v' \quad (5)$$

where ρ and M are the density and molar mass of the substance, respectively, and A is the Avogadro number. Here, we have used the values $\rho = 3.9 \text{ g/cm}^3$ and $M = 79.88 \text{ g/mol}$ for the anatase as given in refs 21 and 22. We have used the values for bulk anatase because the calculation of these values from the structures of the nanoparticles is not always straightforward. The number of valence electrons per molecule was set to be $N_v' = 2$, because all DFT calculations done here were spin paired, having two valence electrons in the highest occupied orbital. The calculated imaginary parts of the DFs were also scaled by dividing with the number of TiO_2 units in the cluster in order to remove the increase of the steady-state level as a function of increasing particle diameter.

The real parts of the DF were calculated by using the Kramers–Kronig relations,²³ and the complex RIFs were calculated from the DFs by using the well-known relations for nonmagnetic material:²⁴

$$n = \frac{1}{\sqrt{2}} [(\epsilon'^2 + \epsilon''^2)^{1/2} + \epsilon']^{1/2} \quad (6)$$

and

$$k = \frac{1}{\sqrt{2}} [(\epsilon'^2 + \epsilon''^2)^{1/2} - \epsilon']^{1/2} \quad (7)$$

As a final step, the acquired RIFs were scaled by a shape-dependent scaling factor:

$$s_a = \left(\frac{l_{\text{mean}}}{l_a} \right)^{1/3} \quad (8)$$

where l_a is the length of the particle along the corresponding crystal axis and

$$l_{\text{mean}} = (l_x l_y l_z)^{1/3} \quad (9)$$

is the cubical effective mean dimension of the particle.

■ COMPUTATIONAL DETAILS

As described in our previous publication,¹ the selected cluster structures were relaxed by using a quasi-Newton minimizer, requiring all forces to be smaller than 0.05 eV/Å in the final structures. In final relaxation runs, the width of the Fermi distribution was set to 0 eV giving us 0 K electronic temperature and integer occupation numbers. The used grid spacing was 0.17 Å, and the cell was set up with nonperiodic boundary conditions so that there was 7 Å of empty space surrounding the cluster. We used the Perdew–Burke–Ernzerhof (PBE) exchange correlation functional,²⁵ conjugate gradient method for the eigensolver, and all calculations were done using only the Γ -point. We did not use spin-polarized calculations, because the tests did not show any evidence about the spin-polarization in TiO₂ nanoparticles.

The photoabsorption spectra for the clusters were calculated by using the TP-TDDFT approach. We used a time step of 16.0 as with 1000 iterations and grid spacing of 0.3 Å. The kick parameter for initial perturbation of the wave functions was set to be 10⁻³. The calculation cell was set up with nonperiodic boundary conditions with 10 Å of empty space surrounding the cluster. The spectra were calculated from the dipole moment files by using a Gaussian broadening of 0.1 eV.

■ RESULTS AND DISCUSSION

Bulk anatase TiO₂ has a tetragonal crystal structure with 12 atoms in the unit cell (four molecules/cell), and it belongs to the $I4_1/amd$ space group.²⁶ The experimental unit cell dimensions are $a = b = 3.784$ Å and $c = 9.515$ Å.²⁶ In our studies, we have used two different sets of TiO₂ structures along with the (TiO₂)₂ cluster: the structures, which were carved from the anatase bulk so that they would be as symmetric as possible in every direction still possessing as much bulklike structure as possible (labeled A), and the corresponding B structures, which were carved from the anatase bulk so that they would be longer in the z coordinate direction, forming a more needlelike structure. The relaxed A and B structures for (TiO₂)_{*n*} clusters are presented in Figure 1. The dimensions of the structures are given in Table 1. The structures were cut so that x , y , and z coordinate axes correspond to the a , b , and c axes in the bulk anatase crystal. The structural analysis of the relaxed structures and their TDDFT photoabsorption spectra are presented in our previous publication.¹

Table 1. Length of the Relaxed Structures in Each Coordinate Direction and Effective Mean Dimension of the Particle^a

| structure | l_x | l_y | l_z | l_{mean} |
|------------------------------------|-------|-------|-------|-------------------|
| (TiO ₂) ₂ | 3.05 | 2.60 | 4.49 | 3.29 |
| (TiO ₂) _{8A} | 6.04 | 5.39 | 6.78 | 6.04 |
| (TiO ₂) _{18A} | 7.77 | 8.56 | 12.33 | 9.36 |
| (TiO ₂) _{28A} | 8.52 | 9.91 | 15.29 | 10.89 |
| (TiO ₂) _{38A} | 12.25 | 9.58 | 12.71 | 11.42 |
| (TiO ₂) _{8B} | 4.67 | 3.26 | 21.43 | 6.89 |
| (TiO ₂) _{18B} | 6.70 | 5.46 | 22.33 | 9.34 |
| (TiO ₂) _{28B} | 6.66 | 5.26 | 29.18 | 10.07 |
| (TiO ₂) _{38B} | 8.72 | 8.46 | 25.40 | 12.33 |

^aAll lengths are given in units of angstrom.

The RIFs for the A structures are presented in Figures 2–4, and the RIFs for the B structures are presented in Figures 5–7, where they are compared to the corresponding experimental data for bulk anatase reported by Jellison et al.²⁷ and Hosaka et al.²⁸ The reference data for bulk anatase was extracted from the articles by carefully digitizing and scaling. When we look at Figures 2, 3, 5, and 6, we see that, in the case of nanoparticles, the optical anisotropy is increased. The bulk anatase crystal structure is optically birefringent, and the RIFs of the a and b axes correspond to each other, while the c axis has a different RIF. This is due to the crystal structure of the ideal anatase bulk, which has an elongated unit cell in the c axis direction. In the case of the nanoparticles, the RIFs of the x and y directions differ from each other, although the basic form of the RIFs is quite similar. This is obviously due to changes in the crystal structure due to the finite size of the particles and thus an increased surface-to-bulk ratio, which was already observed previously in the analysis of the relaxation of the particle models.¹

The maximum peak positions of the imaginary parts of the RIFs are collected in Table 2. According to Figures 2–7, the RIFs of the nanoparticles are generally significantly blueshifted when compared to the experimental values for bulk anatase. This was also predicted by the previous results on photoabsorption spectra.¹ Table 2 also contains the calculated blueshifts compared with experimental bulk data by Jellison et al.²⁷ and Hosaka et al.²⁸ When compared to the data set of Jellison et al.²⁷, the largest blueshift of the peak value of the imaginary part is 162 nm in k_z of the (TiO₂)_{38A} cluster, and the average blueshift in the imaginary part of the RIF is 131 nm. When we compare the nanoparticle RIFs to the data set of Hosaka et al.²⁸, the largest blueshift of the peak value of the imaginary part is 141 nm in k_y of the (TiO₂)_{18B} cluster, and the average blueshift in the imaginary part of the RIF is 101 nm. The negative values of $\Delta\lambda_{\text{zmax2}}$ in the case of (TiO₂)_{8B}, (TiO₂)_{18B}, and (TiO₂)_{28B} indicate that the peak value is actually redshifted.

The refractive index data of Hosaka et al.²⁸ is measured for much smaller wavelengths than the data of Jellison et al.²⁷, so it is better to compare our nanoparticle RIFs to this data set. In the RIF data of Hosaka et al.,²⁸ one can notice small peaks in n_x at 120, 143, and 165 nm. The k_a has corresponding peaks at 120, 140, and 155 nm. The n_y has peaks at 124 and 159 nm, and k_c has peaks at 121 and 148 nm. As we can see in Figures 2–7 and Table 2, in the case of A structures, the maximum peak positions of the nanoparticle RIFs correspond quite well to these peaks at smaller wavelengths. In the case of B structures,

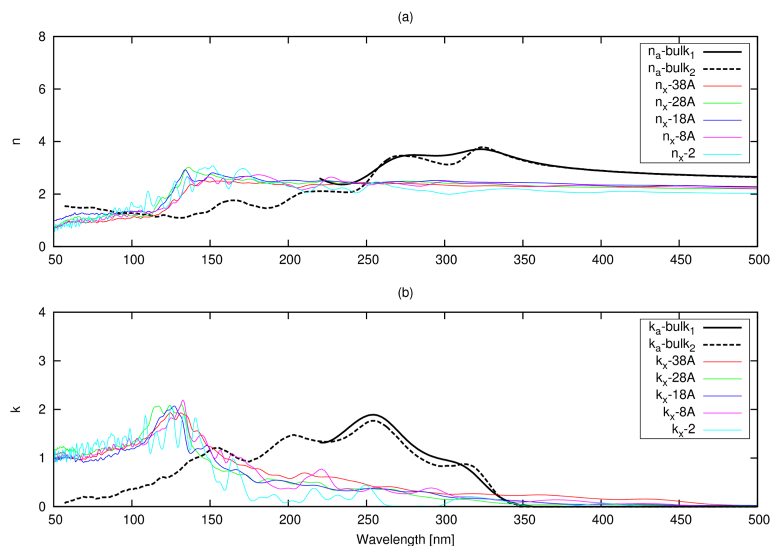


Figure 2. Calculated RIFs of A structures and the $(\text{TiO}_2)_2$ cluster in the x coordinate direction (a axis in the crystal) compared to the experimental values for anatase bulk (depicted as black). Experimental values for bulk anatase are from Jellison et al.²⁷ (bulk_1) and Hosaka et al.²⁸ (bulk_2).

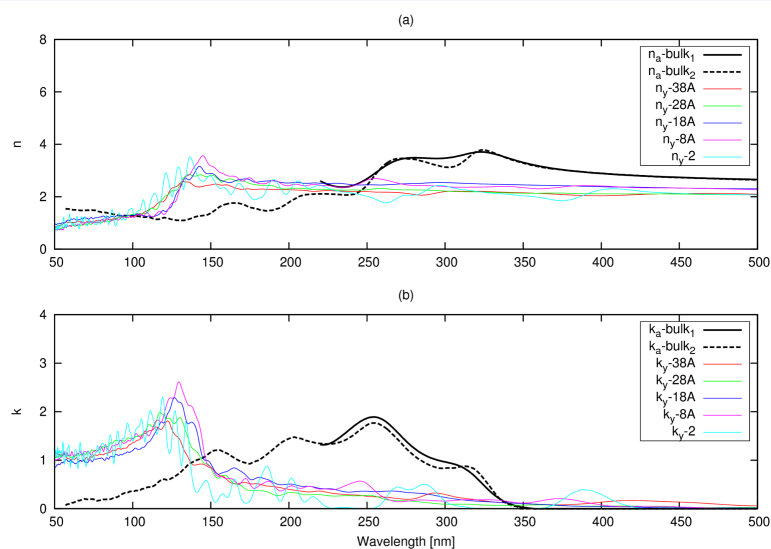


Figure 3. Calculated RIFs of A structures and the $(\text{TiO}_2)_2$ cluster in the y coordinate direction (a axis in the crystal) compared to the experimental values for anatase bulk (depicted as black). Experimental values for bulk anatase are from Jellison et al.²⁷ (bulk_1) and Hosaka et al.²⁸ (bulk_2).

the correspondence is quite good with n_x and k_x , but with n_z and k_z , the correspondence is not so good. On the basis of these findings, we can conclude that the weight of the RIFs moves toward shorter wavelengths when the particle size is decreased.

From Figures 2–7 and Table 2, we see that the shape and structure of the particle can have a more pronounced effect on the RIF than the actual particle size in the size area studied here. Generally, the RIFs of nanoparticles are clearly blue-shifted, but in this set of model structures, we do not see any

size-dependent shift toward the bulk RIF. This is of course due to the relatively small particle size variation in the test set. What is also visible in Figures 2–7 is that the previously reported changes in the gap width of the nanoparticles do not seem to significantly affect the RIF of the particles. We have not used the Tauc Plot analysis²⁹ to resolve the band gaps from RIF data because the calculated band gaps were already reported in our previous article.¹ These results strengthen our previous conclusion that, in the case of ultrasmall particles, the spectra

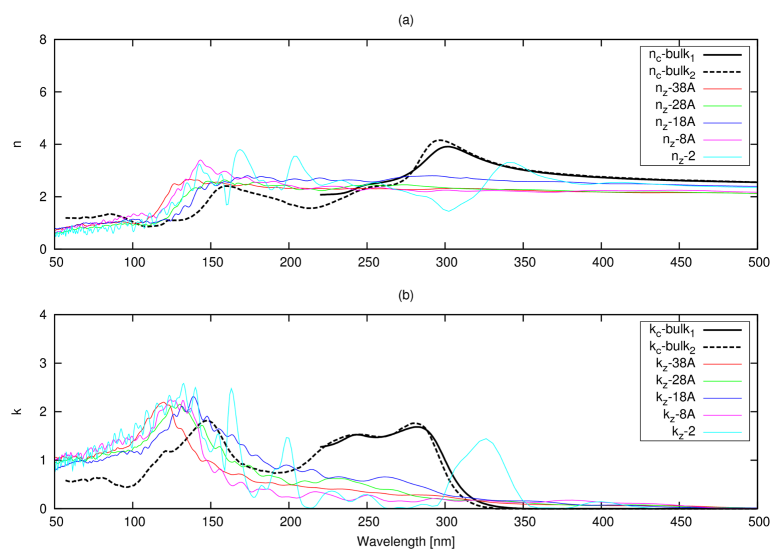


Figure 4. Calculated RIFs of A structures and the $(\text{TiO}_2)_2$ cluster in the z coordinate direction (z axis in the crystal) compared to the experimental values for anatase bulk (depicted as black). Experimental values for bulk anatase are from Jellison et al.²⁷ (bulk_1) and Hosaka et al.²⁸ (bulk_2).

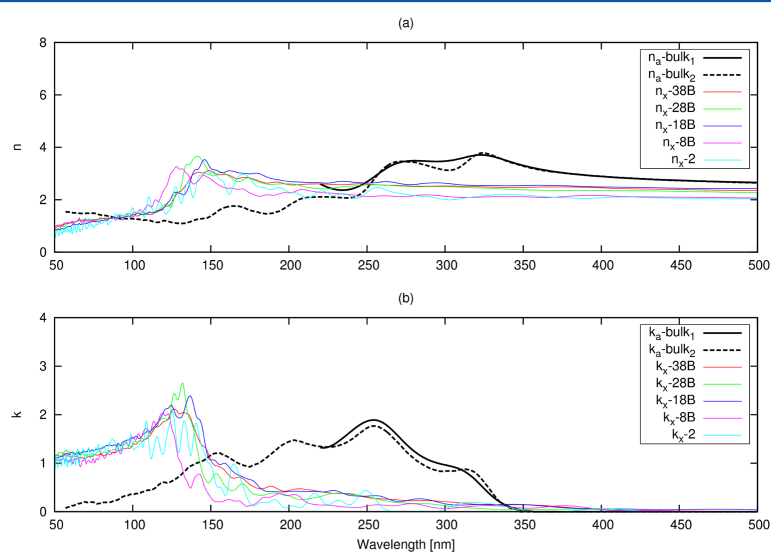


Figure 5. Calculated RIFs of B structures and the $(\text{TiO}_2)_2$ cluster in the x coordinate direction (a axis in the crystal) compared to the experimental values for anatase bulk (depicted as black). Experimental values for bulk anatase are from Jellison et al.²⁷ (bulk_1) and Hosaka et al.²⁸ (bulk_2).

and electronic structure may depend notably on the shape and structure of the cluster and on the other hand the fundamental absorption characteristics do not seem to depend so much on the size of the cluster at the particle sizes studied here.¹ It should be cleared out here that, with shape and structure, we refer to the actual shape of the cluster (prolonged or symmetric) and structural changes on the cluster surface (coordination and bonding due to different carving from bulk structure), as opposed to size, which is considered as a

combination of dimensions and the amount of TiO_2 units in the cluster.

Besides the RIFs, the underlying dielectric properties are also important. The real and imaginary parts of DFs for clusters and the TiO_2 molecule are presented in Figures 8–11. In these figures, we have combined the DFs in perpendicular polarization directions (x and y) by calculating the average value for them. This way we can easily compare our cluster DFs with ones computed for bulk anatase by Asahi et al.³⁰ As we can see

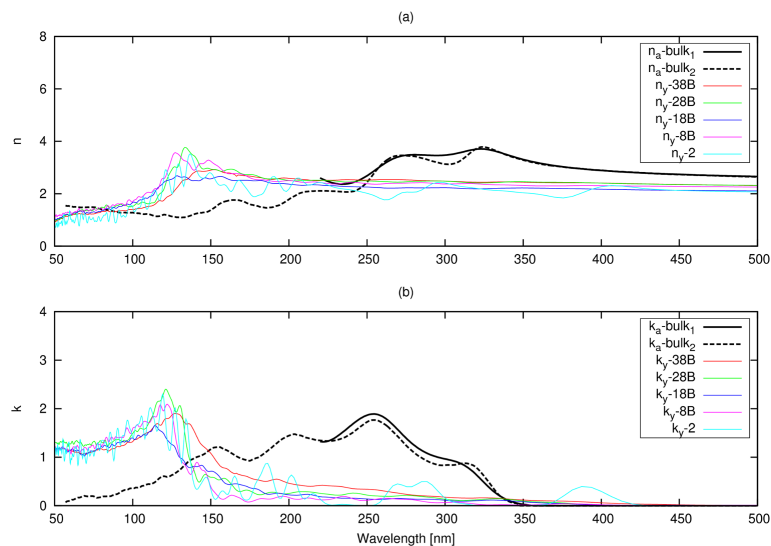


Figure 6. Calculated RIFs of B structures and the $(\text{TiO}_2)_2$ cluster in the y coordinate direction (a axis in the crystal) compared to the experimental values for anatase bulk (depicted as black). Experimental values for bulk anatase are from Jellison et al.²⁷ (bulk₁) and Hosaka et al.²⁸ (bulk₂).

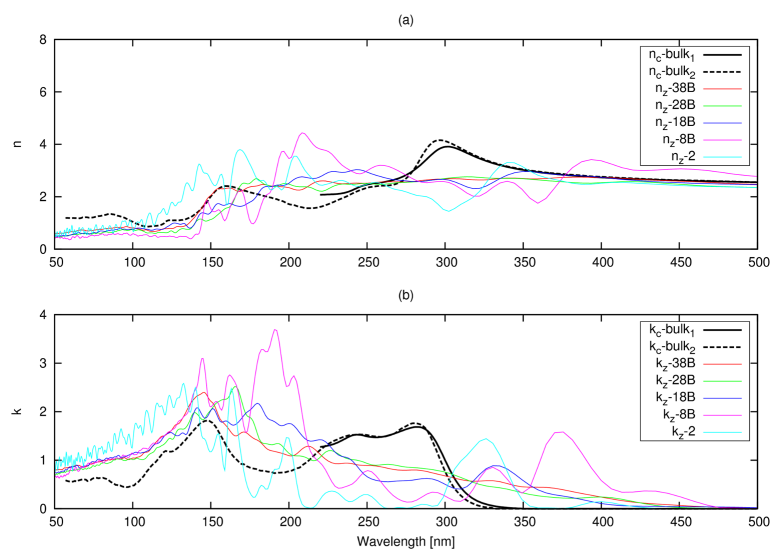


Figure 7. Calculated RIFs of B structures and the $(\text{TiO}_2)_2$ cluster in the z coordinate direction (c axis in the crystal) compared to the experimental values for anatase bulk (depicted as black). Experimental values for bulk anatase are from Jellison et al.²⁷ (bulk₁) and Hosaka et al.²⁸ (bulk₂).

in Figures 8–11 and from ref 30, the peak positions of the DFs for the clusters correspond well with peaks in computational bulk data and with the experimental data of Jellison et al.²⁷ and Hosaka et al.,²⁸ especially in the z direction. The difference is that the clusters have much smaller DFs at the lower energy region around 3–7 eV. These peaks correspond to transitions from the valence bands to t_{2g} orbitals.³⁰

As was already concluded with density of states (DOS) results in our previous publication,¹ the edges of the valence

and conduction bands are more localized in the case of the clusters. The more localized the t_{2g} orbitals are, the lower the absorption peaks are at these energy levels when compared to transitions to e_g conduction bands at higher energy levels.³⁰ Also, the DOS at the edges of the band gap is relatively smaller than it is in the case of bulk structures.¹ This indicates that, when the size and shape-dependent formation of band structure reaches the point where t_{2g} orbitals become less localized, the clusters start to have more bulklike DFs and RIFs. As we

Table 2. Wavelengths (nm) of the Maximum Peak in the Imaginary Part of the RIF along Different Crystal Axes and Their Blueshifts Compared to the Experimental Values for Anatase Bulk^a

| structure | $\lambda_{x\max}$ | $\lambda_{y\max}$ | $\lambda_{z\max}$ | bulk ₁ | | | bulk ₂ | | |
|------------------------------------|-------------------|-------------------|-------------------|--------------------------|--------------------------|--------------------------|--------------------------|--------------------------|--------------------------|
| | | | | $\Delta\lambda_{x\max1}$ | $\Delta\lambda_{y\max1}$ | $\Delta\lambda_{z\max1}$ | $\Delta\lambda_{x\max2}$ | $\Delta\lambda_{y\max2}$ | $\Delta\lambda_{z\max2}$ |
| (TiO ₂) ₂ | 125 | 119 | 133 | 129 | 135 | 149 | 130 | 136 | 15 |
| (TiO ₂) _{8A} | 133 | 130 | 124 | 121 | 124 | 158 | 122 | 125 | 24 |
| (TiO ₂) _{18A} | 127 | 127 | 139 | 127 | 127 | 143 | 128 | 128 | 9 |
| (TiO ₂) _{28A} | 132 | 118 | 130 | 122 | 136 | 152 | 123 | 137 | 18 |
| (TiO ₂) _{38A} | 125 | 122 | 120 | 129 | 132 | 162 | 130 | 133 | 28 |
| (TiO ₂) _{8B} | 119 | 122 | 191 | 135 | 132 | 91 | 136 | 133 | -43 |
| (TiO ₂) _{18B} | 137 | 114 | 180 | 117 | 140 | 102 | 118 | 141 | -32 |
| (TiO ₂) _{28B} | 132 | 121 | 165 | 122 | 133 | 117 | 123 | 134 | -17 |
| (TiO ₂) _{38B} | 127 | 127 | 146 | 127 | 127 | 136 | 128 | 128 | 2 |
| bulk ₁ (expt) | 254 | 254 | 282 | | | | | | |
| bulk ₂ (expt) | 255 | 255 | 148 | | | | | | |

^aThe experimental data for bulk₁ is from Jellison et al.²⁷, and the experimental data for bulk₂ is from Hosaka et al.²⁸ The values $\Delta\lambda_{x\max1}$, $\Delta\lambda_{y\max1}$, and $\Delta\lambda_{z\max1}$ are the blueshifts relative to bulk₁ data, and $\Delta\lambda_{x\max2}$, $\Delta\lambda_{y\max2}$, and $\Delta\lambda_{z\max2}$ are the corresponding values relative to bulk₂ data.

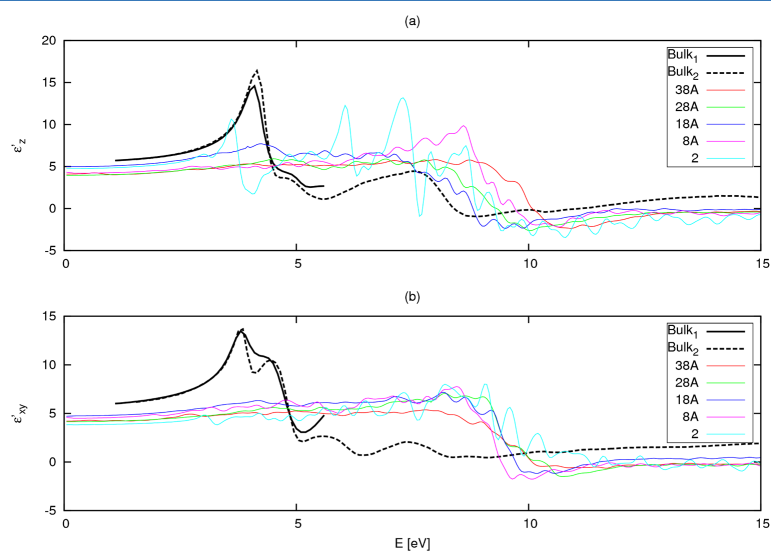


Figure 8. Calculated real parts of DFs for A structures and the (TiO₂)₂ cluster in the *z* coordinate direction (*c* axis in the crystal) (a), and in the *xy* coordinate direction (*a* axis in the crystal) (b). The calculated values are compared to the experimental values for anatase bulk (depicted as black). Experimental values for bulk anatase are from Jellison et al.²⁷ (bulk₁) and Hosaka et al.²⁸ (bulk₂).

already stated with the RIF results, the structure of the particle plays an important role in this band formation, as we can clearly see in the case of the (TiO₂)_{8B} cluster. Figures 10 and 11 show that it has more absorption at the lower energy levels, and our earlier DOS results¹ confirm that, in the case of the (TiO₂)_{8B} cluster, the localization of the band edges is lower than in the case of the other clusters (especially with *t_{2g}* orbitals).

All the results support the proposition that, in the TSM method, one should not use the bulk RIF to compute the PSD of nanosize particles. However, due to the limited size range achievable with first principles calculations, the exact size range of the particles where the transition toward the bulk RIF begins is still unknown. We will consider this in our future studies. The size of the largest particles studied here is already at the size range of industrial interest, and the RIFs of the largest particles

can be used in parametrization when expanding the TSM to nanosize materials.

When interpreting the results, we should keep in mind that we are comparing computational results to experimental values, so the blueshifts reported here are not absolute and may contain small errors due to nature of the approximations used in DFT and TDDFT methods. In our calculations, we have used the PBE generalized gradient approximation (GGA) exchange correlation functional,²⁵ which provides many improvements opposed to original local density approximations. It is still generally known that the DFT and GGA approach tends to underestimate the fundamental band gap of semiconductors. This means that the actual blueshifts can be bigger than reported here. The underestimated gap in the imaginary part of the DF also affects the real part of the DF via

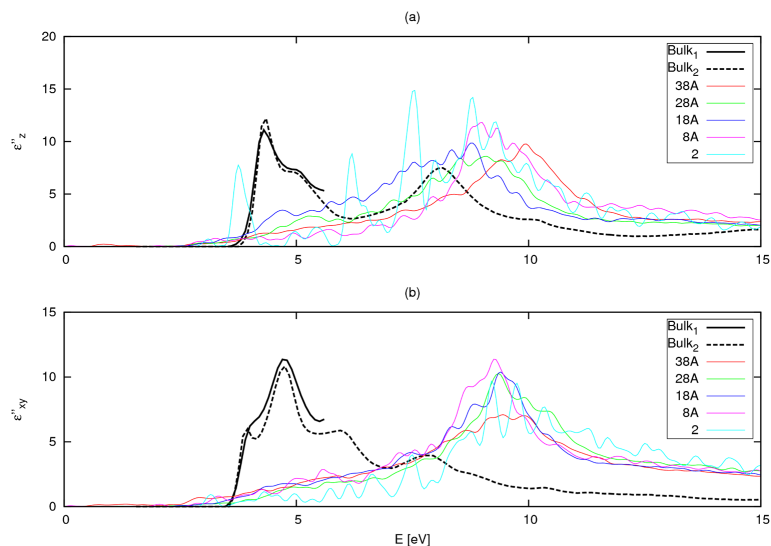


Figure 9. Calculated imaginary parts of DFs for A structures and the $(\text{TiO}_2)_2$ cluster in the z coordinate direction (c axis in the crystal) (a) and in the xy coordinate direction (a axis in the crystal) (b). The calculated values are compared to the experimental values for anatase bulk (depicted as black). Experimental values for bulk anatase are from Jellison et al.²⁷ (bulk₁) and Hosaka et al.²⁸ (bulk₂).

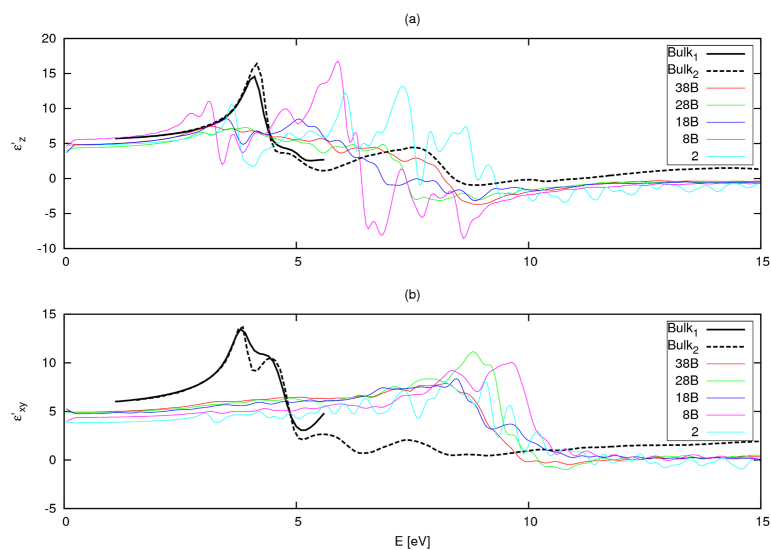


Figure 10. Calculated real parts of DFs for B structures and the $(\text{TiO}_2)_2$ cluster in the z coordinate direction (c axis in the crystal) (a) and in the xy coordinate direction (a axis in the crystal) (b). The calculated values are compared to the experimental values for anatase bulk (depicted as black). Experimental values for bulk anatase are from Jellison et al.²⁷ (bulk₁) and Hosaka et al.²⁸ (bulk₂).

Kramers–Kronig relations. However, the trends and general directions of the results are valid.

In the real-life applications (especially in the case of pigments), TiO_2 particles are also often in solutions containing water and other chemicals, such as sulfuric acid and possible trace elements,³¹ possibly providing adatoms on the particle surfaces. Our current results do not take into account the effect

of surface adatoms, which may change the photoabsorption of the particles due to the changes in the electronic structure.³² We are currently working on effects of on-surface OH and SO_3 on the photoabsorption of TiO_2 nanoparticles, and these results will be published later.

Regarding the importance of exchange-correlation kernels, one should note that there are many ongoing research projects

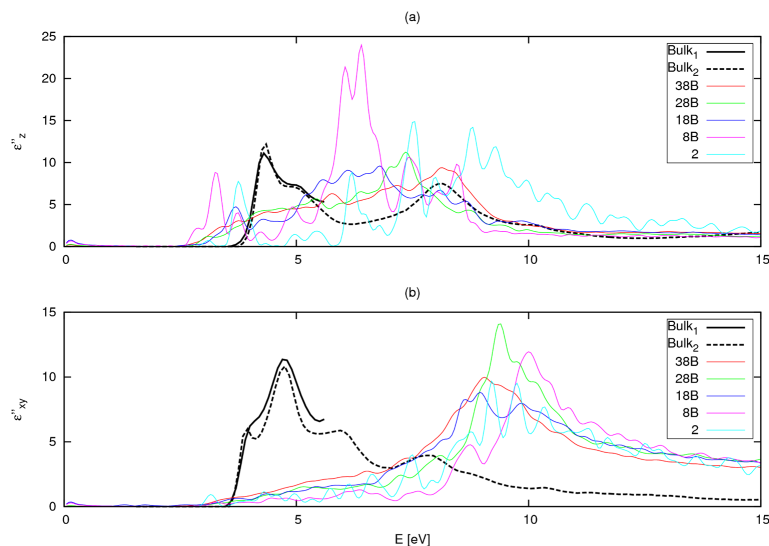


Figure 11. Calculated imaginary parts of DFs for B structures and the $(\text{TiO}_2)_2$ cluster in the z coordinate direction (c axis in the crystal) (a) and in the xy coordinate direction (a axis in the crystal) (b). The calculated values are compared to the experimental values for anatase bulk (depicted as black). Experimental values for bulk anatase are from Jellison et al.²⁷ (bulk₁) and Hosaka et al.²⁸ (bulk₂).

that aim to improve the earlier approximations. One example is a recent study of Gatti, who derived an exact form for the exchange-correlation kernel for time-dependent current density functional theory, allowing successful computation of electronic spectra of solids and nanosystems.³³

In the case of the bulk semiconductors, there are studies suggesting that employing the Bethe–Salpeter equation (BSE)³⁴ can lead to improved optical results when compared to experimental values.³⁵ On the other hand, there are also studies indicating that, in the case of nanoparticles, the TDDFT approach can actually give more accurate results when compared to the BSE approach, as was found in the case of Si nanoparticles by Benedict et al.³⁶ Also the BSE implementation in the GPAW software is restricted to periodic systems, leading to computationally demanding calculations in the case of nanoparticles. Thus, we have neglected the use of the BSE approach in our studies.

However, it should be stressed that the role of excitonic or electron–hole effects can have great importance in some cases of the nanostructures, underpinning the influence of structure and size. In 2008, Varsano et al. studied the optical saturation driven by exciton confinement in molecular chains by TDDFT methods and reported on the breakdown of commonly adopted approximations in anisotropic structures.³⁷ They concluded that the failure of simple local and semilocal functionals is due to the lack of memory effects, spatial ultranlocality, and self-interaction corrections.³⁷ They also stated that simple approximations work better with small band gap systems, because these effects get smaller when the band gap is reduced.³⁷

Our results reported in the present work shed some light into this computationally and experimentally very challenging area of nanoparticle properties and show that the use of the bulk RIF to model nanosize particles in light-scattering measurements is questionable, at least in the case of TiO_2 particles. The

proper incorporation of excitonic and memory effects could still greatly further improve our current results, and other similar calculations, providing more information to fully clarify the optical behavior of nanoparticles.

CONCLUSIONS

RIFs of $(\text{TiO}_2)_n$ nanoparticles ($n = 2, 8, 18, 28, \text{ or } 38$) were calculated based on the TDDFT data from our previous photoabsorption calculations.¹ The computational results were compared to the experimental ellipsometry data for the RIF of bulk anatase crystal reported earlier by Jellison et al.²⁷ and Hosaka et al.²⁸ The results show significant blueshifts (the averages are 131 nm in the imaginary part of the RIF when compared to data from Jellison et al.²⁷ and 101 nm when compared to data from Hosaka et al.²⁸) and increased anisotropy in the RIFs of the nanoparticles. The results indicate that, in the case of ultrasmall TiO_2 particles, the structure of the particle may have a more pronounced effect on the RIF than the size of the particle and that the weight of the RIFs moves toward shorter wavelengths when the particle size is decreased. Current results show also that the anisotropy and blueshifts of the particle RIFs have to be taken into account in the TSM and light-scattering measurements of the small TiO_2 particles. However, the particle size on which the transformation of the particle RIF toward the bulk RIF starts still remains unknown. More studies are still needed to fully clarify this phenomenon.

AUTHOR INFORMATION

Corresponding Author

*E-mail: sami.auvinen@lut.fi.

Notes

The authors declare no competing financial interest.

ACKNOWLEDGMENTS

We want to acknowledge the Finnish Academy of Science and Letters, the Research Foundation of Lappeenranta University of Technology, and Sachtleben Pigments Oy, Pori, Finland, for funding this research. The computational resources were provided by CSC-Scientific Computing Ltd., Espoo, Finland.

REFERENCES

- (1) Auvinen, S.; Alatalo, M.; Haario, H.; Jalava, J.-P.; Lamminmäki, R.-J. Size and Shape Dependence of the Electronic and Spectral Properties in TiO₂ Nanoparticles. *J. Phys. Chem. C* **2011**, *115*, 8484–8493.
- (2) Jalava, J.-P.; Taavitsainen, V.-M.; Haario, H.; Lamberg, L. Determination of Crystal and Particle Size Distributions from Turbidity Spectrum of TiO₂ Pigment by Means of T-Matrix. *J. Quant. Spectrosc. Radiat. Transfer* **1998**, *60*, 399–409.
- (3) Härkönen, R.; Aro, H.; Kujansivu, L. Optimisation of the Dispersing Process of Ultrafine Titanium Dioxide UV-TITAN M170: Effects on Sun Protection Factor and Transparency. *Cosmet. Toiletries Manuf. Worldwide* **2003**, 195–201.
- (4) Härkönen, R.; Kujansivu, L. Ultrafine Titanium Dioxide: Effects on UV Protection. *Pers. Care Mag.* **2003**, *9*, 27–29.
- (5) Karvinen, S.; Lamminmäki, R.-J. Preparation and Characterization of Mesoporous Visible-Light-Active Anatase. *Solid State Sci.* **2003**, *5*, 1159–1166.
- (6) Salmi, M.; Tkachenko, N.; Lamminmäki, R.-J.; Karvinen, S.; Vehmanen, V.; Lemmetyinen, H. Femtosecond to Nanosecond Spectroscopy of Transition Metal-Doped TiO₂ Particles. *J. Photochem. Photobiol. A* **2005**, *175*, 8–14.
- (7) Mishchenko, M.; Travis, L. D. Light Scattering by Polydispersions of Randomly Oriented Spheroid with Sizes Comparable to Wavelength of Observation. *Appl. Opt.* **1994**, *33*, 7206–7225.
- (8) *Light Scattering by Nonspherical Particles. Theory, Measurements, and Applications*; Mishchenko, M., Hovenier, J. W., Travis, L. D., Eds.; Academic Press: London, 2000; pp 147–221.
- (9) Tang, Z.-R.; Zhang, Y.; Xu, Y.-J. Tuning the Optical Property and Photocatalytic Performance of Titanate Nanotube toward Selective Oxidation of Alcohols under Ambient Conditions. *ACS Appl. Mater. Interfaces* **2012**, *4*, 1512–1520.
- (10) Mukherjee, B.; Smith, Y. R.; Subramanian, V. R. CdSe Nanocrystal Assemblies on Anodized TiO₂ Nanotubes: Optical, Surface, and Photochemical Properties. *J. Phys. Chem. C* **2012**, *116*, 15175–15184.
- (11) Bohren, C. F.; Huffman, D. R. *Absorption and Scattering of Light by Small Particles*, 1st ed.; Wiley: New York, 1983; pp 227–267.
- (12) Rocquefelte, X.; Goubin, F.; Koo, H.-J.; Whangbo, M.-H.; Jobic, S. Investigation of the Origin of the Empirical Relationship between Refractive Index and Density on the Basis of First Principles Calculations for the Refractive Indices of Various TiO₂ Phases. *Inorg. Chem.* **2004**, *43*, 2246–2251.
- (13) Mortensen, J. J.; Hansen, L. B.; Jacobsen, K. W. Real-Space Grid Implementation of the Projector Augmented Wave Method. *Phys. Rev. B* **2005**, *71*, 035109-1–035109-11.
- (14) Enkovaara, J.; Rostgaard, C.; Mortensen, J. J.; Chen, J.; Dulak, M.; Ferrighi, L.; Gavnholt, J.; Glinsvad, C.; Haikola, V.; Hansen, H. A.; et al. Electronic Structure Calculations with GPAW: A Real-Space Implementation of the Projector Augmented-Wave Method. *J. Phys.: Condens. Mater.* **2010**, *22*, 253202-1–253202-24.
- (15) Bahn, S. R.; Jacobsen, K. W. An Object-Oriented Scripting Interface to a Legacy Electronic Structure Code. *Comput. Sci. Eng.* **2002**, *4*, 56–66.
- (16) Walter, M.; Häkkinen, H.; Lehtovaara, L.; Puska, M.; Enkovaara, J.; Rostgaard, C.; Mortensen, J. J. Time-Dependent Density-Functional Theory in the Projector Augmented-Wave Method. *J. Chem. Phys.* **2008**, *128*, 244101-1–244101-10.
- (17) Blöchl, P. E. Projector Augmented-Wave Method. *Phys. Rev. B* **1994**, *50*, 17953–17979.
- (18) Blöchl, P. E.; Först, C. J.; Schimpl, J. Projector Augmented Wave Method: Ab Initio Molecular Dynamics with Full Wave Functions. *Bull. Mater. Sci.* **2003**, *26*, 33–41.
- (19) Martin, R. M. *Electronic Structure: Basic Theory and Practical Methods*, 1st ed.; Cambridge University Press: Cambridge, U.K., 2004; pp 406–417.
- (20) Atkins, P. W.; Friedman, R. S. *Molecular Quantum Mechanics*, 3rd ed.; Oxford University Press: New York, 1997; pp 394–395.
- (21) Clark, R. J. H. *The Chemistry of Titanium and Vanadium: An Introduction to the Chemistry of the Early Transition Elements*, 1st ed.; Elsevier: New York, 1968; pp 270–271.
- (22) *CRC Handbook of Chemistry and Physics*, 68th ed.; Weast, R. C., Ed.; CRC Press: Boca Raton, FL, 1987; p B140.
- (23) Lucarini, V.; Peiponen, K.-E.; Saarinen, J. J.; Vartiainen, E. M. *Kramers-Kronig Relations in Optical Materials Research*, 1st ed.; Springer: Berlin, Germany, 2005; pp 1–135.
- (24) Bohren, C. F.; Huffman, D. R. *Absorption and Scattering of Light by Small Particles*, 1st ed.; Wiley: New York, 1983; pp 227–228.
- (25) Perdew, J. P.; Burke, K.; Ernzerhof, M. Generalized Gradient Approximation Made Simple. *Phys. Rev. Lett.* **1996**, *77*, 3865–3868.
- (26) Cromer, D. T.; Herrington, K. The Structures of Anatase and Rutile. *J. Am. Chem. Soc.* **1955**, *77*, 4708–4709.
- (27) Jellison, G. E.; Boatner, L. A.; Budai, J. D.; Jeong, B.-S.; Norton, D. P. Spectroscopic Ellipsometry of Thin Film and Bulk Anatase (TiO₂). *J. Appl. Phys.* **2003**, *93*, 9537–9541.
- (28) Hosaka, N.; Sekiya, T.; Satoko, C.; Kurita, S. Optical Properties of Single-Crystal Anatase TiO₂. *J. Phys. Soc. Jpn.* **1997**, *66*, 877–880.
- (29) *Handbook of Ellipsometry*, 1st ed.; Tompkins, H. G., Irene, E. A., Eds.; William Andrew Publishing: New York, 2005; pp 145–146.
- (30) Asahi, R.; Taga, Y.; Mannstadt, W.; Freeman, A. J. Electronic and Optical Properties of Anatase TiO₂. *Phys. Rev. B* **2000**, *61*, 7459–7465.
- (31) Jalava, J.-P. Precipitation and Properties of TiO₂ Pigments in the Sulfate Process. 1. Preparation of the Liquor and Effects of Iron(II) in Isoviscous Liquor. *Ind. Eng. Chem. Res.* **1992**, *31*, 608–611.
- (32) Iacomino, A.; Cantele, G.; Ninno, D.; Marri, I.; Ossicini, S. Structural, Electronic, and Surface Properties of Anatase TiO₂ Nanocrystals from First Principles. *Phys. Rev. B* **2008**, *78*, 075405-1–075405-11.
- (33) Gatti, M. Design of Effective Kernels for Spectroscopy and Molecular Transport: Time-Dependent Current-Density-Functional Theory. *J. Chem. Phys.* **2011**, *134*, 084102-1–084102-5.
- (34) Salpeter, E. E.; Bethe, H. A. A Relativistic Equation for Bound-State Problems. *Phys. Rev.* **1951**, *84*, 1232–1242.
- (35) Yan, J.; Jacobsen, K. W.; Thygesen, K. S. Optical Properties of Bulk Semiconductors and Graphene/Boron Nitride: The Bethe-Salpeter Equation with Derivative Discontinuity-Corrected Density Functional Energies. *Phys. Rev. B* **2012**, *86*, 045208-1–045208-11.
- (36) Benedict, L. X.; Puzder, A.; Williamson, A. J.; Grossman, J. C.; Galli, G.; Klepeis, J. E.; Raty, J.-Y.; Pankratov, O. Calculation of Optical Absorption Spectra of Hydrogenated Si Clusters: Bethe-Salpeter Equation Versus Time-Dependent Local-Density Approximation. *Phys. Rev. B* **2003**, *68*, 085310-1–085310-8.
- (37) Varsano, D.; Marini, A.; Rubio, A. Optical Saturation Driven by Exciton Confinement in Molecular Chains: A Time-Dependent Density-Functional Theory Approach. *Phys. Rev. Lett.* **2008**, *101*, 133002-1–133002-4.

Publication III

A. Kumar, S. Auvinen, M. Trivedi, R. Chauhan, M. Alatalo "Synthesis, Characterization and Light Harvesting Properties of Nickel(II) Diimine Dithiolate Complexes"

Reprinted from Spectrochimica Acta Part A: Molecular and Biomolecular Spectroscopy 115, 106-110 ©(2013), with permission from Elsevier B.V..



Contents lists available at SciVerse ScienceDirect

Spectrochimica Acta Part A: Molecular and Biomolecular Spectroscopy

journal homepage: www.elsevier.com/locate/saa



Synthesis, characterization and light harvesting properties of nickel(II) diimine dithiolate complexes



Abhinav Kumar^{a,*}, Sami Auvinen^b, Manoj Trivedi^c, Ratna Chauhan^d, Matti Alatalo^b

^aDepartment of Chemistry, Faculty of Science, University of Lucknow, Lucknow 226 007, India

^bFaculty of Technology, Department of Mathematics and Physics, Lappeenranta University of Technology, Lappeenranta FI-53851, Finland

^cDepartment of Chemistry, University of Delhi, Delhi, India

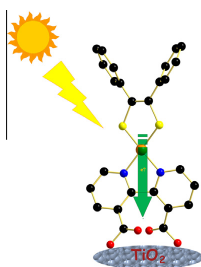
^dCentre for Materials for Electronics Technologies, Pune, India

HIGHLIGHTS

- Four Ni(II) diimine dithiolate prepared from Ni(II) dithiolene.
- Their light harvesting properties investigated using these compounds as photosensitizers.
- Quantum chemical calculations have been performed to explain the nature of charge transfer.
- Effect of change in position of anchoring group on light harvesting parameters monitored.

GRAPHICAL ABSTRACT

Four Ni(II) diimine dithiolate complexes have been prepared from $[\text{Ni}(\text{S}_2\text{C}_2\text{Ph}_2)_2]$ and effect of position of anchoring group on diimine ligand over electronic, electrochemical and light harvesting properties explored.



ARTICLE INFO

Article history:

Received 4 April 2013

Received in revised form 2 June 2013

Accepted 5 June 2013

Available online 19 June 2013

Dedicated to Prof. Kieran C. Molloy

Keywords:

Diimine

Dithiolate

DFT

Light harvesting

TiO₂

ABSTRACT

Four Ni(II) diimine dithiolate complexes viz. $[\text{Ni}(\{\text{S}_2\text{C}_2\text{Ph}_2\}(1,10\text{-Phenanthroline}))]$ (**2**), $[\text{Ni}(\{\text{S}_2\text{C}_2\text{Ph}_2\}(3,3'\text{-dicarboxy-2,2'-bipyridyl}))]$ (**3**), $[\text{Ni}(\{\text{S}_2\text{C}_2\text{Ph}_2\}(4,4'\text{-dicarboxy-2,2'-bipyridyl}))]$ (**4**) $[\text{Ni}(\{\text{S}_2\text{C}_2\text{Ph}_2\}(2,2'\text{-bipyridyl}))]$ (**5**) have been prepared from $[\text{Ni}(\text{S}_2\text{C}_2\text{Ph}_2)_2]$ (**1**) and characterized by microanalyses, UV–Vis, IR, ¹H and ¹³C NMR. Attempts have been made to explain the nature of charge transfer in these molecules through quantum chemical calculations. The light harvesting properties of all the compounds have been studied using these compounds as photosensitizers in TiO₂-based DSSC. The change in position of anchoring group on diimine derivative leads to different structural, electronic and light harvesting properties about the Ni(II) diimine dithiolate dyes.

© 2013 Elsevier B.V. All rights reserved.

Introduction

Last two decades have witnessed a substantial growth in the field of dye-sensitized solar cells (DSSCs) [1–6]. This is due their versatility and cost-effective manufacturing, the organic and

* Corresponding author. Tel.: +91 9451891030; fax: +91 05422367454.
E-mail address: abhinavmarshal@gmail.com (A. Kumar).

inorganic DSSC have been considered as a feasible alternative to conventional solid-state *p-n* photovoltaic devices [7–10]. Out of these dyes the ruthenium polypyridyl dyes have gained interests of chemists owing to their stupendous performance as sensitizers in DSSCs having efficiencies upto 11% [1,3,11,12]. In addition to ruthenium polypyridyl dyes other metal centered dyes including complexes of Fe [13–19], Cu [20–23], Os [24,25] and Re [26] have been used. Additionally the [Pt(II)(diamine)(dithiolate)] [27–30] and [Ni(dithiolene)₂] [31,32] compounds have also been investigated for their light harvesting properties.

Mostly the available solar cell dyes exhibit absorbances at the shorter wavelengths [11,12] and hence longer wavelength dyes are required as they can harness more of the available solar energy and this was established with the help of theoretical calculations [33]. With this viewpoint recently several NIR dye molecules have been reported [31,34,35]. The charge transfer transitions in [Pt((diamine)(dithiolate))] compounds can be assigned as a “mixed-metal ligand to ligands” charge transfer (MMLCT) involving a HOMO that is a mixture of Pt(d) and dithiolate S(p) and a LUMO that involves a π^* bpy orbitals [27–30]. Similar electronic transitional behavior is also anticipated for the [Ni((diamine)(dithiolate))] type complexes [36–41]. Additionally, the substituents on the diimine ligands affects the HOMO and LUMO energy levels and hence the photophysical as well as the electrochemical properties of the molecules. Hence, by tuning the photophysical and electrochemical properties of the dye one can affect the performance of the solar cells.

With these viewpoints and in the quest of the dyes having absorbances in the longer wavelength range we herein wish to report the syntheses, characterization and light harvesting properties of a family of [Ni((diimine)(dithiolate))] complexes.

Experimental

Materials and reagents

All chemical reagents were commercially available and used without further purification. The complex bis(1,2-diphenylethylene-1,2-dithiolene) nickel(II) (**1**) was synthesized according to the previous report [42]. Dichloromethane (DCM) was used as a medium of cyclic voltammogram, purified by standard method.

Elemental analyses were performed on a Perkin–Elmer 240 C, H, N analyzer. Infrared spectra were recorded as KBr pellets on a Varian 3100 FTIR. ¹H and ¹³C NMR spectra were recorded on JEOL AL300 FTNMR spectrophotometers. Chemical shifts were reported in parts per million using TMS as internal standard for ¹H and ¹³C NMR. The absorption spectra in dichloromethane solution were recorded using a Perkin–Elmer LS45 UV–Vis spectrophotometer. Electrochemistry was carried out using a Pt working electrode, Pt rod counter electrode and Ag/AgCl as a working electrode. All electrochemical experiments were carried out in dichloromethane and the supporting electrolyte used was TBAP (0.1 M). After each experiment the reference electrode was calibrated against the ferrocene/ferrocenium couple which was found to be at 0.55 V.

DSSC fabrication

Transparent conductive glass plates coated with an F-doped SnO₂ (FTO, purchased from Pilkington. Co. Ltd., 8 Ω/γ) were used to prepare both the photo- and counter-electrodes. A Ti(IV) bis(ethyl acetoacetato)-diisopropoxide solution (2% w/w in 1-butanol) was spin-coated onto FTO substrates, which were then heated stepwise to 450 °C and maintained at this temperature for 20 min. Commercialized TiO₂ paste (Ti-Nanoxide T, Solaronix) was casted onto the heat-treated FTO substrates by the

doctor-blade technique and then sintered at 450 °C for 30 min. The substrates with thick mesoporous TiO₂ layers (ca. 13–18 μm) were dipped into a dichloromethane solution of **1–5** (0.3 mM) and kept overnight. The unadsorbed dye was washed out with anhydrous ethanol. Pt-layered counter-electrodes were prepared by spin-coating H₂PtCl₆ solution (0.05 M in isopropanol) onto FTO glass and then sintered at 400 °C for 30 min. The dye-adsorbed TiO₂ electrodes and Pt counter-electrodes were assembled into a sealed sandwich-type cell by heating at 80 °C using a hot-melt ionomer film (Surlyn) as a spacer between the electrodes. The electrolyte was composed of 0.6 M 3-hexyl-1,2-dimethylimidazolium iodide, 0.05 M iodine, 0.05 M LiI and 0.5 M 4-tert. butylpyridine in acetonitrile. A drop of electrolyte solution was placed in a hole drilled in the counter-electrode and driven into the cell via vacuum backfilling. Finally the hole was sealed using additional Surlyn and a 0.1 mm thick glass cover.

Solar cell efficiency

The photoelectrochemical performance characteristics (short circuit current J_{sc} (mA cm⁻²), open-circuit voltage V_{oc} (V), fill factor *ff* and overall conversion efficiency η) were measured under illumination with a 1000 W xenon lamp (Oriel 91193) using a Kiethley Model 2400. The light intensity was confirmed to be a homogenous over an 8 × 8 in² area was calibrated with a Si solar cell for 1 sun light intensity (AM 1.5G, 100 mW cm⁻²). Accidental increase in the temperature inside the cell were prevented by using a cooler with a propeller. Each measurement was repeated for three times to confirm reproducibility.

IPCE measurement

Incident photon-to-current conversion efficiency (IPCE) for the dyes **1–5** were measured as a function of wavelength from 400 to 900 nm (PV measurement Inc.) using a standard tungsten-halogen lamp as monochromatic light and a broadband bias light for approximating 1 sun light intensity.

Results and discussion

Synthesis

The Ni(II) diimine dithiolato complexes viz. [Ni((S₂C₂Ph₂)(1,10-Phenanthroline))] (**2**), [Ni((S₂C₂Ph₂)(3,3'-dicarboxy-2,2'-bipyridyl))] (**3**), [Ni((S₂C₂Ph₂)(4,4'-dicarboxy-2,2'-bipyridyl))] (**4**), [Ni((S₂C₂Ph₂)(2,2'-bipyridyl))] (**5**) were prepared by the reaction between the corresponding bpy and their derivatives with [Ni(S₂C₂Ph₂)₂] (**1**) in equimolar ratio in refluxing toluene (see Scheme 1 supplementary informations).

Spectroscopy

The IR spectra for all the five compounds display bands in the region of 1359–1370 cm⁻¹ associated with the perturbed C=C stretch. In addition to this, bands occurring in the region of ~1140 cm⁻¹ can be assigned to the perturbed C–S bond and the band in the region ~882 cm⁻¹ arises due to the stretching of Ph–C(S)=C moiety for all the five complexes. Additionally the bands observed in the range of 1600–1400 cm⁻¹ arises because of the stretching of C=C and C=N bonds of the bipyridyl ligands and their derivatives. In the case of **3** and **4** the bands ~3100 cm⁻¹ can be assigned to –COOH functional.

The purity and composition of all the five compounds have been checked by NMR spectroscopy. All of the compounds display sharp

Table 1
Electrochemical data for the dyes.

| Dye | $E_{1/2}$ (V vs. Ag/AgCl) | | | |
|----------|---------------------------|--------------------|-------------------|-------------------|
| | $E_{\text{Red},2}$ | $E_{\text{Red},1}$ | $E_{\text{Ox},1}$ | $E_{\text{Ox},2}$ |
| 1 | 0.11 ^a | -0.74 ^a | 0.12 ^a | |
| 2 | | | 0.56 ^a | 1.09 ^a |
| 3 | -1.05 ^b | -0.69 ^b | 0.56 ^a | 1.10 ^a |
| 4 | -1.19 ^b | -0.82 ^b | 0.55 ^a | 1.09 ^a |
| 5 | | | 0.57 ^a | 1.11 ^a |

^a Peaks are electrochemically reversible and values represents $E_{1/2}$.

^b Peaks are electrochemically irreversible and values represents peak potential.

¹H NMR signals which integrate well to the corresponding hydrogens.

Electrochemical investigation

The electrochemical properties of all the five compounds were investigated by cyclic voltammetry in dichloromethane solution (Table 1). The complex **1** displayed a reversible peak for the mono-electron reduction at the half-wave potential of 0.12 V. The di-electron reduction was observed at $E_{1/2} = -0.74$ V. The diimine analogs of **1** displayed two fully reversible reduction peaks and one irreversible oxidation peak. Previous investigations have revealed that the diimine ligands influence the reduction potentials of the compounds and the dithiolene/dithiolate ligands influence the oxidation potential of the compounds [43]. This is due to the fact that the LUMO resides on the bipy ligands and HOMO is partly dithiolene/dithiolate based. The multiple oxidation for all the four dyes occurs at almost similar potentials and hence this can be assigned as the oxidation of the HOMO centered over the dithiolene/dithiolate moiety. Since, invariably in all the four diimine derivatives, the dithiolate moiety is identical so it is expected that the oxidation will take place at similar potentials. It is interesting to note that the first reduction potential of **3** occurs at less negative potential in comparison to the rest of the three derivatives. The optimized geometry for **3** (see Fig. S1 supplementary informations) obtained at the DFT level of theory indicates a significant torsion angle (32.16°) between the pyridine rings of the bipyridyl derivative. This lack in planarity may possibly interfere with the delocalization of the charge between the two pyridine rings thereby causing them to behave more like two separate pyridine moieties. So, the electrochemical response in the case of **3** is influenced by both the electronic and steric effects. The electrochemical responses for all the four diimine derivatives indicate that oxidation takes

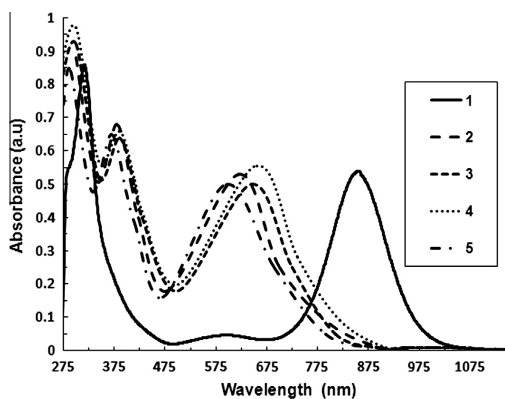


Fig. 1. Electronic absorption spectra for the dyes **1–5** (recorded in 2×10^{-5} M dichloromethane solution for **1** and 2×10^{-3} M solutions for **2–5**).

place on the dithiolate ligand and reduction on the diimine derivatives. This indicates that the charge transfer across the molecules is directional from dithiolate ligand to diimine derivative. In addition to this the location of HOMO also indicates that when the dye is oxidized the positive charge density is placed further from the TiO₂. Also, the LUMO of all of the four derivatives is at an energy suitable to allow charge injection into the TiO₂ conduction band having band edge at -0.81 V vs. Ag/AgCl [44].

Electronic absorption spectroscopy

The electronic spectra for all of the five dyes were recorded in dichloromethane (Fig. 1). In the case of **1**, the bands observed below 400 nm can be assigned to ligand-to-metal charge transfer (LMCT) and intraligand charge transfer transitions [45]. The intense band observed at 857 nm can be assigned to $\pi \rightarrow \pi^*$ transition between HOMO and LUMO [46]. The band observed at 857 nm in the case of **1** is observed to be blue shifted in the case of its diimine derivative and matches well with the previously reported dye **2** [38]. The intense band in the UV regions for the dyes **2–5** can be assigned to the $\pi \rightarrow \pi^*$ intraligand transitions. The bands at ~ 575 – 675 nm region for all the four Ni(II) diimine dithiolate dyes can be assigned to ligand to ligand charge transfer (LLCT) transition. The absorption in the visible region of the electromagnetic spectrum is well within the acceptable range required for a DSSC sensitizer.

The locations of calculated HOMO and LUMO densities for all the five complexes are presented in Fig. S2 (Supplementary informations). In the cases of heteroleptic diimine dithiolate complexes **2–5**, it is apparent from the plots that the HOMO is mainly the dithiolate ligand based having feeble contribution from the phenyl ring as well as the Ni(II) center. The LUMO as speculated is almost entirely diimine ligand based. This observation is consistent with the HOMO/LUMO positions of the previously reported diimine dithio nickel(II) complexes [32]. In the case of **1** the HOMO is located on both of the dithiolate moiety as well as on the phenyl ring and after the electron excitation at the LUMO level the electron density moves from the ligand towards the nickel plane. Calculations indicate that in the case of **2–5** the charge transfer is unidirectional from dithiolate ligands to phenanthroline/bipyridyl or its derivatives while this phenomenon is not observed in the case of **1**. Hence, compounds **2–5** can serve as potential candidates for the light harvesting.

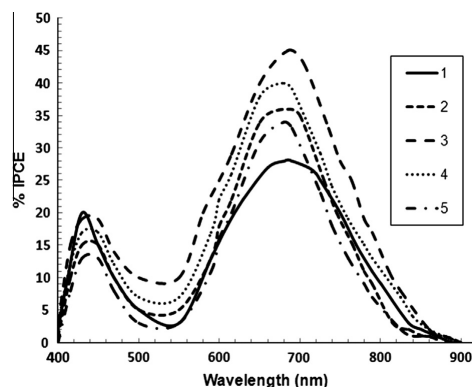


Fig. 2. The IPCE plot vs. excitation wavelengths for DSSCs using **1–5**.

Application of 1–5 to dye-sensitized solar cells

The photovoltaic performance of DSSCs using 1–5 were studied under 1 sun (A_m 1.5G, 100 mW cm^{-2}). Experimental conditions for cell fabrication and measurement of solar cell characteristics were carefully kept as unchanged as possible so that the cell characteristics would reflect the function of the dyes.

The monochromatic IPCE values for devices using 1–5 are presented in Fig. 2. Broad curve covers the region from 400 to 900 nm for all of the devices. No significant variations in the IPCE were observed in these devices prepared from the dyes 2–5. The IPCE spectrum exhibits a maximum of 45% for the dye 3 at 685 nm while this value is lowest in the case of homoleptic system 1 (28%). Hence, it can be said that the symmetrical behavior of the complexes and position of substituents control the DSSC's performance to a considerable extent. In other words, these minor differences might simply arise from different light harvesting efficiencies in the dyes adsorbed on the TiO_2 surface.

The current–voltage characteristics of the devices in the dark reveals sufficient rectification effects with significantly different behavior depending on the device (Fig. 3a). The turn-on voltages associated with hole transfer from the dye-grafted TiO_2 electrode to the electrolyte increases in the order $1 < 5 < 2 < 4 < 3$. Part b of the Fig. 3 shows the photovoltaic performance of the device again indicating remarkable dependences on the dyes. The characteristic parameters taken from the Fig. 3b including the open-circuit voltages (V_{oc}), short-circuit current (J_{sc}), fill-factors (ff) and power conversion efficiencies (η) are presented in Table 2. The ff values are almost constant (49–61%), indicating that the device configurations are similar and the device performance reflects the electronic nature of the dyes.

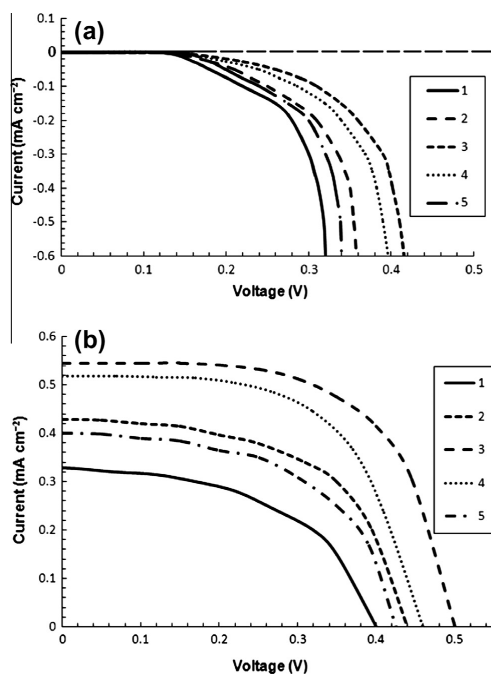


Fig. 3. Current density–voltage curves for DSSCs using 1–5 measured (a) in the dark and (b) under 1 sun simulated sunlight illumination (A_m 1.5G, 100 mW cm^{-2}).

Table 2

Output parameters of cells sensitized by different diimine dithiolate Ni(II) compounds.

| Compound | J_{sc} (mA/cm^2) | V_{oc} (V) | ff | η (%) | IPCE |
|----------|-------------------------------|--------------|------|------------|------|
| 1 | 0.328 | 0.402 | 0.49 | 0.06 | 28 |
| 2 | 0.430 | 0.440 | 0.55 | 0.10 | 36 |
| 3 | 0.545 | 0.500 | 0.61 | 0.17 | 40 |
| 4 | 0.519 | 0.460 | 0.57 | 0.14 | 45 |
| 5 | 0.400 | 0.425 | 0.52 | 0.08 | 34 |

The inferior performance of the dye 1 in comparison to rest of its derivative can be attributed to its symmetrical homoleptic nature. This is also supported by the DFT calculations which indicates the localization of the electron density in the metallic ring plane of the nickel bis(dithiolene) complex which is unfavourable for the electron injection (Fig. S2 supplementary informations). Additionally, there is lack of chemical bond between the dye and the TiO_2 nanoparticulate which can stimulate the excited electrons of the dye to effectively inject into the conduction band of the TiO_2 [47]. As evident from the Fig. 3, diimine derivatives of dye 1 gave relatively better performances. This is due to the heteroleptic nature of all the four Ni(II) diimine dithiolate dyes, which improves the effective electron injection and charge separation. However, still the efficiencies of dyes 2 and 5 are not promising. This is due to the lack of chemical bonds between the dyes and the TiO_2 [47] which can stimulate the excited electrons of the dye to effectively inject into the conduction band of the TiO_2 . In the case of the dyes 3 and 4 having $-\text{COOH}$ functionals at 3,3' and 4,4' positions of the bipyridyl moiety still do not exhibit sufficiently high efficiency. This may be due to the planar geometry of the complex 4, which may have lead to the aggregation of the molecule through $\pi \cdots \pi$ stacking as previously observed in Pt(II) complexes [48]. This dye aggregation can induce significant hindrance which in turn can limit the number of sensitizer bound to the TiO_2 surface and may lead to the intermolecular quenching. In the case of 3, there is deviation from planarity around Ni(II) center which may lead to relatively lesser extent of $\pi \cdots \pi$ stacking. Hence, the amount of intermolecular quenching in 3 will be relatively less than 4 which may lead to the relatively higher efficiency for 3 in comparison to 4.

Conclusion

The investigations revealed that the symmetrical homoleptic complexes are inferior candidates as the dye in DSSC due to the unfavourable electron injection properties. The investigation indicates that the change in position of anchoring group on diimine derivative leads to different structural and electronic properties about the Ni(II) diimine dithiolate dyes. The twisted structure in the case of 3 as observed in the DFT optimized structure influences the electrochemical response which is evident in the reduction potential of this complex. The DFT calculations on the diimine dithiolate complexes indicate that the HOMO is localized on dithiolate ligand and LUMO is mainly localized on the phenanthroline/bipyridyl/bipyridyl dicarboxylate derivative. This indicates that charge transfer in these heteroleptic complexes are uni-directional in nature. This is the first report of the Ni-based dye sensitizer where the bipyridyl is substituted at the 3,3'-positions. Although the efficiencies are not upto the mark but the study indicates that by incorporating appropriate functional groups at appropriate positions on both dithiolate as well as bipyridyl group may lead to the enhancement of the photovoltaic parameters of these Ni(II) diimine dithiolate dyes.

Acknowledgments

This work is supported by the Department of Science and Technology, New Delhi, India, and by the Research Foundation of Lappeenranta University of Technology. The computational resources were provided by CSC-Scientific Computing Ltd., Espoo, Finland.

Appendix A. Supplementary material

Supplementary data associated with this article can be found, in the online version, at <http://dx.doi.org/10.1016/j.saa.2013.06.022>.

References

- [1] B.C. O'Regan, M. Grätzel, *Nature* 353 (1991) 737–740.
- [2] A. Hagfeldt, M. Grätzel, *Chem. Rev.* 95 (1995) 49.
- [3] A. Hagfeldt, M. Grätzel, *Acc. Chem. Res.* 33 (2000) 269.
- [4] S. Ardo, G.J. Meyer, *Chem. Soc. Rev.* 38 (2009) 115.
- [5] A. Hegfeldt, G. Boschloo, L. Sun, L. Kloo, H. Pettersson, *Chem. Rev.* 110 (2010) 6595–6663.
- [6] M.T. Spitler, B.A. Parkinson, *Acc. Chem. Res.* 42 (2009) 2017–2029.
- [7] A. Jäger-Waldau, *Renew. Sustain. Energy Rev.* 11 (2007) 1414.
- [8] M. Grätzel, *Acc. Chem. Res.* 42 (2009) 1788.
- [9] J.W. Bowers, H.M. Upadhyaya, S. Calnan, R. Hashimoto, T. Nakada, A.N. Tiwari, *Progr. Photovolt. Res. Appl.* 17 (2009) 265.
- [10] M.K. Nazeeruddin, M. Grätzel, in: V. Ramamurthy, K.S. Schanze (Eds.), *Semiconductor Photochemistry and Photophysics (Molecular and Supramolecular Photochemistry)*, Marcel Dekker, New York, 2003, pp. 287–331.
- [11] C.A. Bignozzi, R. Argazzi, C.J. Kleverlaan, *Chem. Soc. Rev.* 29 (2000) 87.
- [12] M.K. Nazeeruddin, M. Grätzel, *Comp. Coord. Chem.* 11 (2004) 719.
- [13] S. Ferrere, *Chem. Mater.* 12 (2000) 1083.
- [14] S. Ferrere, *Inorg. Chim. Acta* 329 (2002) 729.
- [15] S. Ferrere, B.A. Gregg, *J. Am. Chem. Soc.* 120 (1998) 843.
- [16] A. Kumar, R. Chauhan, K.C. Molloy, G. Kociok-Köhn, L. Bahadur, N. Singh, *Chem. – Eur. J.* 16 (2010) 4307.
- [17] V. Singh, R. Chauhan, A. Kumar, L. Bahadur, N. Singh, *Dalton Trans.* 39 (2010) 9779.
- [18] S.K. Singh, R. Chauhan, B. Singh, K. Diwan, G. Kociok-Köhn, L. Bahadur, N. Singh, *Dalton Trans.* 41 (2012) 1373.
- [19] R. Chauhan, M. Trivedi, L. Bahadur, A. Kumar, *Chem. Asian J.* 6 (2011) 1525.
- [20] T. Bessho, E.C. Constable, M. Grätzel, A.H. Redondo, C.E. Housecroft, W. Kylberg, M.K. Nazeeruddin, M. Neuberger, S. Schaffner, *Chem. Commun.* (2008) 3717.
- [21] B. Bozic-Weber, E.C. Constable, C.E. Housecroft, M. Neuberger, J.R. Price, *Dalton Trans.* 39 (2010) 3585.
- [22] E.C. Constable, A. Hernandez Redondo, C.E. Housecroft, M. Neuberger, S. Schaffner, *Dalton Trans.* (2009) 6634.
- [23] E.C. Constable, C.E. Housecroft, M. Neuberger, J. Price, A. Wolf, J.A. Zampese, *Inorg. Chem. Commun.* 13 (2010) 74.
- [24] G. Sauve, M.E. Cass, S.J. Doig, I. Lauerma, K. Pomkyl, N.S. Lewis, *J. Phys. Chem. B* 104 (2000) 3488.
- [25] T. Yamaguchi, T. Miyabe, T. Ono, H. Arakawa, *Chem. Commun.* 46 (2010) 5802.
- [26] J.B. Asbury, E. Hao, Y. Wang, T. Lian, *J. Phys. Chem. B* 104 (2000) 11957.
- [27] M. Hissler, J.E. McGarrah, W.B. Connick, D.K. Geiger, S.D. Cummings, R. Eisenberg, *Coord. Chem. Rev.* 208 (2000) 115.
- [28] A. Islam, H. Sugihara, K. Hara, L.P. Singh, R. Katoh, M. Yanagida, Y. Takahashi, S. Murata, H. Arakawa, G. Fujihashi, *Inorg. Chem.* 40 (2001) 5371.
- [29] E.A.M. Geary, N. Hirata, J. Clifford, J.R. Durrant, S. Parsons, A. Dawson, L.J. Yellowlees, N. Robertson, *Dalton Trans.* (2003) 3757.
- [30] E.A.M. Geary, L.J. Yellowlees, L.A. Jack, I.D.H. Oswald, S. Parson, N. Hirata, J.R. Durrant, N. Robertson, *Inorg. Chem.* 44 (2005) 242.
- [31] Q. Miao, J. Gao, Z. Wang, H. Yu, Y. Luo, T. Ma, *Inorg. Chim. Acta* 376 (2011) 619.
- [32] C.L. Linfoot, P. Richardson, K.L. McCall, J.R. Durrant, A. Morandeira, N. Robertson, *Sol. Energy* 85 (2011) 1195.
- [33] H.J. Snaith, *Adv. Funct. Mater.* 20 (2010) 13–19.
- [34] S. Mori, M. Nagata, Y. Nakahata, K. Yasuta, R. Goto, M. Kimura, M. Taya, *J. Am. Chem. Soc.* 132 (2010) 4054.
- [35] Q.Q. Miao, L.Q. Wu, J.N. Cui, M.D. Huang, T.L. Ma, *Adv. Mater.* 23 (2011) 2764.
- [36] T.R. Miller, I.G. Dance, *J. Am. Chem. Soc.* 95 (1973) 6970.
- [37] I.G. Dance, T.R. Miller, *J. Chem. Soc. Chem. Commun.* (1973) 433–434.
- [38] A. Vogler, H. Kunkely, *Angew. Chem. Int. Ed. Engl.* 20 (1981) 386–387.
- [39] C.-T. Chen, S.-Y. Liao, K.-J. Lin, C.-H. Chen, T.Y. Lin, *Inorg. Chem.* 38 (1999) 2734–2741.
- [40] S.D. Cummins, L.-T. Cheng, R. Eisenberg, *Chem. Mater.* 9 (1997) 440–450.
- [41] C.A. Mitsopoulou, *Coord. Chem. Rev.* 254 (2010) 1448–1456.
- [42] G.N. Schrauzer, V. Mayweg, *J. Am. Chem. Soc.* 84 (1962) 3221.
- [43] S.D. Cummins, R. Eisenberg, *J. Am. Chem. Soc.* 118 (1996) 1949.
- [44] M.K. Nazeeruddin, A. Kay, I. Rodicio, R. Humphry-Baker, E. Mueller, P. Liska, N. Vlachopoulos, M. Grätzel, *J. Am. Chem. Soc.* 115 (1993) 6382.
- [45] K. Ray, T. Weyhermüller, F. Neese, K. Wieghardt, *Inorg. Chem.* 44 (2005) 5345.
- [46] H. Shiozaki, H. Nakazumi, Y. Nakado, *Chem. Lett.* (1987) 2393.
- [47] T. Ma, K. Inoue, H. Noma, K. Yao, E. Abe, *J. Photochem. Photobiol. A: Chem.* 152 (2002) 207.
- [48] A. Islam, H. Sugihara, K. Hara, L.P. Singh, R. Katoh, M. Yanagida, Y. Takahashi, S. Murata, H. Arakawa, *Inorg. Chem.* 40 (2001) 5371.

SUPPLEMENTARY INFORMATIONS

FOR

**Synthesis, Characterization and Light Harvesting Properties of Nickel(II)
Diimine Dithiolate Complexes**

Abhinav Kumar,^{a*} Sami Auvinen,^b Manoj Trivedi,^c Ratna Chauhan^d and Matti Alatalo^b

^aDepartment of Chemistry, Faculty of Science, University of Lucknow, Lucknow – 226 007,
India

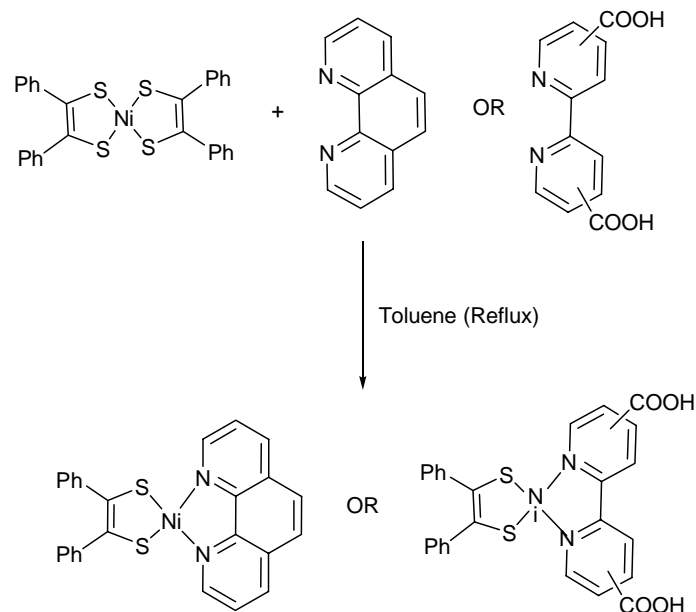
E-mail: abhinavmarshal@gmail.com

Tel: +91-9451891030; Fax: +91-05422367454

^bFaculty of Technology, Department of Mathematics and Physics, Lappeenranta University of
Technology, Lappeenranta, Finland FI-53851

^cDepartment of Chemistry, University of Delhi, Delhi, India

^dCentre for Materials for Electronics Technologies, Pune, India



Scheme 1. Synthesis of the dithiolate complexes.

1.1 Syntheses

1.1.1 Synthesis of bis(1,2-diphenylethane-1,2-dithiolene) nickel(II), **1**.

Benzoin (2.12 g, 10 mmol) was refluxed with P_2S_5 (3.33 g, 15 mmol) in 30 ml of dioxane for 2 h. During this period, the thiophosphoric ester of dithiobenzoin was formed. The hot reaction mixture was filtered to remove the excess P_2S_5 and a solution of $NiCl_2 \cdot 6H_2O$ (1.16 g, 4.9 mmol) in 8 ml distilled water was added to the filtrate. The reaction mixture was heated on steam bath for 2 h. Black crystal of the complex was formed which were collected filtration, washed with a minimal amount of dioxane, water, ethanol, and finally with diethyl ether. Purification was conducted by recrystallization from boiling toluene to afford 1.63 g of green-black crystals, (0.325 g, yield 60%). $C_{28}H_{20}S_4Ni$ (541.98): calcd. C, 61.89, H, 3.71, S, 23.60; found: C, 61.74; H, 3.63; S, 23.23 %. 1H NMR ($CDCl_3$, δ): 7.26, (d, 4H), 7.28 (d, 4H), 7.34-7.35 (m, 8H), 7.38-7.39 (m, 4H). ^{13}C NMR ($CDCl_3$, δ): 128.4, 128.8, 128.9, 141.2 (C_6H_5), 181.5 ($C=C$). IR (KBr, cm^{-1}): 1571, 1493, 1442, 1361, 1138, 882, 749, 696, 409. UV-Vis (CH_2Cl_2 , nm) λ_{max} : 270, 317, 598, 857.

1.1.2 Synthesis of 1,2-diphenylethylene-1,2-dithiolato 1,10-phenanthroline nickel(II), 2.

To a stirring toluene solution (30 mL) of **1** (0.542 g, 1 mmol) was added dropwise a methanol solution (20 mL) of the 1,10-phenanthroline (0.180 g, 1 mmol). The solution was additionally stirred for another 30 min and refluxed for 24 h and filtered to obtain dark blue residue. This was filtered and dried. (0.351 g, yield 73%); C₂₆H₁₈N₂NiS₂ (481.26): calcd. C, 64.89; H, 3.77; N, 5.82; S, 13.33; found: C, 64.78; H, 3.83; S, 13.53 %. ¹H NMR (CDCl₃, δ): 9.34 (d, 2H, phen), 8.44 (d, 2H, phen), 8.41 (m, 2H, phen), 7.90 (m, 6H, phen and Ph), 7.35-7.33 (m, 4H), 7.16-7.14 (m, 2H), . ¹³C NMR (CDCl₃, δ): 128.4, 128.8, 128.9, (C₆H₅), 150.0, 146.1 (phen), 141.2 (C₆H₅), 135.8 (phen) 181.5 (C=C). IR (KBr, cm⁻¹): 1748, 1645, 1600, 1571, 1493, 1442, 1361, 1138, 1079, 882, 749, 696, 412.

1.1.3 Synthesis of 1,2-diphenylethylene-1,2-dithiolato 2,2'-bipyridyl-3,3'-dicarboxylate nickel(II), 3.

To a stirring toluene solution (30 mL) of **1** (0.542 g, 1 mmol) was added dropwise a methanol solution (20 mL) of the 1,10-phenanthroline (0.244 g, 1 mmol). The solution was additionally stirred for another 30 min and refluxed for 24 h and filtered to obtain dark blue residue. This was filtered and dried. (0.344 g, yield 65%); C₂₆H₁₈N₂NiO₄S₂ (545.26): calcd. C, 57.27; H, 3.33; N, 5.14; S, 11.76; found: C, 57.88; H, 3.51 S, 12.10 %. ¹H NMR (CDCl₃, δ): 8.68 (d, 2H, bpy), 8.27 (d, 2H, bpy), 7.54 (m, 2H, bpy) 7.26, (d, 2H, Ph), 7.28 (d, 2H, Ph), 7.35 (m, 4H, Ph), 7.40 (m, 2H, Ph), . ¹³C NMR (CDCl₃, δ): 123.0, 126.8 (bpy), 128.4, 128.8, 128.9 (C₆H₅), 138.0 (bpy), 141.2 (C₆H₅), 150.9, 159.1 (bpy), 167.3 (-COOH), 181.5 (C=C). IR (KBr, cm⁻¹): 3082, 1718, 1590, 1571, 1493, 1442, 1361, 1138, 882, 749, 696, 581, 531, 410.

1.1.4 Synthesis of 1,2-diphenylethylene-1,2-dithiolato 2,2'-bipyridyl-4,4'-dicarboxylate nickel(II), 4.

To a stirring toluene solution (30 mL) of **1** (0.542 g, 1 mmol) was added dropwise a methanol solution (20 mL) of the 1,10-phenanthroline (0.244 g, 1 mmol). The solution was additionally stirred for another 30 min and refluxed for 24 h and filtered to obtain dark blue residue. This was filtered and dried. (0.371 g, yield 68%); C₂₆H₁₈N₂NiO₄S₂ (545.26): calcd. C, 57.27; H, 3.33; N, 5.14; S, 11.76; found: C, 57.73; H, 3.49 S, 12.14 %. ¹H NMR (CDCl₃, δ): 8.99 (d, 2H, bpy), 8.86 (d, 2H, bpy), 7.95 (d, 2H, bpy), 7.23, (d, 2H, Ph), 7.26 (d, 2H, Ph), 7.35 (m, 4H, Ph), 7.40 (m, 2H, Ph). IR (KBr, cm⁻¹): 3112, 1892, 1716, 1603, 1564, 1493, 1442, 1361, 1138, 882, 749, 696, 581, 513, 415.

1.1.5 Synthesis of 1,2-diphenylethylene-1,2-dithiolato 2,2'-bipyridyl nickel(II), 5.

To a stirring toluene solution (30 mL) of **1** (0.542 g, 1 mmol) was added dropwise a methanol solution (20 mL) of the 2,2'-bipyridyl (0.156 g, 1 mmol). The solution was additionally stirred for another 30 min and refluxed for 24 h and filtered to obtain dark blue residue. This was filtered and dried. (0.338 g, yield 74%); $C_{24}H_{18}N_2NiS_2$ (457.24): calcd. C, 64.89; H, 3.77; N, 5.82; S, 13.33; found: C, 64.78; H, 3.83; S, 13.53 %. 1H NMR ($CDCl_3$, δ): 8.59 (d, 2H, bpy), 8.50 (, 2H, bpy), 7.66 (m, 2H, bpy), 7.26, (d, 2H, Ph), 7.28 (d, 2H), 7.35 (m, 4H), 7.40 (m, 2H), 7.12 (m, 2H, bpy). IR (KBr, cm^{-1}): 1568, 1548, 1493, 1442, 1361, 1269, 1138, 1032, 882, 749, 696, 656, 409.

1.2 Computational details

Optimized molecular geometries for all of the five dyes were calculated using the B3LYP exchange-correlation functional [1, 2]. The LANL2DZ basis set for Ni and while 6-31G** basis set for C, H, N, O and S atoms were employed. The optimized structures of the dyes were used for molecular orbital analyses. All the calculations were performed using Gaussian09 software [3].

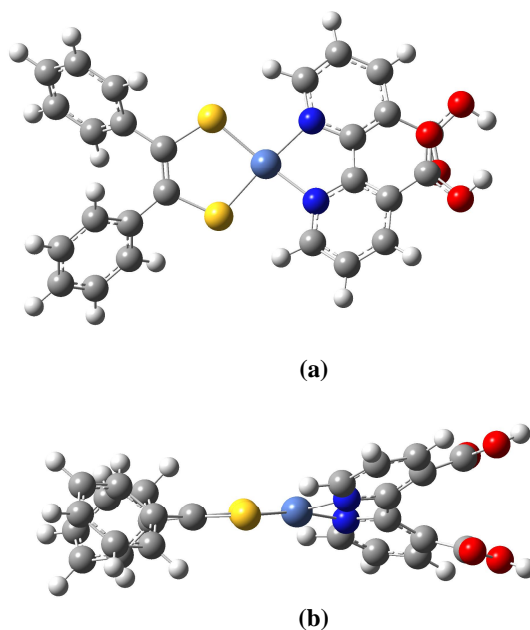


Fig. S1 DFT Optimized structure for **3** (a) Front view (b) Side view.

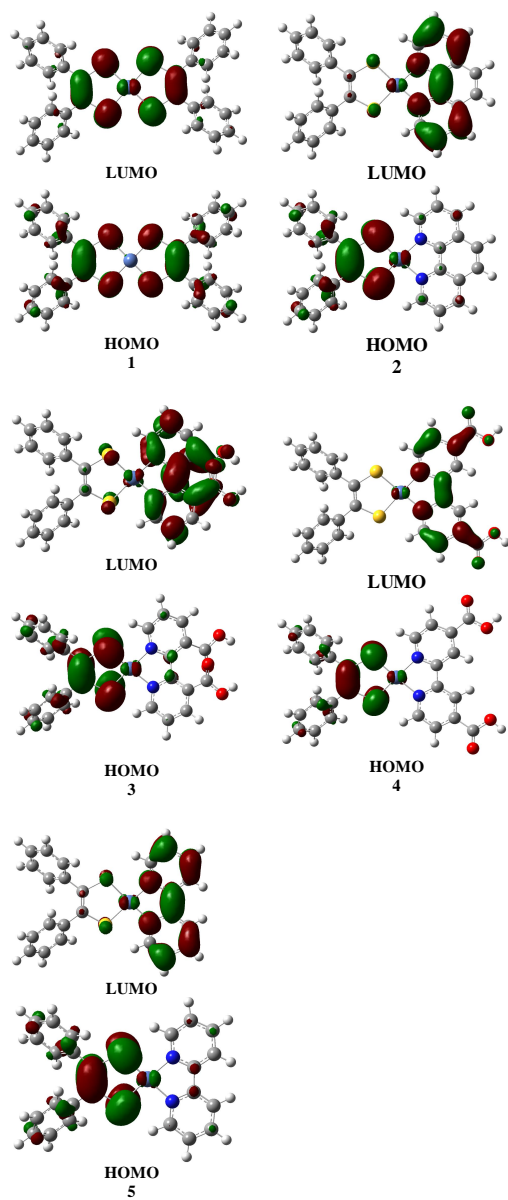


Fig. S2 DFT calculated isosurface plots of HOMO and LUMO for dyes **1-5**.

[1] A. D. Becke, J. Chem. Phys. 98 (1993) 5648-5652.

- [2] C. Lee, Y. Wang, R. G. Parr, *Phys. Rev. B: Condens. Matter Mater. Phys.* 37 (1988) 785-789.
- [3] M. J. Frisch, G. W. Trucks, H. B. Schlegel, G. E. Scuseria, M. A. Robb, J. R. Cheeseman, J. A. Montgomery, T. Vreven Jr., K. N. Kudin, J. C. Burant, J. M. Millam, S. S. Iyengar, J. Tomasi, V. Barone, B. Mennucci, M. Cossi, G. Scalmani, N. Rega, G. A. Petersson, H. Nakatsuji, M. Hada, M. Ehara, K. Toyota, R. Fukuda, J. Hasegawa, M. Ishida, T. Nakajima, Y. Honda, O. Kitao, H. Nakai, M.; Klene, X. Li, J. E. Knox, H. P. Hratchian, J. B. Cross, V. Bakken, C. Adamo, J. Jaramillo, R. Gomperts, R. E. Stratmann, O. Yazyev, A. J. Austin, R. Cammi, C. Pomelli, J. W. Ochterski, P. Y. Ayala, K. Morokuma, G. A. Voth, P. Salvador, J. J. Dannenberg, V. G. Zakrzewski, S. Dapprich, A. D. Daniels, M. C. Strain, O. Farkas, D. K. Malick, A. D. Rabuck, K. Raghavachari, J. B. Foresman, J. V. Ortiz, Q. Cui, A. G. Baboul, S. Clifford, J. Cioslowski, B. B. Stefanov, G. Liu, A. Liashenko, P. Piskorz, I. Komaromi, R. L. Martin, D. J. Fox, T. Keith, M. A. Al-Laham, C. Y. Peng, A. Nanayakkara, M. Challacombe, P. M. W. Gill, B. Johnson, W. Chen, W. M. Wong, C. Gonzalez and J. A. Pople, GAUSSIAN 03 (Revision D.01), Gaussian, Inc., Wallingford, CT, 2004.

Publication IV

S. Auvinen, M. Lahti, M. Alatalo "Unoccupied Titanium 3d States in Stoichiometric TiO₂ Nanoparticles"

Submitted: Journal of Physics: Condensed Matter (2013).

ACTA UNIVERSITATIS LAPPEENRANTAENSIS

523. HÄMÄLÄINEN, HENRY. Identification of some additional loss components in high-power low-voltage permanent magnet generators. 2013. Diss.
524. SÄRKKÄ, HEIKKI. Electro-oxidation treatment of pulp and paper mill circulating waters and wastewaters. 2013. Diss.
525. HEIKKINEN, JANI. Virtual technology and haptic interface solutions for design and control of mobile working machines. 2013. Diss.
526. SOININEN, JUHA. Entrepreneurial orientation in small and medium-sized enterprises during economic crisis. 2013. Diss.
527. JÄPPINEN, EERO. The effects of location, feedstock availability, and supply-chain logistics on the greenhouse gas emissions of forest-biomass energy utilization in Finland. 2013. Diss.
528. SÖDERHOLM, KRISTIINA. Licensing model development for small modular reactors (SMRs) – focusing on the Finnish regulatory framework. 2013. Diss.
529. LAISI, MILLA. Deregulation's impact on the railway freight transport sector's future in the Baltic Sea region. 2013. Diss.
530. VORONIN, SERGEY. Price spike forecasting in a competitive day-ahead energy market. 2013. Diss.
531. PONOMAREV, PAVEL. Tooth-coil permanent magnet synchronous machine design for special applications. 2013. Diss.
532. HIETANEN, TOMI. Magnesium hydroxide-based peroxide bleaching of high-brightness mechanical pulps. 2013. Diss.
533. TYKKÄLÄ, TOMMI M. Real-time image-based RGB-D camera motion tracking and environment mapping. 2013. Diss.
534. PEKKOLA, SANNA. Performance measurement and management in a collaborative network. 2013. Diss.
535. PANOREL, IRIS CHERRY. Pulsed corona discharge as an advanced oxidation process for the degradation of organic compounds in water. 2013. Diss.
536. TORKKELI, LASSE. The influence of network competence of internationalization of SMEs. 2013. Diss.
537. MOLANDER, SOLE. Productivity and services – safety telephone services for the elderly. 2013. Diss.
538. SITARZ, ROBERT. Identification of research trends in the field of separation processes. Application of epidemiological model, citation analysis, text mining, and technical analysis of the financial markets. 2013. Diss.
539. KATTEDEN, KAMIEV. Design and testing of an armature-reaction-compensated permanent magnet synchronous generator for island operation. 2013. Diss.
540. HÄMÄLÄINEN, HARRI. Integration of learning supportive applications to development of e-portfolio construction process. 2013. Diss.
541. RATCHANANUSORN, WARIN. Development of a process for the direct synthesis of hydrogen peroxide in a novel microstructured reactor. 2013. Diss.

542. PERFILEV, DANIIL. Methodology for wind turbine blade geometry optimization. 2013. Diss.
543. STROKINA, NATALIYA. Machine vision methods for process measurements in pulping. 2013. Diss.
544. MARTTONEN, SALLA. Modelling flexible asset management in industrial maintenance companies and networks. 2013. Diss.
545. HAKKARAINEN, JANNE. On state and parameter estimation in chaotic systems. 2013. Diss.
546. HYYPIÄ, MIRVA. Roles of leadership in complex environments
Enhancing knowledge flows in organisational constellations through practice-based innovation processes. 2013. Diss.
547. HAAKANA, JUHA. Impact of reliability of supply on long-term development approaches to electricity distribution networks. 2013. Diss.
548. TUOMINEN, TERHI. Accumulation of financial and social capital as means to achieve a sustained competitive advantage of consumer co-operatives. 2013. Diss.
549. VOLCHEK, DARIA. Internationalization of small and medium-sized enterprises and impact of institutions on international entrepreneurship in emerging economies: the case of Russia. 2013. Diss.
550. PEKKARINEN, OLLI. Industrial solution business – transition from product to solution offering. 2013. Diss.
551. KINNUNEN, JYRI. Risk-return trade-off and autocorrelation. 2013. Diss.
552. YLÄTALO, JAAKKO. Model based analysis of the post-combustion calcium looping process for carbon dioxide capture. 2013. Diss.
553. LEHTOVAARA, MATTI. Commercialization of modern renewable energy. 2013. Diss.
554. VIROLAINEN, SAMI. Hydrometallurgical recovery of valuable metals from secondary raw materials. 2013. Diss.
555. HEINONEN, JARI. Chromatographic recovery of chemicals from acidic biomass hydrolysates. 2013. Diss.
556. HELLSTÉN, SANNA. Recovery of biomass-derived valuable compounds using chromatographic and membrane separations. 2013. Diss.
557. PINOMAA, ANTTI. Power-line-communication-based data transmission concept for an LVDC electricity distribution network – analysis and implementation. 2013. Diss.
558. TAMMINEN, JUSSI. Variable speed drive in fan system monitoring. 2013. Diss.
559. GRÖNMAN, KAISA. Importance of considering food waste in the development of sustainable food packaging systems. 2013. Diss.
560. HOLOPAINEN, SANNA. Ion mobility spectrometry in liquid analysis. 2013. Diss.
561. NISULA, ANNA-MAIJA. Building organizational creativity – a multitheory and multilevel approach for understanding and stimulating organizational creativity. 2013. Diss.
562. HAMAGUCHI, MARCELO. Additional revenue opportunities in pulp mills and their impacts on the kraft process. 2013. Diss.
563. MARTIKKA, OSSI. Impact of mineral fillers on the properties of extruded wood-polypropylene composites. 2013. Diss.

